INFORMATION TO USERS

The most advanced technology has been used to photograph and reproduce this manuscript from the microfilm master. UMI films the text directly from the original or copy submitted. Thus, some thesis and dissertation copies are in typewriter face, while others may be from any type of computer printer.

The quality of this reproduction is dependent upon the quality of the copy submitted. Broken or indistinct print, colored or poor quality illustrations and photographs, print bleedthrough, substandard margins, and improper alignment can adversely affect reproduction.

In the unlikely event that the author did not send UMI a complete manuscript and there are missing pages, these will be noted. Also, if unauthorized copyright material had to be removed, a note will indicate the deletion.

Oversize materials (e.g., maps, drawings, charts) are reproduced by sectioning the original, beginning at the upper left-hand corner and continuing from left to right in equal sections with small overlaps. Each original is also photographed in one exposure and is included in reduced form at the back of the book. These are also available as one exposure on a standard 35mm slide or as a 17" x 23" black and white photographic print for an additional charge.

Photographs included in the original manuscript have been reproduced xerographically in this copy. Higher quality 6" x 9" black and white photographic prints are available for any photographs or illustrations appearing in this copy for an additional charge. Contact UMI directly to order.

U·M·I

University Microfilms International
A Bell & Howell Information Company
300 North Zeeb Road, Ann Arbor, MI 48106-1346 USA
313/761-4700 800/521-0600

Order Number 8906964

Energetic electron precipitation in the aurora as determined by X-ray imaging

Werden, Scott Huntley, Ph.D.

University of Washington, 1988

U·M·I
300 N. Zeeb Rd.
Ann Arbor, MI 48106

Energetic Electron Precipitation in the Aurora as Determined by X-ray Imaging

by

Scott H. Werden

A dissertation submitted in partial fulfillment
of the requirements for the degree of

Doctor of Philosophy

University of Washington

1988

Approved by George K. Parks
(Chairperson of Supervisory Committee)

Program Authorized
to Offer Degree Geophysics

Date 8/5/88

Doctoral Dissertation

In presenting this dissertation in partial fulfillment of the requirements for the Doctoral degree at the University of Washington, I agree that the Library shall make its copies freely available for inspection. I further agree that extensive copying of this dissertation is allowable only for scholarly purposes, consistent with "fair use" as prescribed in the U.S. Copyright Law. Requests for copying or reproduction of this dissertation may be referred to University Microfilms, 300 North Zeeb Road, Ann Arbor, Michigan 48106, to whom the author has granted "the right to reproduce and sell (a) copies of the manuscript in microform and/or (b) printed copies of the manuscript made from microform."

Signature

Date 8/5/88

University of Washington

Abstract

Energetic Electron Precipitation in the Aurora as Determined by X-ray Imaging.

by Scott H. Werden

Chairperson of Supervisory Committee: Professor George K. Parks

The presence of energetic precipitating particles, as determined by auroral bremsstrahlung X-rays, is indicative of various important processes in the magnetosphere, including acceleration, transport, and wave particle interactions. This work examines two aspects of energetic particle dynamics in Earth's magnetosphere through the use of an X-ray imager flown from a stratospheric balloon in the auroral zone. The design and theory of this instrument is completely described, including the technique of image formation using an on-board microprocessor and a statistical analysis of the imaging process. Day side energetic electron precipitation is examined in the context of global energy dissipation during the substorm process. It is found that the relationship between events on the night side and the day side are considerably more complex than can be modeled with just a simple picture of drifting particles that induce instabilities, wave growth, and pitch angle diffusion into the loss cone. The driving force for precipitation is probably not the presence of the energetic

electrons (>30 keV) alone, but is influenced either by local effects or the less energetic component. The presence of small scale structure, including gradients and complex motions in the precipitation region in the morning sector, suggests a local process influencing the rate of electron precipitation. The spatial and temporal evolution of a classic 5-15 second pulsating aurora during the post breakup phase is also examined with the X-ray imager. The pulsations are superimposed on a longer time scale modulation that exhibits small scale beam-like features during the most intense portion of the X-ray emission. The pulsation source region does not appear to be highly localized, but is stronger in the portion of the emission region that is also characterized by a softer energy spectrum and enhanced X-ray fluxes. The scale lengths are similar to the well known characteristics for the optical aurora, implying that the spatial structure for both the low and high energy electrons are rooted deep in the magnetosphere rather than in the auroral region.

TABLE OF CONTENTS

Page

LIST OF FIGURES

LIST OF TABLES

Acknowledgements

I would like to thank Professor George Parks for the support and opportunity to learn experimental work in space physics. The construction of the instrument involved in this dissertation could not have been accomplished without the help of the engineering staff, Chris Wagner, George Pitt, and especially John Chin. I thank Professor Ken Clark for the many enjoyable seminars at his house as well as the reading of this and other manuscripts. Professor Bob Holzworth offered many hours of practical advice throughout these last few years, and of course my fellow grad-students were always sources of constructive comments, criticisms, and levity. Lisa Peterson certainly deserves thanks for arranging many TRs, PRs, and an uncountable number of overnight "panic-grams" to George at NASA. My special companion who is so patient in times of frustration, able to turn a tired-computer-frustrated mood into laughter, full of good advice, and grows the best jalapeno peppers in Seattle, deserves more credit than a few words here can achieve. This person, of course, is Rita. I also wish to mention my fellow dinner table pundits, Ralph, Pi, and Glen Garioch.

This work was supported by National Science Foundation grants ATM-8420220 and ATM-8710314.

Chapter 1

Introduction

1. Magnetospheric Energy Dissipation

Earth's magnetosphere serves as a sink for some of the energy contained in the plasma flow coming from the Sun. Since the solar wind is a gas of charged particles, it is influenced by electromagnetic forces and interacts strongly with the terrestrial magnetic field through the Lorentz force. This results in the formation of a boundary between the solar wind and the magnetosphere. The coupling of solar wind momentum and energy into the magnetosphere is quite complex, but for this work it is sufficient to know that there is a transfer of energy into the magnetosphere and this must somehow be dissipated. The geomagnetic substorm is the relaxation of the magnetosphere to a more stable state, and it is a particular manifestation of the substorm, the precipitation of energetic particles, that will be addressed in this thesis.

The excess energy which accumulates in Earth's inner magnetosphere is primarily contained in the particles, not in the fields. The energy to be dissipated is largely carried by the particles into the auroral zone and the ionosphere and is expended through a variety of mechanisms; electromagnetic radiation, Ohmic heating, and collisions. Understanding the characteristics of these particles reveals important information on the mechanisms of energy dissipation and relaxation of the magnetosphere. The terrestrial magnetic field lines which thread the outer magnetosphere map to the auroral region allowing access of magnetospheric plasma to lower altitudes. Since the density increases and the temperature decreases at lower altitudes, the lower ionosphere is collisional while the greater part of the magnetosphere is not, and therefore the auroral ionosphere is a region that dissipates most magnetospheric energy.

The precipitating particle energy is expended by collisions with atmospheric constituents and these collisions can be ionizing or radiative (bremsstrahlung). The former can produce visible photons and the latter produces X-rays. If we arbitrarily put the high-low energy cutoff at about 20 keV, and restrict attention to X-rays above this energy, the high energy electrons can undergo either type of interaction, the low energy particles only result in ionization losses. Therefore, bremsstrahlung X-ray measurements are sensing only the by-products of the energetic component of precipitating electrons.

The high energies of bremsstrahlung X-rays constrains the underlying physics. For example, observations indicate the presence of an acceleration region in the high auroral region. This has been postulated to be produced by several different mechanisms, from an electrostatic potential to a stochastic process [*Kan and Lee*, 1981; *Bryant*, 1987]. Whatever the mechanism is, it is observed to have an upper range of several keV and therefore the particles responsible for bremsstrahlung X-rays must originate much deeper in the magnetosphere rather than local to the auroral region.

The energy spectrum of bremsstrahlung X-rays is often exponential with e-folding values in the range 15-20 keV in the midnight region, becoming progressively harder in the early and late morning sectors [*Barcus et al.*, 1966; *Akasofu*, 1968]. However, there is sometimes a finer temporal structure to the spectrum which is related to phases of the event being observed. For instance, near midnight at the very onset stage of a substorm, the spectrum is sometimes seen to harden and then soften during the main phase [*Sauvaud et al.*, 1987]. Often the spectrum is not a simple exponential, but contains two distinct components, each with its own exponential behavior [*Barcus and Rosenberg*, 1966]. This observation suggests the presence of two different plasma populations or possibly a single plasma component that is being energized by two different mechanisms.

Temporal behavior is observed to have variations on many different time scales. Pulsating aurora is commonly seen in the early morning hours during the post-breakup phase of the substorm and has periods of 5-15 seconds. The original observations were of optical pulsations but similar behavior is seen in the X-rays [*Parks et al.*, 1968; *Barcus et al.*, 1966]. Experiments have shown a high degree of correlation between optical and X-ray measurements [*Hofmann and Greene*, 1972] and a careful analysis of timing has shown that the modulation mechanism must be at very high altitudes rather than local to the auroral region [*Bryant et al.*, 1971; *Oguti et al.*, 1982]. The underlying mechanism responsible for the pulsations has been postulated to be a kinetic instability, [*Coroniti and Kennel*, 1971] in which the repetitive character is due to modulation by a low frequency MHD wave, or a saturation and relaxation process with two different time scales [*Davidson*, 1986].

There are temporal variations which occur on time scales of several minutes and do not necessarily show periodic trends. These time scales are often comparable to

Alfven and convection times and may be due to a motion of the flux tubes that connect the collisional region to the middle magnetosphere. The direction and sense of these motions put constraints on the magnetospheric source of the particles. For instance, eastward propagation of a flux tube in the early morning hours would be expected in a zeroth order magnetosphere model. However, equatorward or poleward motions in this sector would indicate the presence of local forces acting on the particles.

Visual auroral features show spatial scales from less than a kilometer to near global in size. Similar spatial morphology of X-ray emitting regions should be evident for certain classes of events, and good agreement has been observed some of the time [*Stadsnes et al.*, 1987]. A correlation analysis of the time variations in X-ray fluxes at two different balloons by *Barcus et al.*, [1966], revealed length scales of 100 to 200 km. These scale lengths are based on the results of two narrow-collimated detectors widely separated and do not reveal any fine structure which may be present. *Mauk and Parks* [1981] used X-ray imaging to look for finer spatial structure and found that bremsstrahlung X-ray production is sometimes localized to scale lengths of 15 km or less.

In the spirit of elucidating global magnetospheric dynamics, it is necessary to seek correlations between the local observations and events occurring elsewhere in the magnetosphere. One important correlation is the relationship between the events occurring near local midnight and events which occur in the morning sector. The characteristics of particle precipitation in this sector may be a consequence of a purely spatial effect, such as the so-called drift precipitation model [*Kangas et al.*, 1975], from purely temporal effects such as magnetospheric compression or some types of wave-particle interactions, or they may be caused by combinations of spatial and temporal effects. The latter may include processes which are thought to be purely temporal in nature, but often occur only at certain local times indicating some degree of spatial effect on the mechanism. These would include REP (Relativistic Electron Precipitation) [*West and Parks*, 1984] and micro-bursts, both in the late morning sector, and pulsating aurora in the early morning region.

This special role the morning sector has in the global dissipation of energy in the substorm process is not well understood. For instance, it is widely thought that the particles which take part in the dynamics of this region come from the nightside injection region. However, the presence of relativistic electron precipitation predominately in the noon sector indicates some additional acceleration process local to the dayside, or a precipitation mechanism that is more selective to the very high energy component. The exact relationship between the above described dayside processes to the presumed nightside source region is not well known, nor are the mechanisms which give rise to the various observed precipitation modulations. This problem is both global and local in nature, and requires a detailed examination of the particles and fields which may be playing a role in morning sector electron precipitation.

The goal of this present work is to report on two auroral events that provide new information on the temporal-spatial relationships involved in electron precipitation. The first report will be an extensive analysis of morning sector precipitation dynamics using a variety of ground and spacecraft data. The X-ray measurements are interpreted in the context of an interaction region that may be driven by the drifting electrons from the nightside. Evidence of local acceleration and complex motions of the precipitation region suggest that this event is strongly influenced by local processes. The second result will be a presentation of simultaneous measurements of energy, spatial, and temporal features of a pulsating auroral event. The data coverage for this event was not as good as the first, so this report will be much briefer.

This work will also introduce an improved technique of X-ray imaging as a research tool in magnetospheric physics. The presentation of the development of the X-ray camera is more of an engineering endeavor than a scientific one, but it is a complex technique and deserves an appropriate discussion to understand the measurements being made. This will also involve an understanding of the problem of data deconvolution which will be introduced in the next section.

This study uses the results of an experiment which was carried out in July of 1986 in Kiruna, Sweden, which is located at about 67° of latitude, so is well situated for auroral studies. The experiment was a collaborative effort among the University of Washington and the Universities of Oslo and Bergen in Norway, the Royal Institute of Technology in Sweden, the University of Toulouse in France, and the Space Research Institute of Graz, Austria. Each group contributed a different experiment to be launched on stratospheric balloons. The University of Washington's instrument was the X-ray imager

1.1. Data Deconvolution

The nature of this remote sensing experiment requires a scheme which will relate X-ray measurements to the characteristics of the original electrons. The relationship between the behavior of the detected X-rays and the energy-spectral characteristics and spatial morphology of the source X-rays is quite complicated due to Compton collisions and photoelectric absorption in the atmosphere. This problem has been examined by several workers for various parameters and geometries.

Pilkington and Anger [1971] showed that the measured spectrum of an X-ray detector depends upon both the geometry of the detector collimation and upon the source distribution of the X-rays. Their study did not use actual measurements, but used a Monte-Carlo simulation of X-ray transport through the atmosphere. The source spectrum of X-rays, not parent electrons, was related to the X-rays which would be measured at balloon altitudes. An isotropic angular distribution of X-rays at the source was assumed. *Berger et al.* [1970] and *Berger and Seltzer* [1972] did a similar study, but concentrated on the effects different angular distributions of X-rays at the source region would have on an X-ray spectrum at balloon altitudes.

The sensitivity to the angular distributions of the electrons undergoing bremsstrahlung is also important, and this type of study has also been performed. *Gaines et al.* [1986] performed detailed studies using data from a low altitude satellite for the source distribution of electrons and data from balloons which were conjugate to the spacecraft for the X-ray measurements. Since the region below the satellite is collisional, a Fokker-Planck treatment was used to obtain the evolution of the parent electron distribution down to a thin region in which bremsstrahlung collisions were deemed to take place, about 100 km in altitude. The bremsstrahlung process and the subsequent transport through the atmosphere, were simulated with a Monte-Carlo calculation. The calculated X-ray spectra were then compared to the measured spectra and found to generally be in good agreement.

These studies have not thoroughly investigated the spatial evolution of a distribution of X-rays as they propagate through the atmosphere, nor have they investigated the response of an imaging detector to X-rays. Such a study is useful in helping to correctly interpret data obtained with the X-ray imaging technique. These problems are addressed in Chapter 2 with a Monte Carlo simulation of X-ray transport in the atmosphere.

1.2. Auroral Experimentation using X-ray Imaging

The dynamics of the aurora can be studied from several different perspectives, each one distinguished by its characteristic length and time scales. Polar orbiting satellites and rocket experiments have the advantage of making *in situ* measurements of the local plasma parameters, however the constraints of orbital motion prevent many of these experiments from making measurements over long time scales. This is particularly true for rockets and low altitude spacecraft. Furthermore, there is always an inherent ambiguity in separating spatial effects from temporal effects when taking measurements from a single point, especially when that point itself is in motion. Satellite imaging of the auroral oval and the polar cap is a powerful tool, but does not always fully resolve the small scale dynamics occurring within an aurora.

Balloon borne instruments are able to examine the longer time scale behavior of auroral phenomena since the balloon's motion is usually much slower than many typical auroral time scales. Furthermore, the space-time ambiguity can be partly resolved by the use of imaging techniques and/or use of two-point or greater measurements. These imaging techniques allow an examination of structures of scale lengths of order tens of kilometers in times as short as a few seconds.

As mentioned earlier, the high energy electrons can undergo either ionizing or radiative interactions, the lower energy electrons result primarily in ionization losses. The problems which can be addressed with an X-ray imager carried by a stratospheric balloon include those processes that occur deep in the magnetosphere and result in changes in a particular portion of velocity space, the loss cone.

Magnetospheric research has achieved tremendous understanding of the temporal behavior of many processes but significant questions still remain in the areas of coupling between different regions of the magnetosphere and spatial extent. This is largely due to the necessity of many measurements from different spatial regions to obtain a global picture of cause-and-effect and spatial relationships. An alternative to making many *in situ* measurements at various points in space is to exploit the auroral "window" into the magnetosphere. That is, observe the signatures produced in the ionosphere of physical processes that are occurring much deeper in the magnetosphere. This is possible through the mapping of terrestrial magnetic field lines from the ionosphere to other magnetospheric regions, and the ability for these field lines to easily couple these regions together.

1.3. Scope of Study

The structure of this study is as follows. The construction of the instrument was a major part of this work and the operating principles and all necessary details in the design will be presented in Chapter 2. The theory of X-ray interactions in matter is not the primary topic of this work, but it is necessary to draw upon some of the results for Chapter 2. This topic is covered in detail in Appendix A. Chapter 2 will also discuss the techniques involved in data analysis, a discussion of the imaging problem, and the effects of the atmosphere on the ability to obtain source characteristics. The scientific studies will be presented in Chapters 3 and 4 as self contained presentations, that is, an introduction to the work, data analysis, and a discussion of the results. The analysis of dayside particle precipitation will be done in Chapter 3, while Chapter 4 will present the results of the pulsating-aurora study. Chapter 5 will be a final commentary on the scientific results and suggestions for future studies. A summary of the experiment will also be done to analyze problems, possible solutions, and future improvements.

Chapter 2

Design of Instrument and Methods of Data Analysis

This chapter will present the design of the X-ray imaging instrument, the image formation algorithms, and other techniques used in data analysis. Some of the design considerations, and much of the performance, depend upon the theory of X-ray interaction in matter. This topic is discussed in detail in Appendix A. Although there was a considerable amount of engineering detail that went into the construction of the imager, these details will not be dwelt upon any further than is necessary to understand how the instrument works and why certain performance options were chosen.

The instrument is conceptionally divided into a "front end", and electronics. The front end includes the pseudo-optics, scintillator, photomultiplier tubes, mechanical housing, high voltage and preamps. Pseudo-optics is a term used to denote the pin-hole collimation arrangement to focus the X-rays. The electronics section includes all other analog circuits, analog-to-digital converters, coincidence and anti-coincidence logic, and a computer. The general characteristics of scintillators and photomultiplier tubes (PMTs) are presented in Appendix B. An understanding of both these topics is helpful in the theory of the X-ray imager.

2.1. Instrumental Design

The basic design of the instrument can be divided into several logical units: (1) The "optical" end which includes the scintillator-photomultiplier tube combination and the associated X-ray collimation, (2) analog electronics, (3) digital electronics, (4) computer, and (5) power supplies (high voltage and low voltage). The block diagram for this is shown in Figure 2.1. An important auxiliary to the instrument is the ground station equipment (GSE), which will be outlined at the end of this section.

The design of the detector was constrained by some practical considerations. The weight must be minimal, the complexity of the system must not be too great, and it must be designed and fabricated in a reasonable amount of time. The need for simplicity was dictated mostly by telemetry limits but also by the fact that more complex systems have more ways to fail. The design rational was thus to improve upon a previously flown design. The extension of a previous design saved prototyping time, ensuring the realization within deadlines, and although the improvements increased the complexity, the basic idea was still simple.

2.1.1. Anger X-ray Cameras

Pin hole X-ray imagers are a particular type of Anger camera [*Anger*, 1958], and function similar to the optical analog. X-rays are "focused" by lead collimation onto the NaI scintillator, which acts as the film. See Figure 2.2. Photons carry information from the object and deposit energy to the film, leaving an image of the object. The energy deposition to the film is not permanent but radiates away as optical photons (plus local heating in the scintillator). For low energy X-rays, such as 30 keV, the number of scintillation photons is about 500. Thus a critical component of this scheme is the efficient detection of the scintillation photons and this makes the use of a PMT a natural choice. Photomultiplier tubes do not have the capability to determine the direction from which the impinging photons have come from, so the method used to find the X-ray impact position is analogous to triangulation: Use two point-measurements of the same event to deduce the relative position between the two sensing points. Using a third point-measurement in the same way will provide the position within a plane. Thus, the Anger camera requires multiple PMTs coupled to a single, thin scintillating crystal to image a planar source distribution of X-rays. The image is then formed by analyzing the relative amounts of light sensed by each of the PMTs. The total energy deposited in the scintillator results from the sum of all the PMTs, and this is directly related to the incident X-ray energy.

The system roughly obeys Poisson statistics (see Appendix B for a detailed discussion on this), so a minimum statistical uncertainty and the best resolution are achieved when the maximum number of photons are sensed by each PMT. The ideal design is to have no more than the minimum number of PMTs necessary to perform a triangulation calculation, i.e., three, since this will maximize the number of scintillation photons that each receives. This is not the actual situation since the properties of the scintillator have been ignored. The diffusion of the scintillation photons within the scintillator-light pipe combination (see Appendix B) is dictated by refractions at interfaces, critical reflections, and diffuse scattering at the walls. The result is that the light intensity at the outer face of the quartz window is not a simple $1/r^2$ decrease, but becomes much sharper when the distance from the X-ray impact region is such that critical reflections at the quartz-NaI interface become dominant. This is illustrated in Figure 2.3. X-ray impacts that are centered over one PMT and far from one or more of the others will result in many photons entering one PMT, giving good statistics for that one, and few photons and poor statistics for the others. Since the positions are determined from relative amounts of light sensed by three PMTs for each X-ray, i.e., by ratios of PMT outputs, the poor statistics in any one PMT will dominate in the overall position resolving ability. There is thus an optimum geometry for the instrument which is a balance between the proper PMT size and lightpipe thickness.

The proper geometry is determined by several factors. The energy range of X-rays to be detected determines the correct thickness of scintillator. The anticipated X-ray fluxes will influence the size chosen for the "pin-hole", and the relative size of the pin-hole to the size of the imaging plane sets a limit on the resolving ability of the detector. Finally, the desired temporal resolution will also influence the pin-hole size. Statistically meaningful images require many X-rays which can be gathered either by having a large aperture, with accompanying low spatial resolution, or accumulating over long time periods, with low temporal resolution.

The previous imager of *Mauk, et al.*,[1981] had four tubes, each of which was round, coupled to the scintillator. Analysis of the performance of that instrument showed that the gaps between the tubes resulted in problems with position and energy determination for X-rays which were incident on the crystal over void areas, partly due to lost scintillation photons degrading the counting statistics. The natural improvement was to use PMTs which could be close packed, thus minimizing any loss of photons. This could be done with a couple different available shapes, square or hexagonal. Since better resolution can be achieved with more tubes, the latter were chosen, giving the configuration shown in Figure 2.4.

2.1.2. Optical Design Optimization

The quartz window is necessary to isolate the NaI crystal from the environment, but is also used to obtain the optimum amount of light diffusion to all the PMTs. The imaging technique requires the scintillation photons to be transmitted over a reasonable area of the surface which is coupled to the photomultiplier tubes so that the light is apportioned amongst several tubes. Since the positioning scheme uses ratios of PMTs to determine where the X-ray hit, the best spatial resolution is obtained when this ratio has large changes for small changes in the impact position of the X-ray.

There is a fine balance between too much spreading and too little. Both extremes will result in poor resolution, although at different locations relative to particular PMTs. An X-ray impact directly over a PMT which illuminates a small area will give little light to the neighboring PMTs. When the light levels are low the statistics are poor and the uncertainty is high. However, for the case of an impact over the boundary between two tubes, the optimum illuminated area should be small since the best information will come from these two PMTs alone.

The above parameters for our instrument were determined as follows: The assigned data rate would limit us to about 300 X-ray events per second, and auroral X-ray fluxes during times of activity can range from 100 - 1000 (roughly) X-rays (cm^2 sec ster$)^{-1}$, so the pin-hole was initially at 1 cm radius, giving a geometric factor of 5.4 cm^2 ster.

2.1.3. Anticoincidence

Since cosmic rays are charged particles, they can invoke the same response in the scintillator as X-rays. (See Appendix B). To improve the quality of the data it is helpful to eliminate the effects of cosmic rays as much as possible. This was accomplished by encasing the entire collimation chamber within another scintillating material, organic compound NE-102, with two PMTs coupled to it, and thereby sensing the passage of a cosmic ray through this material as well as the NaI scintillator. The event will still register in the normal PMTs, but will be eliminated electronically without further processing. This component of the instrument is the anti-coincidence. The above described geometry of the system is shown in Figures 2.5.

2.1.4. Electronics

Each photomultiplier tube has its own analog circuit and a portion of the digital circuit. Other than the amplifying process, the main tasks of the analog circuits were to manipulate the signal so that it could be correctly digitized, and to provide some information to the logic evaluation board. Once digitized, the values were taken up by the computer. The digital representation was to eight bits or one byte, covering 256 possible PMT output levels. The analog and digital circuit elements are schematically shown in the block diagram of Figure 2.6. This first section will describe the analog portion of the electronics.

The output from the PMTs is a burst of charge, on the order of a picoamp (10^{-12} amp) which is converted to a voltage pulse at the first stage of amplification.

This stage has some noteworthy properties. The first is that the preamp inputs are particularly vulnerable to external noise sources. It is therefore advantageous to have the preamp as close to the PMT as possible and also well shielded. This was done by mounting the preamps inside the camera housing within 10 cm of the PMTs.

The input pulse to the preamps is a current which is integrated to obtain the total charge. A charge sensitive amplifier integrates the charge build up on a capacitor, converting it to a voltage at the output. A shunt resistor is needed to discharge the capacitor and this network will have a characteristic time constant, RC, which determines the tail shape of the pulse. The rise time is determined by the time constant of the scintillator-PMT combination. The ability of the rest of the analog circuit to respond linearly and without side effects depends upon this pulse shape. The pulse shape and preamp saturation were later found to be problematic in the operation of the instrument.

The remainder of the analog circuit consisted of passive pulse shaping circuits, variable gain amplifiers to balance the gain variations of the PMTs, peak-hold detectors, and A/D converters. As discussed above, the output of the preamp is a voltage pulse, the maximum value of which is proportional to the charge out of the PMT. The peak-hold detector follows this pulse until this maximum is found, and then holds this value on its output so it can be digitized. It also provides a signal to the logic evaluation section to notify it that it was holding a PMT output pulse which needed to be either digitized or rejected.

The final link in the analog circuit chain for each channel were the A/D converters which were controlled by the logic board and had an interface to the computer.

The logic board was critical in that it would signal to the ADC when to start its conversion. The computer was critical to its operation in providing the reset back to a state where it could do another conversion, as well as reading in the data.

2.1.4.1. Logic Circuits

It is desirable to reduce the amount of spurious or unusable data which is processed. One source is the cosmic ray influence discussed above, which is largely detected with the anti-coincidence system. However, since the pin-hole aperture cannot be shielded, and cosmic rays have ready access to the system through it, "high level" detection logic was implemented to reject any event which had an analog value in *any* channel above a predetermined value. This also eliminated the higher energy X-rays, so the instrument had a definite upper limit for X-rays detected.

The remainder of the logic served a dual purpose of "minimum criteria" validation, coincidence, and anticoincidence logic. The coincidence attempts to eliminate all spurious pulses which have their origins in the PMT or associated electronics rather than in the scintillator. Since the latter events are assumed to be caused by thermal emissions and are therefore random, the different channels should be completely uncorrelated. The electronic implementation for this is closely associated to the necessity of having a minimum number of PMTs sensing an event, which is required by the positioning algorithm. The minimum criteria conditions are discussed in Section 2.2.1.

The instrument has a nominal lower energy cutoff of 20 keV, the minimum energy that is not severly degraded by atmospheric absorption and scattering. This is achieved by only considering those events which have an analog value above a predetermined value, corresponding to a 20 keV X-ray. A single channel which has satisfied these requirements can then trigger the entire logic evaluation circuitry. Note that any channel can do this; the triggering is simply a logical "or" of all seven channels.

All seven channels were then considered simultaneously for minimum coincidence conditions. If the result of the tests for either anticoincidence or high-level was true, or if the minimum criteria was not met, then the operation was aborted and the peak-hold detectors were reset. If all conditions were satisfied the A/D converters were signaled to start converting and the computer was notified that there would be data available to be read in. In this case, when the computer had finished reading in the data it signaled the logic circuit it was done, and this in turn reset both the peak-hold detectors and the A/D converters. The logic equations were implemented in an EPROM (Erasable, Programmable, Read-Only Memory), which is a socketed IC. Thus it could be taken out and the logic equations fiddled with, without changing actual circuits. Figure 2.7 diagrams this entire logic evaluation process.

2.1.4.2. Computer

Since each X-ray event is described by the output of seven PMTs, each of which was one byte, the overall data rate could be very large. The allotted telemetry rate was 512 bytes/sec., giving a maximum of about 170 X-ray events per second. The time resolution of the instrument is dependent upon having enough X-rays analyzed to form a statistically sound image, so an on-board computer was used to do some preliminary calculations, reduce the data volume per X-ray, and therefore increase the number of X-rays processed.

The computer served other purposes; controlling the flow of data, monitoring the performance of the instrument, inserting some statistical and diagnostic information into the data stream, and interfacing to the telemetry system. The computer was built at University of Washington and consisted of several components which will be logically divided into the asynchronous process controller, the serial and parallel data interfaces, and the microprocessor with its associated volatile and permanent memory.

The occurrence of X-rays is of course a random process so the computer had to be able to respond in an asynchronous fashion, that is, stop whatever task it was currently doing and process an X-ray. There were critical sections of code which could not be interrupted but these were kept minimal. There were other events that could happen asynchronously and these had to also be watched for and scheduled for the computer. The interrupt controller handled all these tasks from the hardware end. There were four regular external asynchronous processes: a need for parallel input from the occurrence of a validated X-ray, two associated with the telemetry system communication through the serial interface (input and output), and a clock pulse to allow count rate computation.

The data interfaces brought data into the computer from the A/D converters or from the serial interface, and sent data out through the serial interface. The latter communicated to the telemetry system or, during testing and calibration, it could communicate with any standard serial-data computer interface, such as a P.C. The telemetry protocol was for data to be delivered once a second, in a continuous burst, immediately after it was requested. This delivery was at 19200 baud, or about 1900 bytes/second. The data transmission window was quite narrow, so it had to be sent efficiently.

The hardware configuration of the microprocessor is not particularly noteworthy; much of its usefulness is better illustrated by the programming of it. These programs resided in the non-volatile EPROM memory, which was 4096 bytes in size. Considerable storage was possible in the 16 kbytes of temporary memory, although this was not all used. Most of the storage was used for buffering of data while it was waiting to be output to the telemetry system.

2.1.5. Flight Programs

Those parts of the flight programs which do not involve actual discussion of the data calculations will be considered here. The rest will be looked at in detail when the subject of image formation algorithms is examined in Section 2.2.1. The hardware tasks of the system were outlined above, and each one has a corresponding software routine that took all necessary steps in handling it. The most interesting of these will be discussed without appealing to the actual code. This code was all written in assembly language to maintain speed.

There was only a single synchronous task in the computer, that of the data processing. As long as the data queue was not empty it would be working on this task, otherwise the microprocessor was waiting for data. All of the remaining tasks were "background" or asynchronous processes. Upon the reception of an interrupt by the computer, it determined which of the external processes was requesting attention and acted accordingly. Each of these is discussed below.

X-ray Processing

During times of high X-ray fluxes, more events are generated than can be effectively processed, even with the data reduction in the computer. Thus, after the event was tallied into the current frame's count rate, the computer would determine if the data quota was satisfied for the frame. If it was, the event would not be processed. In either case, the A/D converters still had to be polled for their data, since this was a hardware requirement for their correct operation. The energy discrimination of the external logic only provides an approximate discrimination since the energy is actually a sum of all PMTs. Therefore, if the event was to be processed, a sum was made and the result examined to see if it was within preset values determined from calibration. If this was OK the data would be stored for processing, and a flag set to notify the data processing task.

Clock

The instrument worked on one second time frames and the clock provided the notification for the switching of frames. Performance and statistical information for the closing frame would be completed and stored for transmission. An additional task was to make sure that there had actually been a net data throughput in the previous second. Although the computer and its programs were tested extensively, programming bugs can sometimes be deeply hidden and not appear until too late. If no data was found to have been processed for the entire frame, the entire system was reset to the start-up sequence. A similar feature monitored the data input and would reset the logic circuits. The latter feature turned out to be a saving feature, but the former never was enacted.

Telemetry Interface

The telemetry system, which was also a computer system built by the project engineer, would send synchronization signals to the experimenters as well as a request for data. This task simply pulled bytes out of the previous frame's data buffer and sent them out at the fastest possible rate. The serial interface IC would interrupt the computer every time its output buffer was empty, and the task would provide the data to the interface.

2.1.6. Ground Station Equipment

As outlined above, the X-ray camera electronics is complex in its operation, and needed to be completely debugged. Also, a method was needed which could allow calibration procedures to be performed in a way which was as close to the actual operating mode, so that the tests were true indicators of performance, but not reliant upon the entire data encoding electronics of the control computer, since this would be too cumbersome for testing.

These requirements were satisfied with a data interface for all the balloon payload experiments that was a common RS-232 serial interface operating at 19200 baud. This allowed all experimenters to use PC (e.g., IBM) computers to emulate the data interface protocol that had been defined by the project engineer. The instrument could be operated independently from the control computer, being controlled only by a bench top PC, for all testing and calibration. The same instrument could then be connected directly to the payload data interface, without change, and be operated.

The design of the ground control computer (GCC) which did all data demodulation and blocking, was symmetrical in operation to the flight control computer; all GSEs which formerly were used to gather data from an individual's experiment, now could be connected to the GCC and receive data. The GSE used by the imager could exercise the instrument in several different ways, gather statistical data on performance, and produce various data "products". Typical uses for the GSE was for performance monitoring during cold-hot cycling of the instrument, calibration, and real-time monitoring of data during the flight.

2.1.7. Instrument Performance

The performance of the instrument was judged in several different ways. The energy resolution was measured for two different sources, Am^{241} and Co^{109} providing 66 keV and 22 keV respectively, and comparing these to the resolving capabilities of previously built detectors. This measurement is actually the sum of all the PMTs and it is necessary to know if they are working individually as well as in concert. One way to to do this is to test each PMT before mounting in the camera, or to only look at the output of a single channel after being mounted. Both of these procedures were done. The first was used mostly to choose PMTs which were closely matched in gain, and the second was used to balance them.

The response of the instrument must be uniform across the face of the scintillator. The measured pulse height spectrum should depend very little upon the position over which the source is placed. This spatial dependent energy response is shown in

Figure 2.8. The results are very good, showing less than 10% variation over 90% of the face.

Dead time of the instrument had a few different contributions. The first was the time interval between the initial input of a PMT pulse to the peak-hold circuit till the final reset of all circuits by the computer. This was measured and found to be from 120 to 400 μs. depending upon what was being done with the data. The maximum number of events using the longer time period is determined by the maximum number which can be processed, 333, giving about 13% deadtime. Any number of events above this will use the shorter time interval.

The second deadtime contribution was the amount of time spent by the logic board on spurious or other invalid events. This decision process took about 10 μs. The rate for these was not measured during flight but was looked at in the lab and was found to be about 200 sec^{-1}. The final contribution was the cosmic ray component. Since these can deposit very large amounts of energy to the system and hence saturate the amplifiers, a long delay was allowed to let the system return to a normal state. This delay was set at 50μs. for all but the first instrument. Anti-coincidence count rates averaged 1100 counts/sec., giving a fractional dead time of about 5%. Thus the instrument had a deadtime that was about 18% during times of count rates above 333, with about a 1.2% increase for every additional 100 counts/sec.

2.1.8. Problem Analysis

The imaging technique relies on the six-fold symmetry of the PMT configuration, and on the outer PMTs all having the same response or gain. This was tested in two different ways. The first was to place a source over the center of each of the outer PMTs and measure the response of that channel alone, and then compare these results for all six outer tubes to make sure they were indeed responding the same. The second method was to hold a source directly over the center of the scintillator and make sure each PMT was giving the same output. In principle these should both yield the same output from all PMTs when they are all balanced, but in practice this did not happen. Balancing the outputs using the first method would give unequal results from the second method and vice-versa.

The tests are sensitive to different influences. The second method was dependent upon a spreading of the light which is largely a multiple reflection process. For the geometry of the NaI and quartz window, many of the photons impacting the exit face of the quartz window over an outer PMT have trajectories that are quite oblique. If there are air pockets trapped between the PMT and the quartz surface, the internal reflections will decrease the number of photons going into a PMT. So this method is determining the homogeneity of the optical coupling more than the actual response of the PMTs. The coupling is as important as balancing the gains and required fiddling with the seating of the PMTs. Uniform response was never achieved to complete satisfaction, although the differences were small. The hexagonal shape and close packing of the tubes made it difficult to push them around in the jell and exclude all air pockets. The result of this will be a degradation in the resolution of the image, and although it is hard to quantify this further, it is felt that this is a small effect.

The worst problem of the experiment did not manifest itself until the instruments were launched. This was the occurrence of data drop outs - short (typically one-second) gaps during which little data would be gathered by the instrument. An examination of the status information returned by the computer showed that the problem had its origins in the digital logic. A later analysis of the problem using a spare instrument showed that extremely large input pulses to the preamp would result in saturation, non-linear behavior and some oscillations extending for about 100 μs. This type of input can result from cosmic rays with energies on the order several tens to hundreds of MeV. The lab pre-testing of the preamp included testing with large pulses to simulate cosmic ray impacts, but the test regime was not extended to simulate extremely high energies. The logic should have been immune to all such pathological behavior, foreseen or not, so there was a problem here also. The origin of this problem is quite complex and involves some subtleties in the synchronization in communication between the logic circuits and the analog boards.

For the second balloon flight, from which the data for this work originated, this problem was more of an annoyance than a hindrance. The time intervals when error occurred were detectable by status information returned in the telemetry and thus could be trapped. The result is that the time profile of the data was affected the most. The ability to form images or energy spectra was only slightly affected.

2.2. Methods of Data Analysis

It is helpful to understand the two different phases of the data analysis process. The first is data acquisition and X-ray position determination, both of which occurred on board the balloon in real time. Image formation, on the other hand, uses the data returned to the ground from the experiment and took place here at the University of Washington. A section will be devoted to each of these topics.

Image statistics is an important aspect of the technique and will be discussed with the purpose of defining the meaningfulness of images. A large section will be devoted to the analysis of X-ray transport in the atmosphere, and an algorithm for correcting the data against the atmospheric attenuation and scattering.

2.2.1. X-ray Position Determination and Image Formation

The basic idea behind the production of images was stated previously as exploiting the different amounts of light collected by each PMT for different positions of incident X-rays. For the case of our instrument, this translates into a mapping of points between the seven dimensional space of PMT outcomes to the two dimensional Cartesian or position space on the crystal face. As the problem is stated, this would be a formidable task, as the outcome space alone consists of more than 10^{16} points. The situation is further complicated by the statistical behavior of the system.

The solution to the imaging problem used in this work is more of a pragmatic, empirical approach than one rooted in mathematical rigor. The primary motivation is an algorithm that is not too complicated to implement, since it will be programmed into the on-board computer, but still obtains good results. Considerable research has been done in the formation of X-ray images, but usually with quite different optical configurations (e.g., coded aperture arrays), or operating emphasis (e.g., time-stationary and/or highly localized sources).

The magnitude of the problem can be reduced considerably by appealing to symmetry and other considerations. The arrangement of the seven PMTs has six-fold symmetry, so the position space can be reduced by 1/6. The maximum resolution is determined by, among other things, the "pinhole" aperture size, and when this is mapped down to the crystal face, the maximum number of pixels becomes fixed. The geometry of the crystal and the PMTs suggests a polar coordinate system for the positions, even though this forces the pixels to have nonuniform aspect ratios.

The statistical nature of the outputs allows a further reduction in the dimensionality of the PMT outcome space. Since the relative fluctuations are proportional to $\frac{1}{\sqrt{N}}$ where N = number of photons (see the discussion on PMT statistics in Appendix B), and the diffusion of scintillation light is a function of distance away from the source, the PMTs which are far from the region of the X-ray impact will have a higher uncertainty in their contribution to the position determination. Therefore only those PMTs that are in the immediate neighborhood of the assumed position of the photon are considered, which are usually the ones with the highest outputs. A transformation is made on this reduced space of outcomes, which is formed by taking ratios of the center to the sum of the outer PMTs, and by taking two ratios of two different outer PMTs, two adjacent and two which are separated by one PMT. Only one of these last two will actually be used.

This defines the minimum criteria for the logic equations described in Section 2.1.5; the center tube must have sensed the event, along with three outer tubes which must be adjacent to one another. For very low energy X-rays, statistical fluctuations will mean that sometimes this won't be met, and will lead to some of these being rejected.

The outcome space is now three dimensional, the two coordinates described above and the sum of all PMTs, which is proportional to the energy. A correspondence can be made between the two outcome space coordinates and the two dimensional position space. The correspondence is not linear and the outcome coordinates are not independent, although these are not difficult problems.

The statistical nature of the problem needs to be addressed in more detail. The outcome of each PMT, for a fixed source location of the X-ray, is correctly described by its complete distribution function, which will be called $P_{Q;i}\,(Q;\,i)$ where Q is the electronic, measured outcome of the ith PMT, and $1 \leq i \leq 7$. Given the symmetry considerations, the parameter i takes on only two values which label unique distributions, one corresponding to the outcome of the center PMT, the other corresponding to any of the outer PMTs. For this last statement to hold, the outer PMTs must all have identical behavior. This is partly achieved through PMT selection and partly through adjustment of the gains at the pre-amps. For an ideal, non-statistical system, this distribution would be a delta function.

The distribution changes for different source locations, $\mathbf{X}_k$, and we identify this conditional distribution as; $P_{Q;i,\mathbf{X}_k}\,(Q;\,i,\ \mathbf{X}_k)$. The subscript, k on $\mathbf{X}$ reminds us that the possible source locations are discrete rather than continuous, and hence are not determined to any greater precision than the size of a pixel. The problem of position determination is cast into a probability through the conditional position distribution, $P_{\mathbf{X};\,\mathbf{Q}}\,(\mathbf{X};\ \mathbf{Q})$, which is the distribution of source positions associated with a given outcome-vector, $\mathbf{Q}$. The latter may be direct PMT outcomes or the values derived from the outcomes through a transformation, such as the one above. The formation of an image, or more correctly, the source probability distribution, is obtained from the measurements by a weighted integration (summation) over all outcomes,

$$P_{\mathbf{X}}(\mathbf{X}) = \int d\mathbf{Q}\, P_{\mathbf{X};\mathbf{Q}}(\mathbf{X};\ \mathbf{Q})\, P_{\mathbf{Q}}(\mathbf{Q}) \tag{2.1}$$

where $P_{\mathbf{Q}}(\mathbf{Q})$ is the distribution of *measured* outcomes during the time interval in which the image is to be formed, and the weighting function, $P_{\mathbf{X};\mathbf{Q}}(\mathbf{X};\ \mathbf{Q})$, can be interpretated as the "response" of the system. The essential problem now is to formulate this response function.

The starting point in the determination of $P_{\mathbf{X};\mathbf{Q}}(\mathbf{X};\ \mathbf{Q})$, is through the identification of $P_{Q;i,\mathbf{X}_k}(Q;\ i,\ \mathbf{X}_k)$ as a directly measurable quantity. The latter is the distribution of outcomes, given that the source is at $\mathbf{X}_k$. This may be obtained, for instance, by holding a source of X-rays over a fixed position, $\mathbf{X}_k$, and recording the outcome distributions for the derived quantities. An example of this calibration function for a source held over 10 points along a radius line is shown in Figure 2.9. The inversion of this to obtain $P_{\mathbf{X};\mathbf{Q}}(\mathbf{X};\ \mathbf{Q})$, is done with the use of Baye's theorem [*Papoulis*, 1984],

$$P_{\mathbf{X};\mathbf{Q}}(\mathbf{X};\ \mathbf{Q}) = \frac{P_{\mathbf{Q};\mathbf{X}}(\mathbf{Q};\ \mathbf{X})\, P_{\mathbf{X}}(\mathbf{X})}{\int d\mathbf{Q}\, P_{\mathbf{Q};\mathbf{X}}(\mathbf{Q};\ \mathbf{X})\, P_{\mathbf{X}}(\mathbf{X})} \tag{2.2}$$

The application of Eqn. (2.2) requires knowledge of the function, $P_{\mathbf{X}}(\mathbf{X})$. Since no *a priori* knowledge is available about $P_{\mathbf{X}}(\mathbf{X})$, it will be considered to be the distribution which was used in generating $P_{Q;i,\mathbf{X}_k}(Q;\ i,\ \mathbf{X}_k)$ during calibration.

Since this operation was done uniformly, $P_X(X)$ must be a constant. The choice of a polar coordinate system leads to the following for this function:

$$P_X(X) = P_\Phi(\Phi)\, P_r(r),$$

$$P_\Phi(\Phi) = \frac{1}{2\pi},$$

$$P_r(r) = \frac{3r}{r_0^3}.$$

An alternative method of obtaining the calibration distributions was examined. This idea is very simple and assumes that for a uniform source of X-rays, the correct choice of $P_{X;Q}(X;\ Q)$, must result in a uniform distribution produced by the algorithm. This method of generating tables was the one which was ultimately used since the the calibration X-ray sources made available at the launch site were far too intense and awkward in producing a point-source as required for the original calibration scheme.

2.2.2. Implementation of Imaging Algorithms

The major function of the on-board computer was data volume reduction through position determination using a modification of the above algorithm. The actual code was written in assembly language for computational efficiency. The method outlined above requires further modification to use in a real-time microprocessor computer since it doesn't have the computational power. The mechanically induced rotation of the payload would require the data to be transformed into a non-rotating reference frame before the above integrals can be performed, which is fairly computer intensive, but also the apportioning of several hundred X-rays into 216 pixels and 15 energy bins would result in a poor approximation to the distribution, $P_Q(\mathbf{Q})$.

The implementation algorithm then started with the assumption that the outcome, $\mathbf{Q}$, of each X-ray represented a random sampling of the distribution. So the function, $P_Q(\mathbf{Q})$, in Eqn. (2.1) was substituted with a "test outcome", i.e., a delta function, and the resulting position distribution, $P_X(\mathbf{X})$, was found. The best guess for what the position would be for the test PMT outcome was needed and for this the mean of the above position distribution was used. The median, or even the mode may be a better choice [*Mosteller and Tukey*, 1977]. By testing all possible PMT outcomes (appropriately reduced through symmetry considerations), a list of correspondences between PMT outcomes and best-guesses for the position is found. This allows the positions to be found by a simple translation table that would return a coordinate for a specific PMT ratio. The distribution of possible positions for each set of PMT voltages also has a variance associated with it and this additional information is used on the ground to distribute the mass in one pixel to others.

The coordinates are not separable in Eqn. (2.1), and this presents a problem in a limited memory computer as used in the imager. It was found that the radial determination is relatively insensitive to the azimuthal position of the X-ray impact when it is found from the ratio of the center PMT to the sum of the outer PMTs. However, the azimuth was more sensitive to the radial position, so the correct tables to use were dictated by the radial position. The azimuthal position was found iteratively; the first guess was always to use the outer PMTs with the highest and second highest values, since the X-ray impact would presumably be closest to these. This would be modified for positions which were near the outer edges of the outer PMTs by using information from one more outer tube.

Raw tube outputs values were also sent intermittently for the purpose of verification of the in-flight computations. The period at which this was done was a function of count rate; when the count rate was high, every 100 frames out of 500 frames were raw data, while during low count rates the split was even. Part of the motivation for the latter was that during low count rate times, the data allotment for the X-ray telemetry stream was considerably higher than the amount of reduced data which was generated.

2.2.3. Image Production

Image processing denotes those procedures which occurred after the flight and operate on the received telemetry data. This is a fairly lengthy procedure which will be aided with the flow chart of Figure 2.10. The initial step is to verify the integrity of each data frame. Each frame represents one second of data and is 1024 bytes in length, containing data from all the experiments and also including ambient pressure, temperature, a clock, and a compass. The above quantities were used to ensure that each frame was indeed 1024 bytes long and therefore had no extraneous or missing bytes. If so, the entire frame would be discarded as being unreliable. The validity of each individual experiment's data also needed to be verified. The imager was allotted 512 bytes of telemetry (later boosted to 768 bytes when one experiment was not flown), and this "subframe" had its own indicators to verify the data.

The X-ray frame was examined to make sure the on-board computer was functioning as expected. The clock would indicate if the computer had glitched and reset itself, and status indicators monitored various functions. The most important test was the check on the data itself. Although this could not validate the instrument's operations on the data, it could verify what was being received was not random data. The verification scheme lies in the way in which the reduced data was encoded. Each X-ray's position and energy was encoded into 12 bits, eight for the position and four for the energy. Since there were only 216 pixels, and the first pixel was numbered 1, any pixel number which was zero, or greater than 216, was determined to be invalid. The energy encoding was similar but with only one invalid bit pattern, 0000. The only frames which had invalid X-ray data were those which also had incorrect constants (i.e., clock etc.) and were probably compromised in the telemetry process rather than during computation. The check on the in-flight computations was done by comparison to the results from the analysis of the raw data portion of the data stream.

The first step in the actual image production was to decode the pixel numbers into a position and than transform this position into a particular reference frame. The last step was necessary since the payload was spinning at a rate of about 2 revolutions per minute, about comparable to an image integration time. The housekeeping data included the two horizontal components of an aspect magnetometer which served as a compass and thus provided the exact orientation of the payload.

A primitive image was built up by accumulating events, each of which would be binned into the corresponding pixel. The amount of "mass" accumulated in each bin was scaled by the count rate for the one second time period during which the X-ray positions were determined. This normalization is necessary since the instrument was often data rate limited and would actually be random sampling the actual process. The image is primitive in the sense that it only represents what is detected at the face of the instrument and not what the actual source looks like. The effects of the atmosphere need to be removed as well as angular dependence. This step will be detailed in Section 2.2.5, below. For purposes of plotting and other data manipulations, the completed image is transformed onto a Cartesian coordinate system.

Other physical quantities were also computed or measured, most notably the raw count rates and energy spectra. The former was computed on board the instrument as described in Chapter 2, while the latter could be determined from the four bit energy encoding for each X-ray processed, or from the raw data returned. The count rates require a dead-time correction, and the spectra need to be corrected for the atmosphere.

2.2.4. Image Statistics and Resolution

An important consideration in the formation of images is the degree of confidence which can be associated with them. There are three contributions to the resolving ability: (1) The number of X-rays accumulated in some time interval, (2) the positioning algorithm including the calibration data which it uses, and (3) the size of the "pinhole". The pinhole was fixed before launch to be 3/4 inch diameter (1.9 cm) giving a lower limit to the resolution at 15 km for the X-ray emission plane, or about 2 pixels. The influence of (1) is associated with counting statistics and will determine the minimum time resolution of the instrument. This will be treated as a statistical system described by a signal to noise ratio. The estimation of error in point (2) will be treated in two different ways: the inherent uncertainty associated with the calibration procedure, and the variances in the overall image formation process. The characteristics of the instrument in terms of these parameters are defined in Table (2.1).

Table 2.1 Imager Statistics

X-ray Imager Statistics	
Spatial Resolution:	15 km (16°)
Energy Resolution:	ΔE/E at 66 keV = 0.16
Time Resolution:	Variable
Image Coherency:	Variable, S/N > 4

The usage of the terms signal (S) and noise (N) need to be made more definitive. Consider a set of data, $\{y_i\}$, where i serves as an independent parameter to label each measurement and could, for example, denote a discrete time series, $\{y_{t_1}, y_{t_2}, y_{t_3} \ldots\}$. The data are assumed to have two contributions, a steady part and a random component; $y_i = v_i + e_i$, where e_i is the random part. Averaging this expression gives $\overline{y} = \overline{v}$, since random fluctuations will have zero mean, and the square of this will be the "power" of the signal. The power in the noise will be the mean-square of the fluctuation part, $\overline{e^2} \equiv \sigma_y^2$, giving $\frac{\overline{y}}{\sigma_y}$ for S/N, [*Papoulis*, 1982]. Stationarity with respect to the parameter i is implicit in this definition, so a modification is necessary to account for dependence upon i. This parameter *dependent* mean, $\overline{y_i}$ is defined in Eqn. (2.3), and is related to the common technique of taking a moving or "boxcar" average. The constant, n delineates between the coherent and incoherent scales of the parameter i and requires knowledge of the behavior of y_i. This is assumed to be fairly constant over the range $k-n \leq i \leq k+n$, for all k.

$$\overline{y_k} = \frac{1}{2n-1} \sum_{i=k-n}^{k+n} y_i \qquad (2.3)$$

To be explicit in the application to the imaging problem, the measurements y_i are identified as the observed pixel outcomes. The parameter i is now a label for a particular spatial point and would be better served with the replacement, $\mathbf{x}$, denoting the vectorial position. Note that the origin of this spatial dependence lies not in the instrument, but in the behavior of the X-ray source region itself. For instance, if the source was uniform and isotropic, than there would be no spatial dependence to the mean. The requirement of weak dependence is that the length scale over which changes take place will be greater than several pixels, which is satisfied in light of the size of the aperture. Therefore, Eqn. (2.3) is the average obtained from the few pixels surrounding the point at which the mean is being calculated.

The same analysis as above leads to a similar, non-stationary calculation for the standard deviation. Using these values and the above definition of the signal-to-noise ratio allows the construction of a position-dependent measure of the relative fluctuations. By taking the average of S/N over the entire imaging area, a single number is obtained that can be interpreted as the statistical significance of the entire image, in the sense of a spatially uncorrelated emitting region.

A requirement can now be stated for an image to be statistically reasonable, as having the average signal to noise ratio over all pixels greater than four. This is rather an arbitrary requirement and was arrived at by noting that too much fluctuation makes it difficult to deduce the presence of spatial structure, but too stringent a requirement will restrict integration times and hence, the time scales of temporal behavior that can be examined. This requirement will give a maximum 25% relative fluctuation.

The above test serves as a useful way to look at the degree of fluctuations in a single pixel relative to the average local behavior, but may have slighted the possible coherent behavior between adjacent pixels. However, this should not be a problem since it was accounted for in the concept of a spatially dependent average; the source of this dependence is indeed a coherent behavior. The integration times have been found by trial-and-error to be as short as 15 seconds.

The statistical nature of the imager indicates the need for an estimate of the error produced by the algorithm as well as a position estimate. Recall that the position comes from the relative amounts of light into each PMT, which means taking ratios of the desired PMT outputs. These outputs are not constant for a fixed source location but fluctuate around some mean. Therefore the ratios will correctly be described with a distribution of possible values. The variance of the position distribution associated with a particular source point, $P_{\mathbf{X};\mathbf{Q}}(\mathbf{X};\ \mathbf{Q})$ will be taken as a measure of the uncertainty in position. This is a function of position on the crystal, and has upper and lower bounds of 4 pixels and 2 pixels, respectively, corresponding to 15 to 30 km.

The final statistical measure for an image will be the determination of the variances associated with the image forming process itself. The technique for this is the so-called "jackknife" method [*Mosteller and Tukey*, 1977], which estimates the variance associated with data that has gone through many complex processing steps. To describe this technique, let N be the number of data, and y is the result derived from these data. We wish to find the variability by examining the new result y'_k found by removing the kth datum and performing the same analysis on the N-1 data. This is repeated for all N data points and the estimate of its variance is

$$y' = \frac{1}{N}(y'_1 + \dots\dots y'_N) \qquad (2.4)$$

$$s^2 = \frac{\sum y'^2_k - \frac{1}{k}\left[\sum y'_k\right]^2}{N-1}$$

This technique will be used to examine the variability within each pixel. This differs from the S/N ratio of above by only considering the effect within a single pixel, rather than the accumulation of many.

It is useful to compare these results with those of *Mauk et al.*, [1981]. Their formula for the standard deviation within a pixel was;

$$\sigma = .45\left(\frac{M}{SC} + BG\right) \qquad (2.5)$$

where M is a measure of the number of photons in a pixel, SC is a scaling factor, and BG is the background contribution. The factor 0.45 contains information on the effect of correlations between pixels. This does not say anything further about the uncertainty of the images. The expression used in the current work has the advantage over the one above of being calculated self-consistently from the data alone, with no other parameters necessary.

2.2.5. X-ray Transport in the Atmosphere

The goals of this section are to estimate the effect of Compton scattering and photoelectric absorption on the X-ray measurements. This will be done by simulating the propagation of an ensemble of X-rays through the atmosphere, and accumulating statistics on what the measured result would be. This is compared to the simulated emission characteristics in order to develop a method of deconvolving the effect of the atmosphere from the data.

The simulation is best done using a Monte Carlo calculation since the interactions are not deterministic. The technique is to generate individual X-rays from a source with an initial energy and trajectory, **k**, and to follow each of these through all intercations. The results of any interaction is determined by random sampling of the distribution that represents the probability for all the possible outcomes for that interaction. For instance, the random variable for the photoelectric interaction would be the distance for absorption to occur, and the governing distribution would be;

$$P(z) = \exp(-\int^{z} \sigma \, \rho(z) \, dz) \tag{2.6}$$

where P(z) is the probability that the photon is not absorbed by the height z, σ is the mass attenuation coefficient, and ρ is the density. (See Appendix A)

The symmetry about the detector makes cylindrical coordinates a natural choice. The top is the emitting plane at 100 km, and the bottom is arbitrarily chosen to be at an altitude corresponding to about 20 g/cm^2 of overburden. The bottom could be at the corresponding balloon elevation, but there is a small backscatter component. The horizontal extent is 150 km in radius, and the detector is at the center of the 4 g/cm^2

layer, which is the nominal altitude of the balloon. This horizontal extent is much greater than the imager viewing area in order to examine the possible effect of X-rays which come from large distances before scattering into the detector's field-of-view.

The atmospheric parameters are taken from the US Standard Atmosphere [1979], which assumes a plane parallel geometry. The hydrostatic equation and the ideal gas law give the density as a function of height;

$$\rho(z) = \rho_0 \left[1 + \frac{z\Gamma}{T_0} \right]^{1 - \frac{g}{R\Gamma}} \tag{2.7}$$

where the temperature, T, has a linear height dependence, $T = T_0 + \Gamma z$; Γ is the lapse rate (temperature gradient), g is the acceleration of gravity at sea level, and R is the gas constant. The factor, $\frac{g}{R\Gamma}$, is much larger than unity so (2.7) is approximated by,

$$\rho(z) = \rho_0 \, e^{\frac{-z}{H}}, \tag{2.8}$$

where H is the scale-height. H is a weak function of z, so for thin layers H can be taken to be constant within any layer, but changes from layer to layer. This simplifies the calculation and also sets an upper limit on the layer thickness.

Equation (2.7) is averaged over a given layer when used with (2.6) to test for the occurrence of an interaction somewhere within the given layer. If there is an interaction another random sampling is done to find out if it is a Compton scattering or an absorption. A scattering necessitates a further calculation using (2.7) to find the exact position. If the interaction is photoelectric, the exact position is not important and the process simply starts over for a new photon.

For a Compton collision, the new trajectory and energy, $\mathbf{k}$, are found from the distribution given by (2.8) and (2.9). Equation (2.8) is obtained by integrating the Klein-Nishina cross section in Eqn. (A.2).

$$\sigma(x,\ \mathbf{k}) = \pi r_0^2 \left[\frac{1}{2\alpha} - \frac{1}{2\alpha(1+\alpha+\alpha x)^2} + \frac{\alpha^2 - 2(1+\alpha)}{\alpha^3} \log(1+\alpha+\alpha x) + \frac{1-x^2}{\alpha(1+\alpha+\alpha x)} + \frac{2}{\alpha^2}(1+x) \right] \quad (2.9)$$

$$k_{scatt} = \frac{k_0}{1+\alpha(1+x)} \quad (2.10)$$

$$x = -\frac{\mathbf{k}_{scatt} \cdot \mathbf{k}_0}{k_0\, k_{scatt}}$$

where $\alpha = \dfrac{k_0}{m_e c^2}$ and k_0 is the photon's original energy. The vector $\mathbf{k}$ expresses the photon's energy and trajectory in spherical coordinates, $\mathbf{k}=(E, \theta, \phi)$, $k = |\mathbf{k}| = E$.

A region of 5 km radius, corresponding roughly to the size of a pixel mapped to the emitting plane, is used as the source region for the calculation. In order to obtain reasonable statistics and to minimize computer time, an ensemble of X-rays is generated once for this single 5 km radius region and all further results are obtained by random sampling this ensemble. To extend the calculation to the entire emitting region, the results of this sub-region are replicated throughout the entire emitting plane with the appropriate coordinate transformations. This latter step is necessary to study the Compton scattered component only, since the direct component impinging upon any one pixel arises from the original 5 km radius region. The X-ray source population was assumed to be isotropic.

2.2.6. Atmospheric Response

The results of the above calculation are not yet in the form necessary for inverting the data, since the calculation yields the atmospheric response, while it is the inverse of this that is required. The procedure to achieve this will be discussed in this section, with the formulation being kept quite general at first and then narrowing to a realizable means of solution, using either physical reasoning or details of the application to the problem at hand.

The conversion from the response function to the the inversion function comes about in the following way. The measurements, $Q(\mathbf{k}; \mathbf{x})$, are assumed to be related to the source, $S(\mathbf{k}'; \mathbf{x}')$, through the relationship

$$Q(\mathbf{k}; \mathbf{x}) = \int d\mathbf{k}'\, d\mathbf{x}'\, F(\mathbf{k}, \mathbf{k}'; \mathbf{x}, \mathbf{x}')\, S(\mathbf{k}'; \mathbf{x}') \qquad (2.11)$$

where $F(\mathbf{k}, \mathbf{k}'; \mathbf{x}, \mathbf{x}')$ is the calculated response of the atmosphere, $\mathbf{k}$ is the previously defined energy-trajectory vector for the X-ray, and $\mathbf{x}$ is a position vector of a point either in the source (object) or image planes. Primed quantities are source variables. A similar functional relationship is assumed to hold for the inversion of the data to obtain source characteristics;

$$S(\mathbf{k}; \mathbf{x}) = \int d\mathbf{k}'\, d\mathbf{x}'\, G(\mathbf{k}, \mathbf{k}'; \mathbf{x}, \mathbf{x}')\, Q(\mathbf{k}'; \mathbf{x}') \qquad (2.12)$$

where $G(\mathbf{k}, \mathbf{k}'; \mathbf{x}, \mathbf{x}')$ is the inversion integral kernel which is related to the atmospheric response function by

$$\delta(\mathbf{k}-\mathbf{k}')\,\delta(\mathbf{x}-\mathbf{x}') = \int d\mathbf{k}''\, d\mathbf{x}''\, F(\mathbf{k},\mathbf{k}'';\mathbf{x},\mathbf{x}'')\, G(\mathbf{k}',\mathbf{k}'';\mathbf{x}',\mathbf{x}''); \quad (2.13)$$

$\delta(\mathbf{k}-\mathbf{k}')$ $\delta(\mathbf{x}-\mathbf{x}')$ are Dirac delta functions. Equation (2.13) is obtained easily from (2.11) by multiplying it with $G(\mathbf{k},\mathbf{k}';\mathbf{x},\mathbf{x}')$ and integrating over $\mathbf{k}$ and $\mathbf{x}$. Solving (2.12) will yield the inversion kernel, $G(\mathbf{k},\mathbf{k}';\mathbf{x},\mathbf{x}')$.

At this point it is reasonable to eliminate the dependence upon the variables θ' and ϕ', since the source has been modeled to be emitting isotropically. Likewise, the variables θ and ϕ can be eliminated as they are not dependent on $\mathbf{x}$ due to the pinhole collimation. This leaves only a single component of the X-ray vector, the magnitude k, which is better noted as E. Equation (2.13) is now reduced to

$$\delta(E-E')\,\delta(\mathbf{x}-\mathbf{x}') = \int dE''\, d\mathbf{x}''\, F(E,E'';\mathbf{x},\mathbf{x}'')\, G(E',E'';\mathbf{x}',\mathbf{x}''). \quad (2.14)$$

Equation (2.14) is a Fredholm integral equation of the first kind, and a way to solve this is to attempt a separation of variables for the atmospheric response function, $F(E,E';\mathbf{x},\mathbf{x}')$, [*Arfken*, 1985];

$$\begin{aligned} F(E,E';\mathbf{x},\mathbf{x}') &= F_E(E,E')\,F_x(x,x')\,F_y(y,y') \\ &= F_E(E,E')\,F_r(r,r')\,F_\Phi(\Phi,\Phi') \end{aligned} \quad (2.15)$$

where (r,Φ) are the polar coordinates for the points being imaged. The above separation cannot be rigorously done, but a similar operation can be performed that provides the desired computational convenience and is still a good approximation. The starting point for this decomposition is to write

$$F(E,E';\mathbf{x},\mathbf{x}') = F_{direct}(E,E';\mathbf{x},\mathbf{x}') + F_{scatt}(E,E';\mathbf{x},\mathbf{x}'). \quad (2.16)$$

The first term on the right is the part of the beam which has reached the detector directly. This part will undergo attenuation but will contain no X-rays which have scattered into the beam from other directions. The second term on the right side contains the information on the component scattered into the beam direction. It is important to note that the data itself is not decomposed, only the integral-kernel. The attenuation of the beam is a function of energy and the distance traveled. Since the direct component contains no transformations in trajectory and there is only attenuation without a change in energy, the direct term in (2.15) can be written

$$F_{direct}(E,E';\, \mathrm{x},\, \mathrm{x}') = A(E',r')\ \delta(E-E')\ \delta(r-r')\ \delta(\Phi-\Phi'). \qquad (2.17)$$

The delta functions reflect the direct mapping of the source photons to the corresponding pixels in the image plane, while the factor $A(E',r')$ expresses the energy and path-length dependent attenuation of the beam.

The scattered component cannot be treated in the same way since Compton collisions result in an energy dependent change in trajectory; the variables are not separable. This component to the problem is most effectively treated by first separating out the effects that will have the largest and/or most discernible effect on any measurements.

The Compton process is not dispersive to a beam of X-rays in the sense of many small angle collisions that widen the beam since the scattering angles are fairly uniformly distributed for the 20-120 keV energy regime. The process tends to form a weak uniform background relative to the unscattered photons of the beam. However, the attenuation of X-rays that traverse greater distances from the source to the detector will tend to emulate this effect of angular diffusion. This is more prominate for a region of enhancement that is considerably off-axis (i.e., a zenith angle greater than say, 35°).

Figures 2.11 illustrates this by separating the simulated unscattered component from the Compton component at the altitude at which the detector would be. The top 3-dimensional plot is the simulated source spatial distribution and the bottom 3-dimensional plot is the directions that the detector would perceive the photons to be coming from. The source X-rays are all 60 keV. Each square in the two plots is a little smaller than the size of a pixel, 3.5 km on a side and the total simulated region is 280 km on a side, which is actually much larger than the actual imager's field-of-view. The main result from this is that the source is quite localized, about 40 km off-axis from the detector, yet the scattering tends to smear out the incidence angles. The resulting image would have the unscattered component (the "true" image) superimposed on a "false" image similar to the one shown in the lower panel of Figure 2.11.

To see what the relative effects are for the Compton and unscattered components to the image, Figure 2.12 shows angular distributions (zenith angle in the upper panel; azimuth in the lower panel) at the simulated detector. The three lines in each panel represent; (1) the direct component ("true" image) of an enhancement at the same location as above, (2) the same scattered component as discussed above, resulting from the enhanced region, and (3) the quasi-uniform background component from the rest of the emission region. The latter results from the entire emission plane's scattering component that reaches the detector. In other words, (1) and (2) are the result of the point in the object plane and (3) is the result of scattered X-rays coming from everywhere but the object point. The enhancement is a factor of five more intense than the remainder of the region. Note that the zenith angle plot is not normalized by the solid angle; there is a sine dependence that results in a maximum to occur at around 45°. The net result of this is that the direct component is still well above the Compton contributions, and the smearing effect to the image (effect (2), above) is washed out by the more diffuse background (effect (3), above).

Applying this reasoning to the inversion problem, it is evident that the scattered photons which enter a small solid angle at the detector can originate anywhere in the emitting plane. There is very little localization of the source for the Compton contribution to any one pixel. Little information is available regarding source characteristics from this component. Inverting the transformation of the scattered X-rays from their original trajectories and object-plane positions to the final trajectories and image positions are computationally difficult for a result that is probably non-unique. Therefore this will not be done, rather an attempt will be made to understand the amount of degradation to the images.

The neglect for the interdependence of the the transform $E \rightarrow E'$ and the transform $\mathbf{x} \rightarrow \mathbf{x}'$ during scattering interactions assumes that the energy spectrum is not a strong function of position. This could be a serious problem except that the $E \rightarrow E'$ process is not very strong for the 20 to 100 keV energies. For example, using Eqn. (2.10), the greatest change in energy for a 60 keV X-ray will be a degradation to 50 keV, corresponding to a 180° deflection. The average change is closer to 4 keV, giving a new photon of 56 keV. In this sense, scattering is a second order effect, the direct component being first order, and it is now assumed that the degree of spatial variation due to the scattered component of the spectrum will only result in a second order effect.

Combining (2.16) and (2.18), the inversion now is a function of energy only and is stated as;

$$\delta(E - E') = \int dE''\, F(E,E'',r')G(E',E'',r') \tag{2.18}$$

Obtaining the solution of such an integral equation is still a difficult task but can be made more tractable by considering the data to be discretely distributed, which is indeed the case for the measurements. Therefore, (2.18) can be cast into a matrix equation

$$\delta_{i,j} = F_{i,k}\, G_{k,j} \tag{2.19}$$

In (2.19), it is understood that $F_{i,k}$ and $G_{k,j}$ are each functions of r, by virtue of the above discussion. The diagonal elements correspond to the direct component and the off-diagonal elements would represent the scattered contribution, which in our ordering are all 0.

Finally, the inversion of the measurements to obtain the source characteristics is obtained as;

$$S_i = G_{i,j}\, Q_j. \tag{2.20}$$

In (2.20) Q_j, is a column vector from each pixel, and represents the energy spectrum measured by that pixel during some time interval.

In terms of practical use of (2.20), a set of inversion matrices, $G_{i,j}$, is calculated from (2.18) for several different solid angle directions. The output of each pixel is represented by an energy-spectrum vector which is then operated on by the appropriate inversion matrix to obtain the corresponding vector for the source. The final image is than constructed from these energy-spectrum vectors.

2.2.7. Relation to Electron Spectrum

The above scheme for the deconvolution of atmospheric effects on the X-rays has still not given us the parent electron spectrum. The physics of the bremsstrahlung process is described by the cross section for an interaction of an electron in the Coulomb field of an nucleus. This can be approximated classically [*Jackson*, 1975], but is correctly approached quantum mechanically, although the calculation of the matrix elements is of sufficient difficulty to only result in various approximations (see, for example, *Koch and Motz*, [1959]). Using the appropriate approximation for the cross sections, a Monte Carlo calculation for the spectrum resulting from test electrons colliding with test atmospheric particles could be performed. This calculation is not performed here, however there are some general relationships that can be drawn between the bremsstrahlung X-ray spectrum and a parent electron spectrum.

Figure 2.13 shows a result of *Barcus and Rosenberg*, [1966], who studied the ability to infer electron spectra from bremsstrahlung x-ray spectra. These results were not meant to indicate an exact correspondence between the two quantities, rather to demonstrate the ability to make good qualitative judgements about the electron spectrum. A procedure adopted by *Pilkington*, [1972], is to assume a six-parameter electron spectrum of the form $A\,exp(-E/E_1) + B\,\delta(E - E_2) + C\,exp(-E/E_3)$, and use semi-classical thick-target bremsstrahlung theory to estimate what three parameters will reproduce the measured X-ray spectrum. Using this procedure, it was found that very high resolution X-ray spectroscopy is needed to infer the fine structure in the electron spectrum.

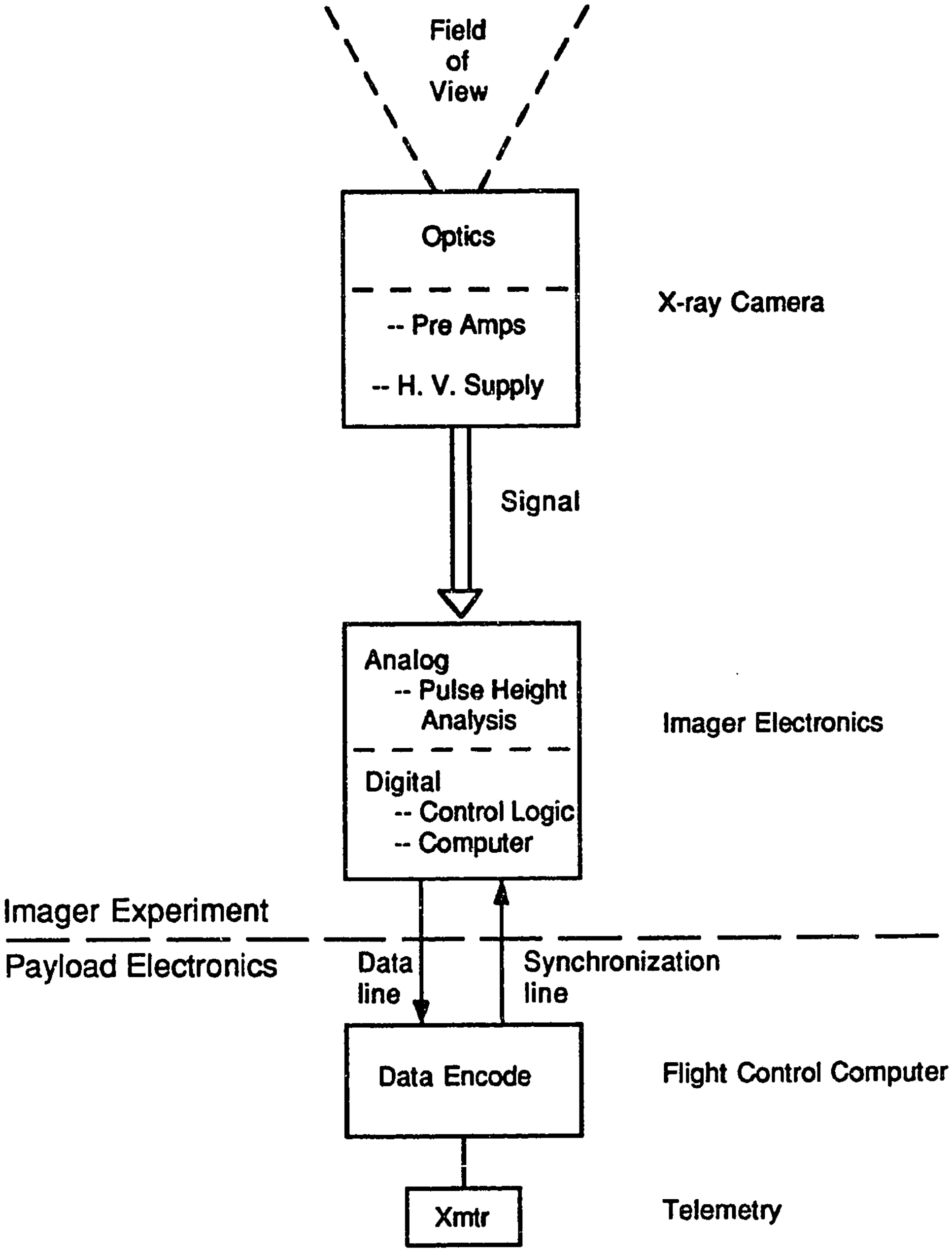

Figure 2.1 Imager block diagram.

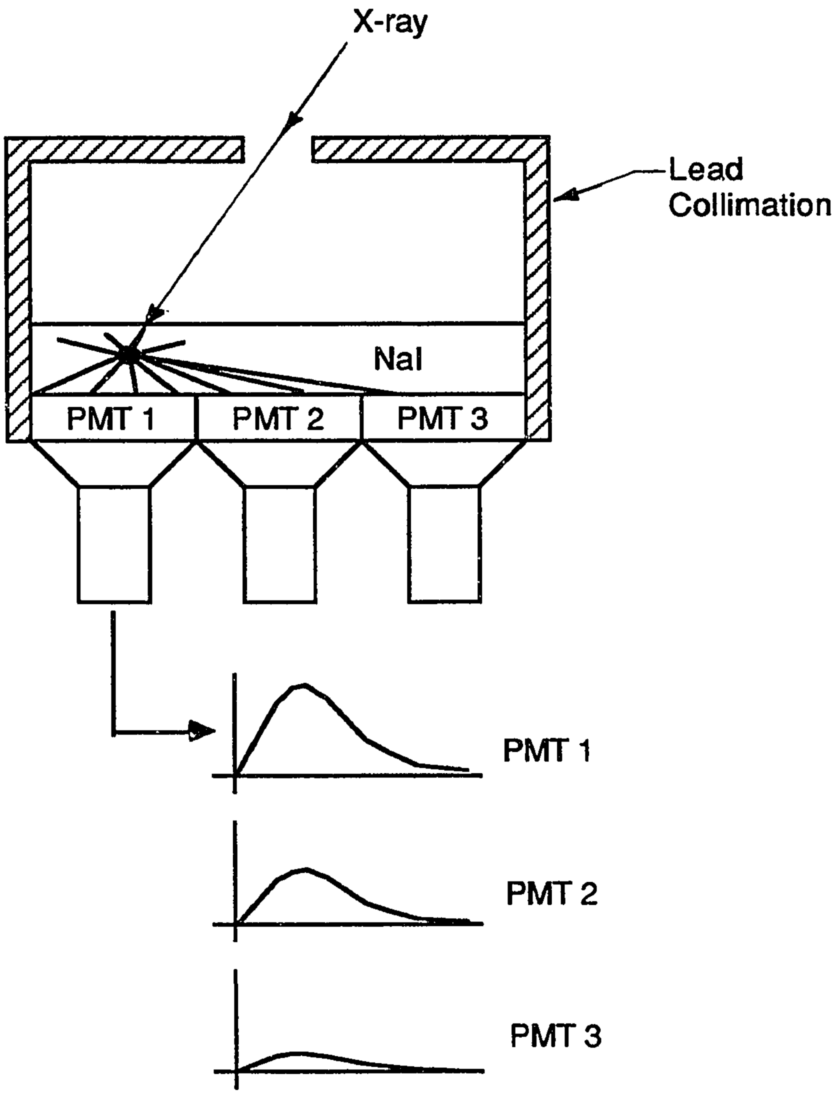

Figure 2.2 Anger camera schematic.

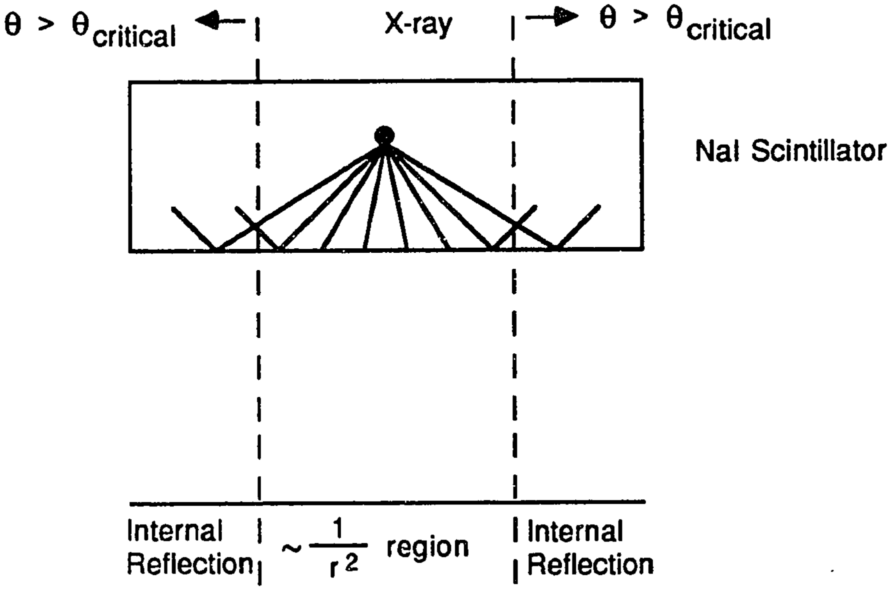

Figure 2.3 Scintillation light spreading in imager optics.

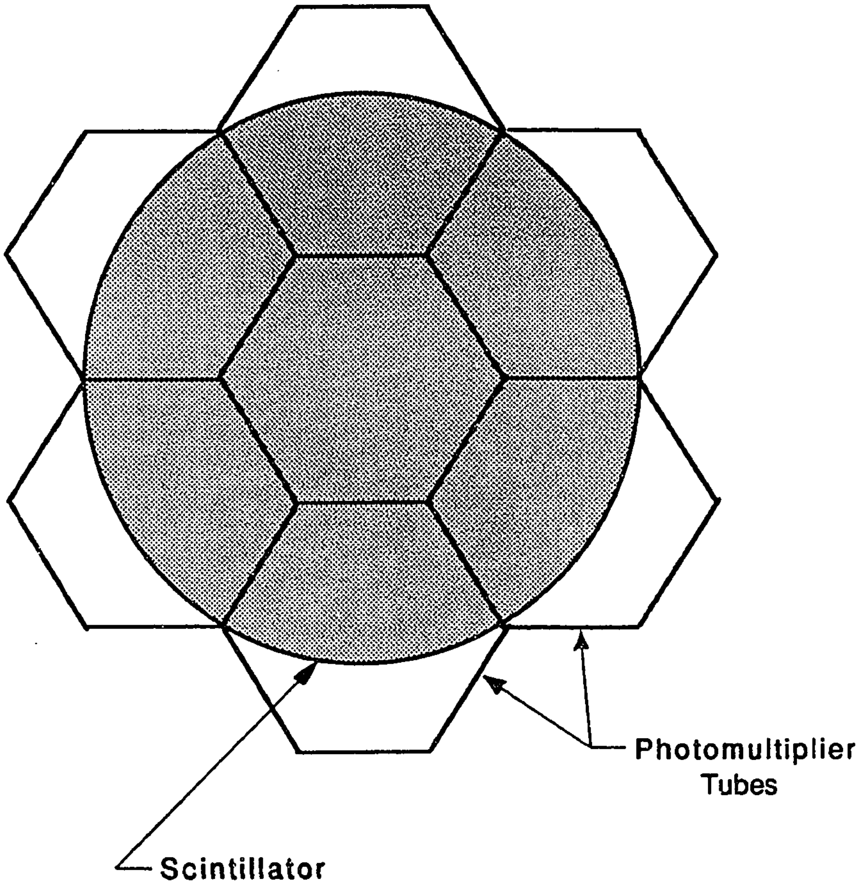

Figure 2.4 New Imager: Top View.

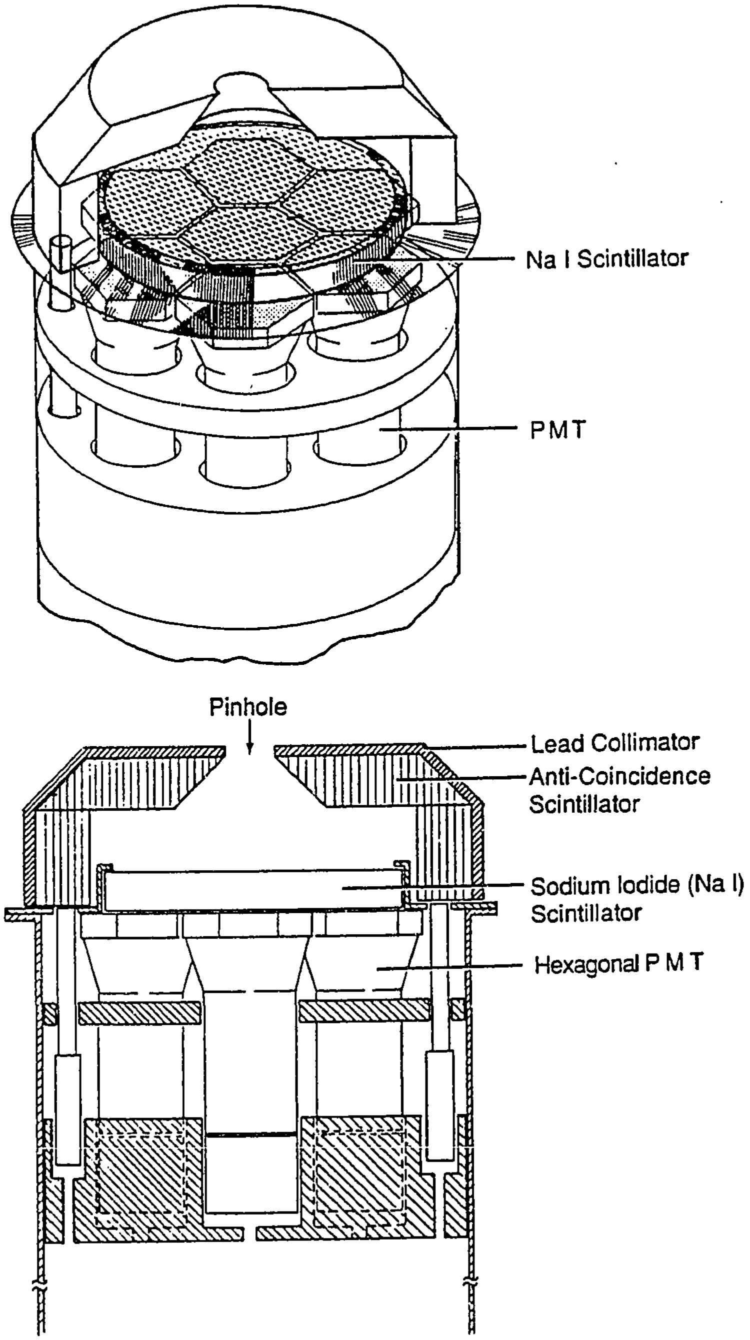

Figure 2.5 Pseudo-Optics: Side and top views.

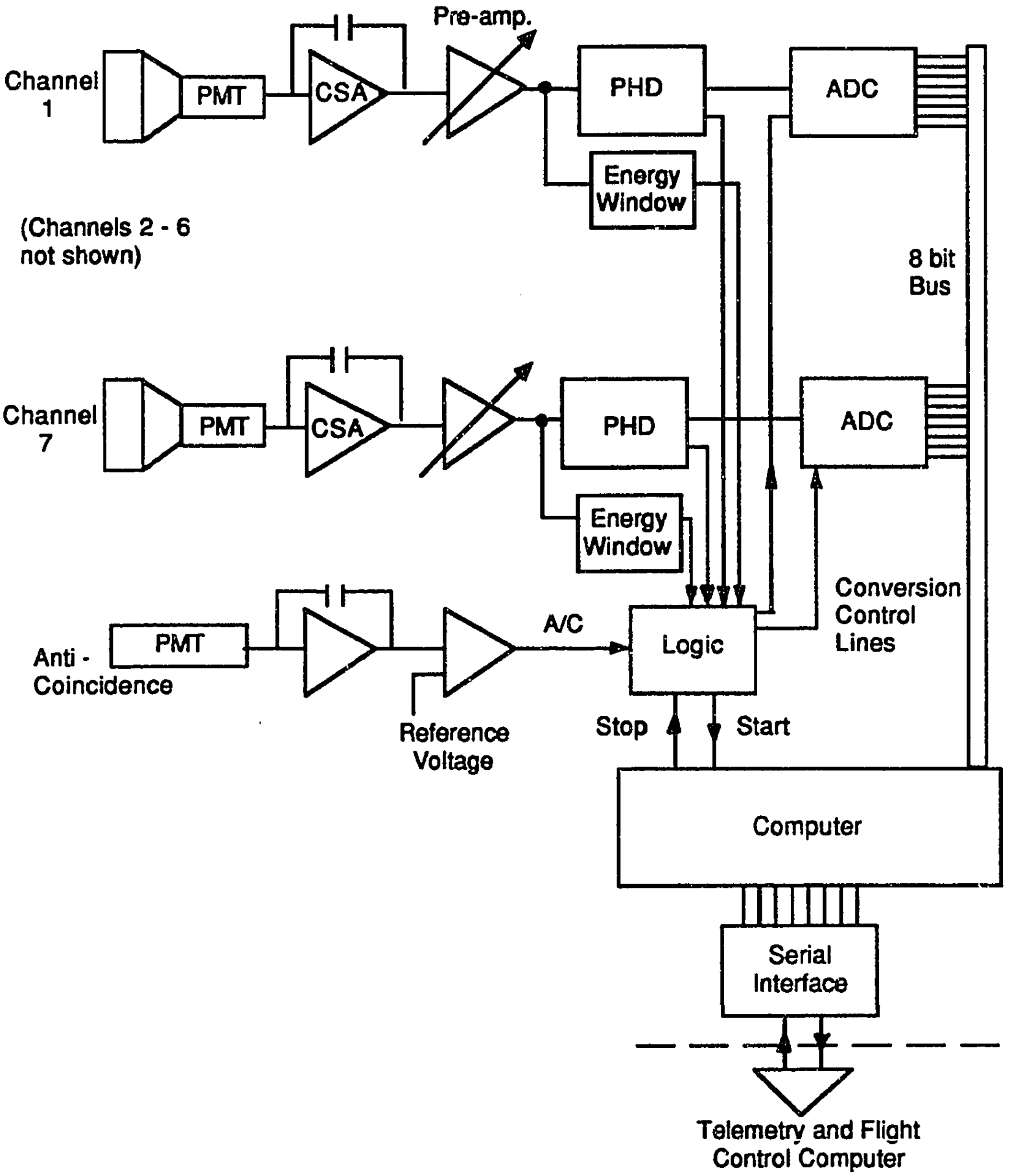

Figure 2.6 Electronics block diagram.

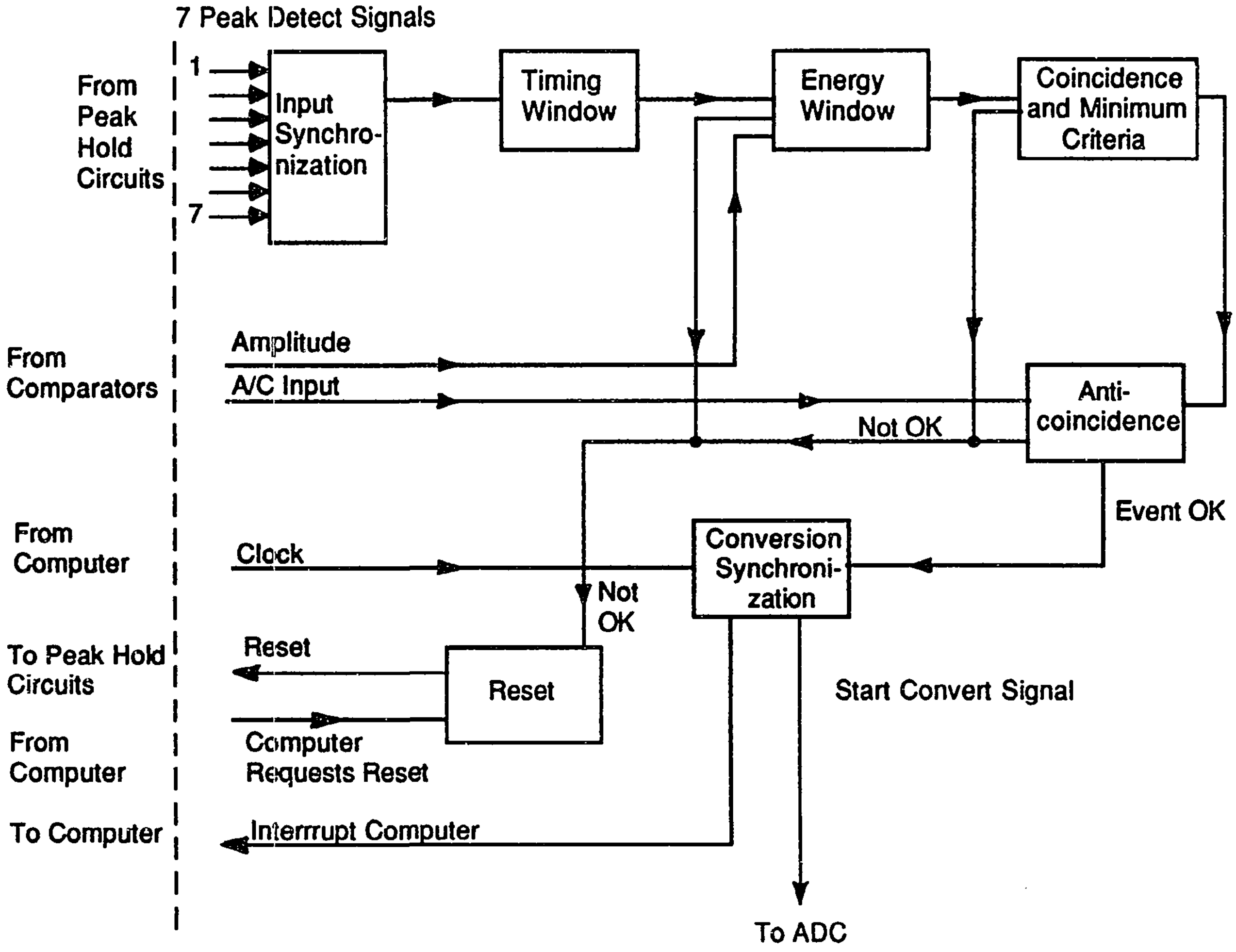

Figure 2.7 Logic evaluation for X-ray event processing.

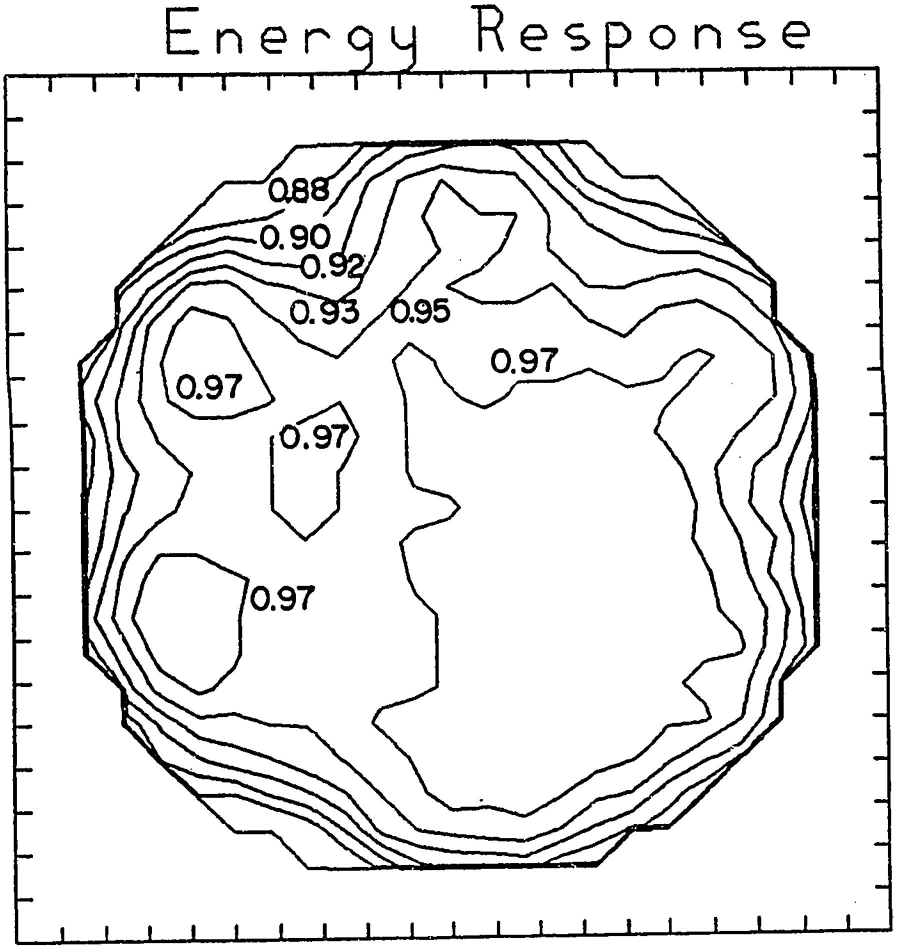

Figure 2.8 Spatial dependent energy response for 66 keV X-rays.

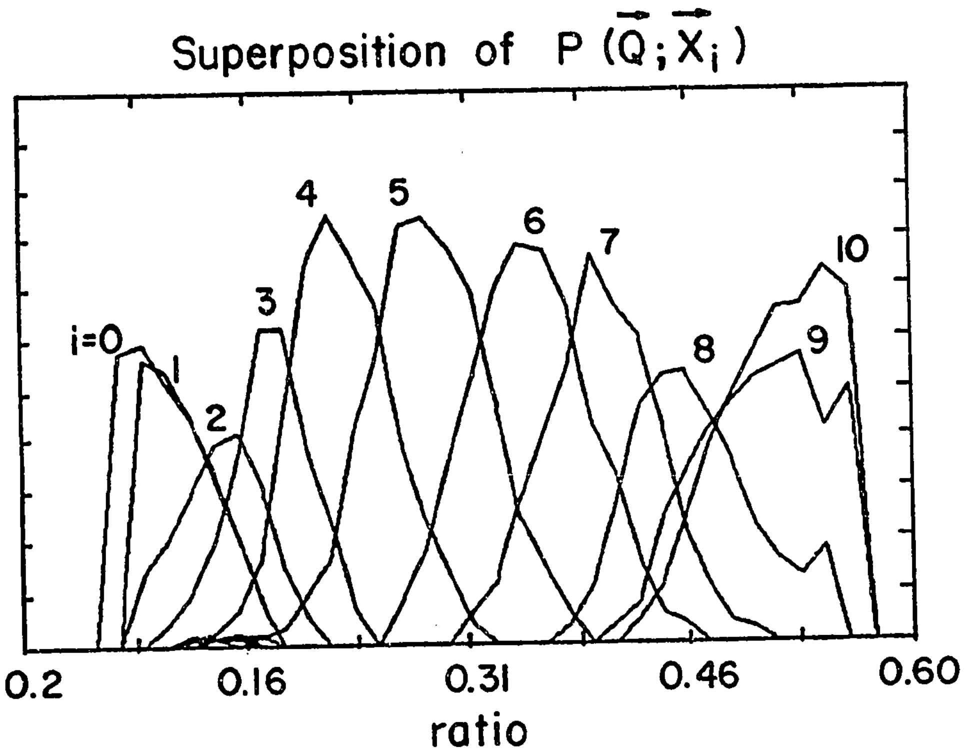

Figure 2.9 Calibration response along a line of constant radius.

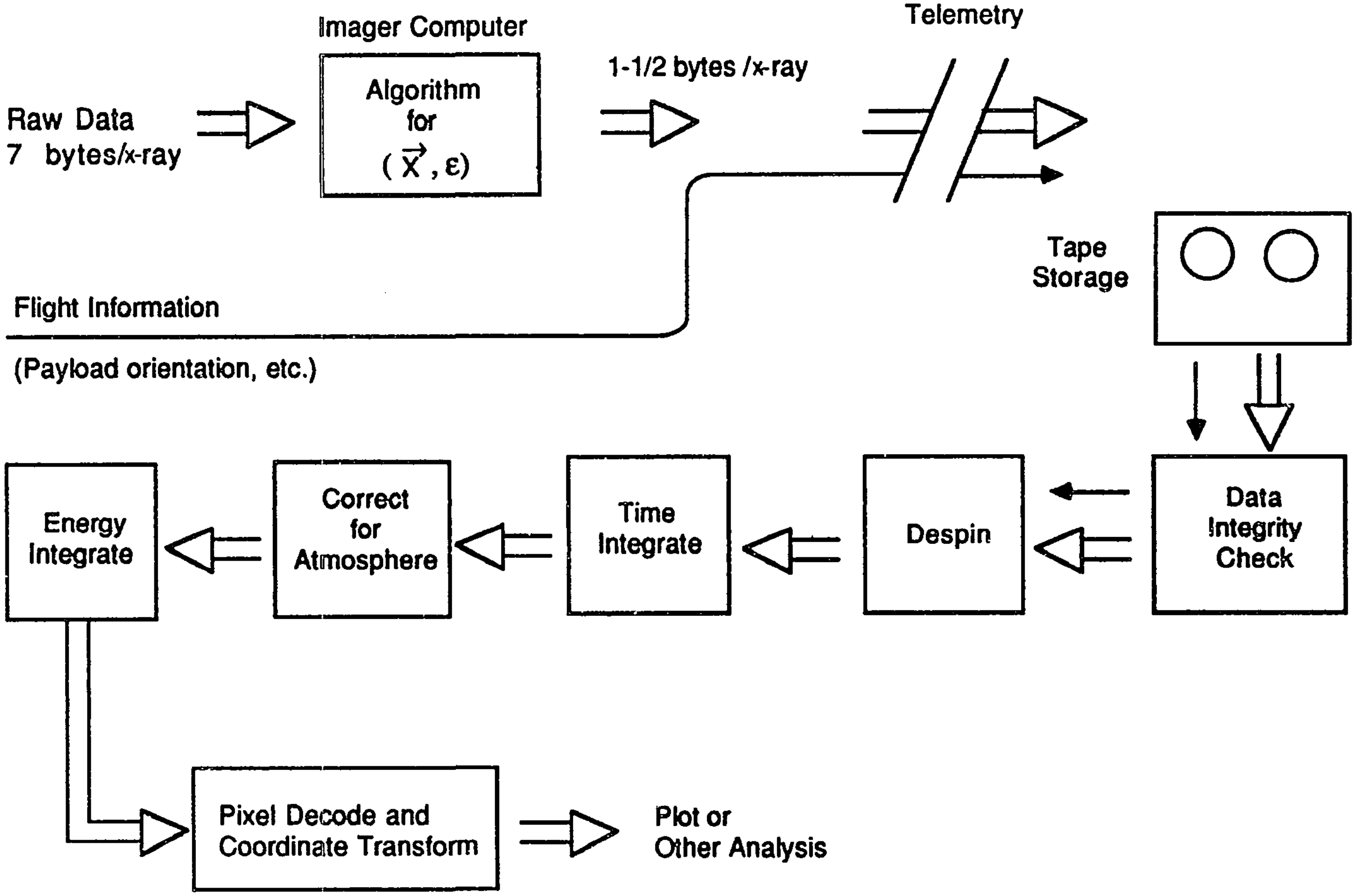

Figure 2.10 Image production flow chart: Ground data processing.

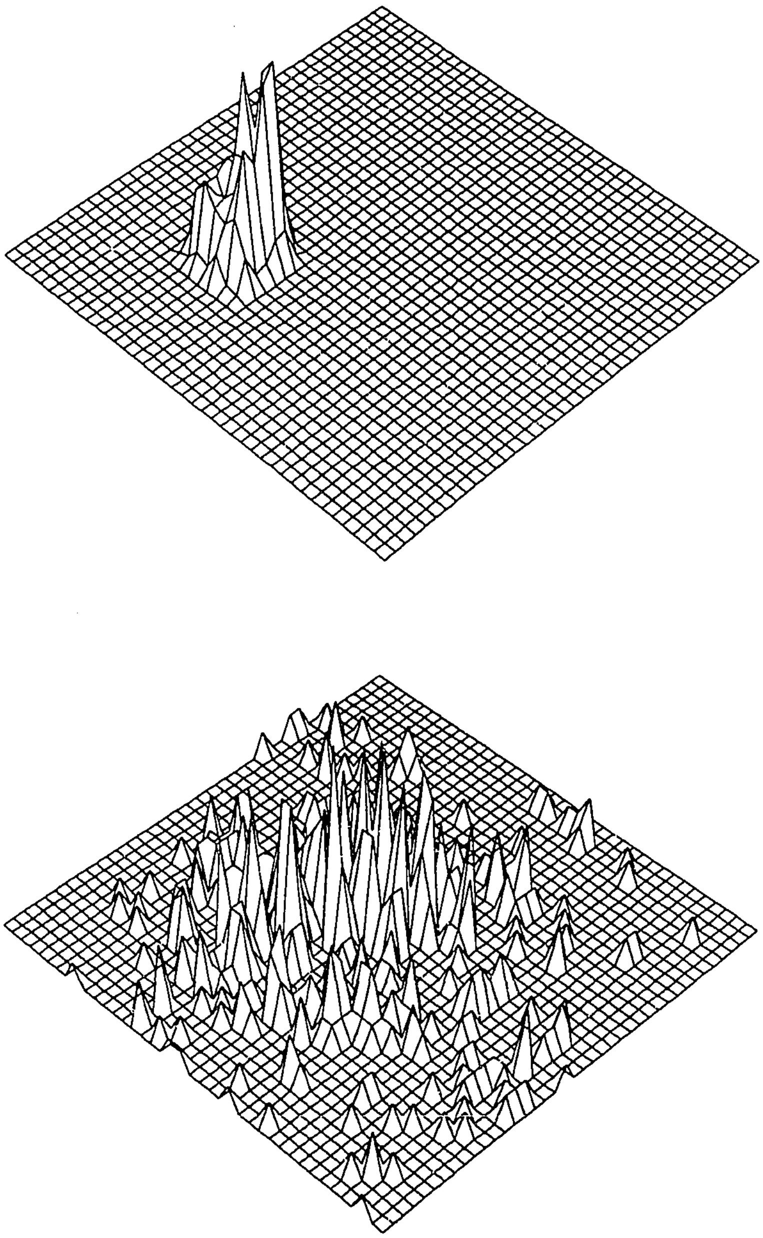

Figure 2.11 Compton Degadation of an Image for a localized emitting region. Upper panel is the distribution of source emitters that Compton scatter into the field-of-view of the detector. Lower panel is a distribution of where the X-rays appear to be coming from.

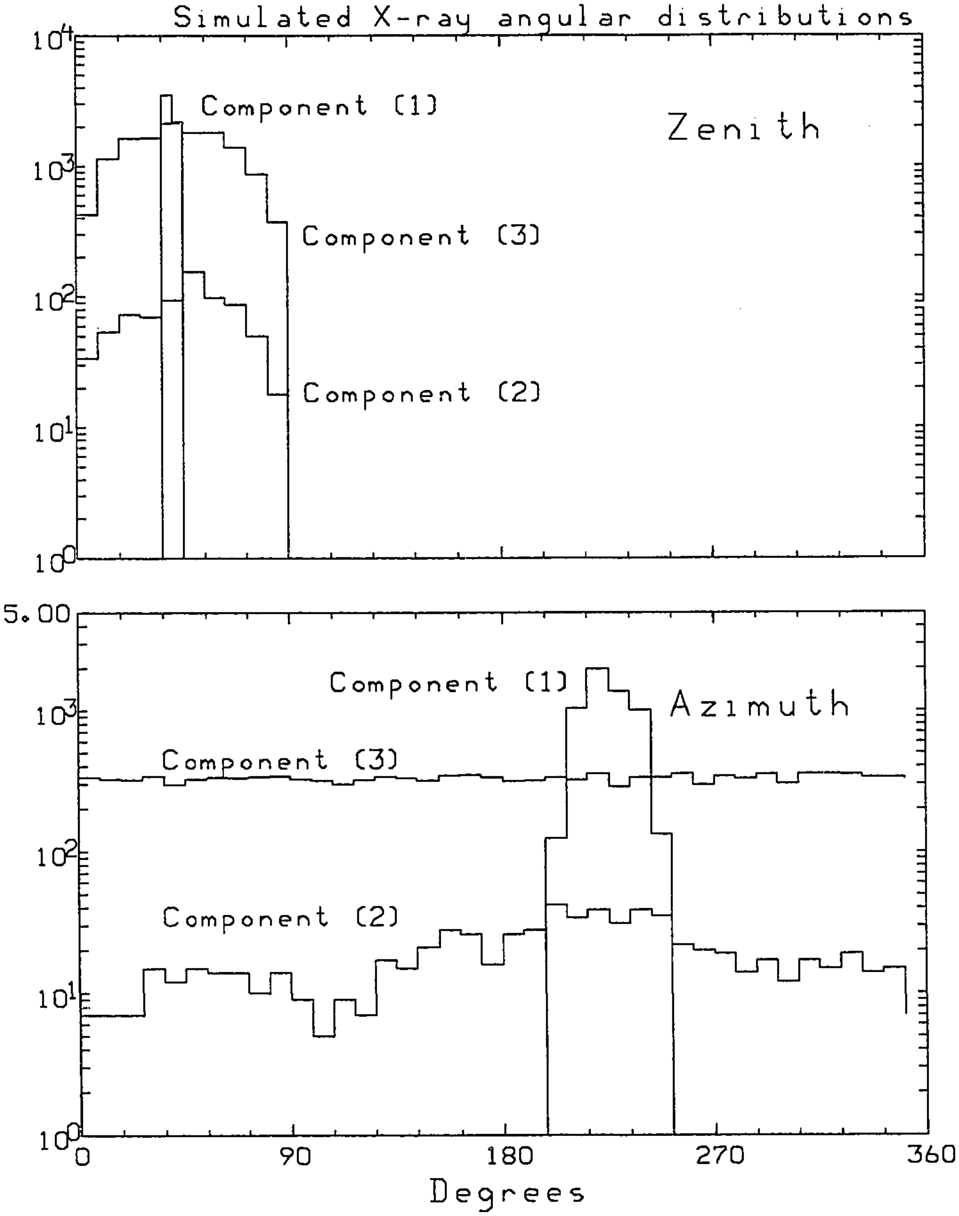

Figure 2.12 Angular distribution for detected X-rays, separated into scattered and unscattered components for a region of intensity enhancement being imaged. (1) are the unscattered X-rays that are detected, (2) the scattered component that comes from an object point being imaged, and (3) is the diffuse contribution arising from all other emitting points out of the filed-of-view that scatter into the field-of-view of the detector.

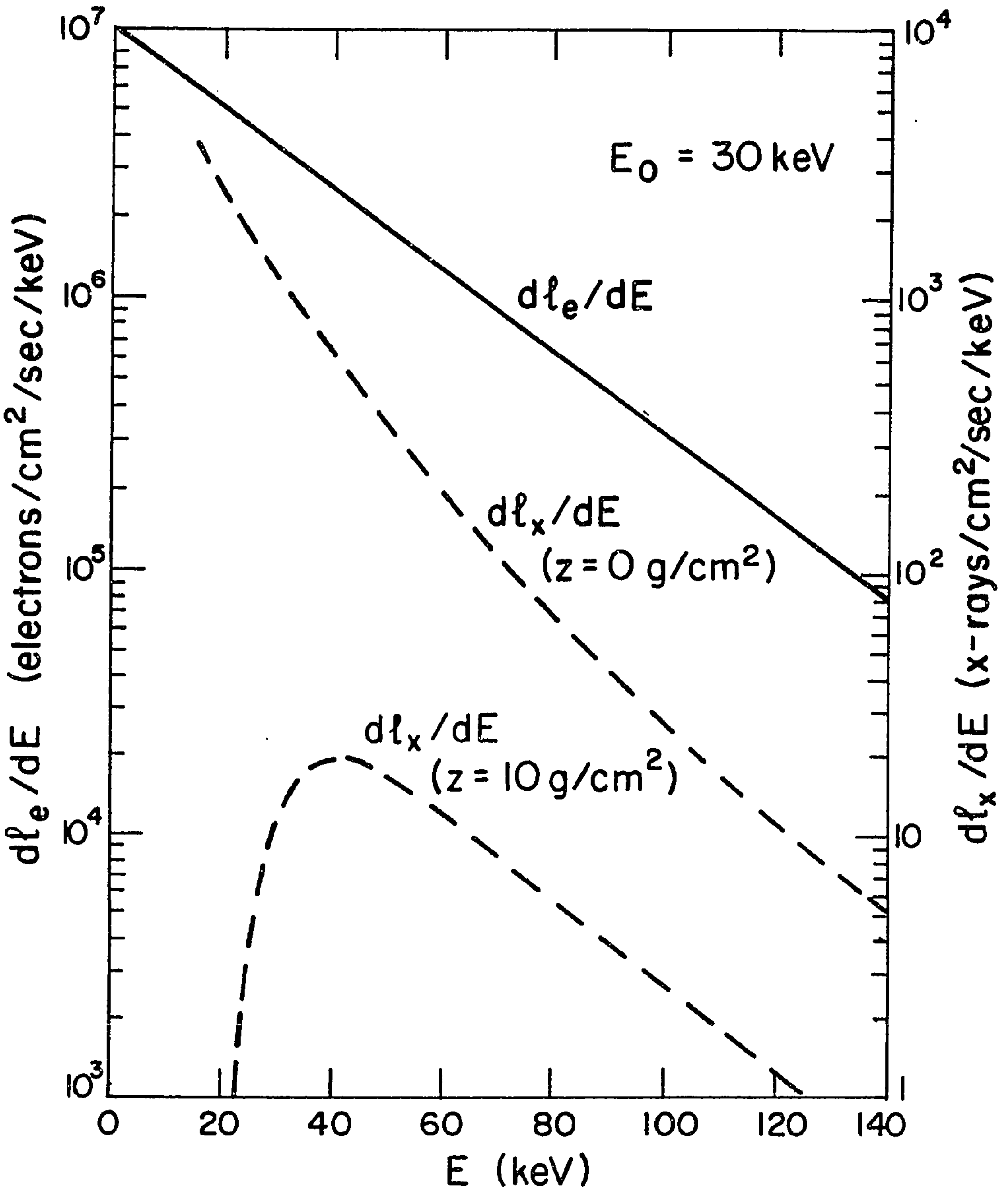

Figure 2.13 Relationship of X-ray to electron spectrum. From *Barcus and Rosenberg* [1966].

Chapter 3

Morning Sector Electron Precipitation

3.1. Introduction

The mechanism by which Earth's magnetosphere dissipates excess energy is a central goal of magnetospheric research. Such a mechanism has two conceptual components; the introduction of fresh hot plasma into the inner magnetosphere and the decay of this energy through particle precipitation and ionospheric Joule heating. There are different time scales associated with these processes ranging from the near simultaneous deposition of energy to the nightside auroral atmosphere, to a delayed process of slowly transporting the energy to other regions of the magnetosphere before dissipation. Much of the excess energy in the inner magnetosphere is contained in the plasma and therefore observing plasma flow provides a good method of tracking the transport of energy to other regions of the magnetosphere. The forces which control plasma flow and particle drifts are fairly well understood, thus identifying the time and region for the introduction of hot plasma into the inner magnetosphere should allow the determination of energy transport to other regions. By studying this transport and the details of the various energy sinks, a more complete picture of the mechanism for magnetospheric relaxation can be obtained.

The broad goal of understanding magnetospheric energy dissipation has resulted in investigations of many of the finer details which are involved in this process. One such focus has been on the physics of how the newly energized plasma is brought into the middle or inner magnetosphere. Two broad categories of models are the injection boundary model [*McIlwain*, 1974; *Konradi*, 1975; *Mauk and Meng*, 1983] and the Alfven layer model [*Walker and Kivelson*, 1975; *Kay and Kivelson*, 1979; *Kivelson*, et al., 1980]. The injection boundary model originally postulated the existence of a dispersionless boundary, tailward of which contained the recently energized plasma, however, the longitudinal extent of the boundary has now been suggested to extend duskward as far as 1700 LT and dawnward to 1040 LT [*Newell and Meng*, 1987], and possibly even circling the Earth [*McIlwain*, 1985]. The Alfven layer model advocates the existence of time dependent electric fields which alters existing steady-state drift paths of particles in the inner magnetosphere. Both models assume similar drift paths after the initial appearance of the particles and only differ in the way the particles achieve their initial configuration before adiabatic drifting.

The study of drifts of energetic particles in the magnetosphere is a logical continuation of the injection problem. This has been carried out experimentally [*DeForest and McIlwain*, 1971; *Pfitzer and Winkler*, 1969] and by performing single particle orbit calculations in various magnetic and electric field configurations. For instance, *Ejiri* [1978], used a dipole magnetic field and steady convection electric field to model 90 degree pitch angle proton and electron drift orbits. *Meng and Akasofu* [1983] extended the Ejiri calculations to explain the mantel aurora, the precipitation of electrons at sub-auroral latitudes on the dayside. The deficiency in these drift orbit calculations is that they are not self consistent and do not adequately model the time dependent or loss processes involved.

The mechanism that allows particles to be lost from the magnetosphere is widely thought to be a collisionless diffusion process in which wave activity scatters particles into the loss cone, with subsequent loss to the atmosphere. Wave particle interactions has an extensive theoretical and experimental background. *Kennel and Petschek* [1966] first developed the theory of whistler wave growth in regions of pitch angle anisotropy as a self consistent means of limiting trapped radiation fluxes. Further work by *Kennel* [1969] defined two limiting cases for pitch angle diffusion without specification of the resonant wave mode: In weak diffusion the loss cone is nearly empty, so the diffusion coefficient, and hence the precipitation rate, is proportional to the wave spectral density. For strong diffusion the loss cone is nearly full, and the loss rate is independent of the diffusion coefficient and wave amplitude. The pitch angle diffusion theory requires knowledge of the wave amplitude which is not obtainable with linear plasma theory. Without a general theory for wave amplitudes, or more correctly, for wave saturation levels, it is difficult to specify the waves responsible. Linear kinetic instability analysis will provide a growth rate, which is a necessary but not a sufficient requirement for a particular wave mode to be the causal agent in pitch angle diffusion.

Different wave modes have been proposed for different electron energy regimes: Low energy electrons (0.1-10 keV) associated with the diffuse aurora have been attributed to the electrostatic electron cyclotron mode [*Lyons*, 1974]. Nonrelativistic electrons are thought to interact with the whistler mode, although a direct experimental confirmation is stronger for coherent or narrow band whistlers [*Chang, et al.*, 1983] rather than the more commonly observed broad band "chorus" or "hiss". Broad band wave activity is often seen in in conjunction with enhanced magnetic activity and on the dayside of the magnetosphere [*Burton and Holzer*, 1974; *Maeda et al.*, 1978]. *Kremser et al.*, [1986], found fair agreement between auroral bremsstrahlung X-rays and VLF wave activity at GEOS 2 near local midnight. Relativistic (> MeV) electron pitch angle diffusion has been theoretically attributed to Doppler shifted ion-cyclotron resonance at the plasma pause [*Thorne and Kennel*, 1971], and there has been some confirmation of this [*Vampola*, 1971].

Morning sector particle precipitation has long been associated with the nightside manifestations of the substorm and as such is viewed as an extension in time and space of the energy dissipation process [*Akasofu*, 1968]. The association between nightside ground magnetograms and morning sector bremsstrahlung X-rays was used by *Kangas, et al.* [1975] to establish the delayed response as consistent with a picture of drifting particles from a nightside source. *Meng and Akasofu* [1983] made a similar connection between the observation of electron fluxes at low altitude in the morning sector and the magnetogram-determined substorm onset near local midnight. *Hones, et al.*, [1971] studied the evolution of substorm features at several local times with the use of riometers, spacecraft, and balloon instruments, and found generally good agreement between the local times of onset and the expected drift times for 100 keV electrons. However, *Hones et al.*, [1971] also found precipitation variations in the noon sector which were unexplainable in terms of electron flux variations.

The theoretical connection between the presence of electrons in the morning sector magnetosphere and the precipitation of these through wave particle interaction has been studied by *Jentsch*, [1976] and *Lucas and Brice*, [1973]. *Lucas and Brice*, [1973] found that the measured electron pitch angle distribution in the morning sector were more unstable to whistler wave growth than midnight electron populations. *Jentsch*, [1976], studied the theoretical evolution of electron pitch angle distributions resulting from drifts from a midnight source region and concluded that whistler mode wave particle interaction was a likely cause of pitch angle diffusion and precipitation.

The goal of this work is to make a detailed study of the relationship between particle precipitation on the dayside and the drift of electrons from a nightside source region. The energies of the electrons being studied here (>20 keV) are well above observed auroral potential structures, so we do not consider this to be an important influence. The process that precipitates the drifting, quasi-trapped electrons is assumed to be wave particle induced pitch angle diffusion in the manner of *Kennel* [1969]. By examining the temporal behavior and energy characteristics of geosynchronous electrons at three widely separated local times in conjunction with ground and balloon observations, further knowledge is obtained on the wave-particle interaction region. It is found that an extremely intense, long duration emission of bremsstrahlung X-rays at subauroral latitudes on the dayside is best explained as a change in the pitch angle diffusion process rather than resulting from a change in the electrons drifting into the region. The electrons that are precipitating are possibly trapped (i.e., have executed a complete azimuthal drift), but more likely resulted from the nightside source continuing to supply hot plasma for an extended period of time.

The impulsive nature is found to not be explainable in terms of a simple picture of drift-induced anisotropies leading to wave growth, but rather seems to require further attention to the details of the scattering mechanism.

3.2. Data

The data to be used in this study are composed of spacecraft omnidirectional differential electron fluxes (Los Alamos-Department of Defense) and magnetometer measurements (GOES-5,6) at geosynchronous orbit and Viking UV images, ground magnetometer, riometer, and balloon X-ray and electric field data. The X-ray data are from the UW imager experiment and balloon borne X-ray spectrometer flown by the Space Research Institute (SRI) of Graz, Austria. The particle data from the three geosynchronous spacecraft allow the progression of the drifting energetic electrons (30-1400 keV) to be observed in space and time on the L = 6.6 shell, while the balloon data will provide a sampling of the loss-cone particles from a slightly lower L shell, and a local time between two of the geosynchronous satellites. The riometer data will be used to investigate large scale spatial effects in the dayside precipitation. The magnetometer data will serve to augment the nightside electron flux data in the identification of substorm onset and energy deposition to the near midnight auroral zone. Figure 3.1 shows a map of the magnetosphere and satellite positions at 900 UT, 27 July 1988. The local time locations of the Los Alamos (LA) spacecraft at 1000 UT are: s/c 84-037 at 1436 LT, s/c 84-129 at 2340 LT, and s/c 82-019 at 730 LT. GOES-5 and GOES-6 were located between the midnight region and the morning sector. The location of both balloons is close to 1030 LT. The two riometer stations are on the same meridian but different L shells, and about one hour later in local time from the balloons. These ground station and balloon locations are shown in Figure 3.2. The ground magnetometer data comes from College, Alaska, which is at LT 0030. Table 3.1 summarizes these experiments.

Table 3.1 Experiment locations.

Experiment	Geographic Latitude	 Longitude	L-Shell	1000 UT Local Time
Ground and Balloon				
College Magnetometer	64.9	-147.8	5.4	0030
Kevo Riometer	69.8	27.0	6.2	1150
Sodankyla Riometer	67.4	26.6	5.1	1150
SRI Elec. Field, X-ray Spec.	67.9	7.2	5.4	1030
UW X-ray Imager	67.7	10.5	5.4	1040
Spacecraft				
LA-129, electron flux	0.0	-155.0	6.6	2340
LA-019, electron flux	0.0	-38.0	6.6	0730
LA-037, electron flux	0.0	69.9	6.6	1440
GOES-5, magnetic field	0.0	-74.0	6.6	0500
GOES-6, magnetic field	0.0	-98.0	6.6	0330
Viking, UV imager				Polar Orbit

Figure 3.3 shows the 24 hour overview of July 27, 1986 as determined by the horizontal component of the magnetic field at the College magnetometer. The four hour time interval, 800 - 1200 UT is expanded in Figure 3.4 for this same data, along with the magnetometer data from the two GOES spacecraft. Table 3.2 contains the sequence of events to be discussed in this section, ordered by time of occurrence in UT. Each entry also gives the location in LT, the observation, and the experimental

source for the data. There are entries in the table marked with a † which will be focused on in the discussion section. These correspond to observations which add new insight to the relationship between events occurring on the nightside and those on the dayside, or show features that are particularly important to the discussion.

Table 3.2 Chronology of magnetospheric events.

Time (UT)	Loc'n (LT)	Night Events	Day Events	Experiment
0832	0200	Magnetic Impulse		GOES-6
0840	2230	Broad-Band Injec.		LA-129
0846	0330	Magnetic Impulse		GOES-5
0850	0030	Auroral Bay start		College mag.
0850	0615		Injection - Dispersion	LA-019
0905	1030		X-ray Start	UW, SRI
0910	1030		X-ray Maximum	UW, SRI
0910	1345		Injection - Dispersion	LA-037
0915	1100		CNA Maximum	Sodankyla
0920	2300	Narrow-Band Injec.		LA-129
0930	0000	†		
0950	1140		CNA Maximum, L = 5.1	Sodankyla
0955	0130	Auroral Bay Max.		College mag.
1000	1150		CNA Maximum, L = 6.0	Kevo
1000	0330	Magnetic Impulse		GOES-6
1000	730		†	
1005	1100		X-ray Start	UW, SRI
1005	1100		South-North X-ray gradient	UW
1012	1110		Electric Field - Eastward	SRI
1015	0500	Magnetic Impulse		GOES-5
1015	1110		X-ray Maximum	UW
1015	0745		Injection - No Dispersion	LA-019
1020	745		†	
1025	0745		Injection - Mult., No Disp.	LA-019
1030	1150		X-ray Multiple Peaks	UW
1040	1435		†	
1050	1445		Injection - Mult., Dispers.	LA-037

† - Particularly noteworthy times, see text.

Geosynchronous Electron Characteristics

Low energy omnidirectional electron flux data for the energy channels 30-45 keV, 45-65 keV, 65-95 keV, 95-140 keV, 140-200 keV, and 200-300 keV from the three geosynchronous spacecraft are shown in Figures 3.5, 3.6, and 3.7, ordered in the direction of electron drift motion around Earth, starting at s/c LA-129 near midnight, in Figure 3.5. Figures 3.8, 3.9, 3.10 show the high energy electron fluxes (channels 200-300 keV, 300-400 keV, 400-600 keV, 600-900 keV, 900-1400 keV, 1400-2000 keV) for the same spacecraft as shown in Figures 3.5, 3.6, and 3.7, respectively. The sudden flux enhancements in all energy channels of the electron detectors of s/c LA-129 at 840 to 845 UT signals the introduction of fresh hot plasma into the inner magnetosphere, presumably from magnetotail processes, and by 950 UT the auroral electrojet has begun to respond. To be explicit in this work, the term injection will denote electron flux enhancements in several energy channels, with a possible further specification of 'broad band' or 'narrow band' to indicate whether the injection is sensed in all the detector energy channels or just the lower few.

The appearance of some energy dispersion in the 840 UT injection indicates the source was probably not at s/c LA-129, but the details of the source characteristics are not important for this study. At 920 UT another injection is apparent at s/c LA-129, although this one is somewhat more narrow in energy bandwidth. These events establish the start of dissipation processes in the the magnetosphere. The newly introduced plasma presumably starts to drift in accordance with the well understood principles of convection, curvature, and gradient drifts. The observations of energy dispersed flux enhancements at s/c LA-019 at about 850 UT and at s/c LA-037 at about 905 UT (Figures 3.6 and 3.7, respectively) are consistent with this picture of drifting particles, although the second injection does not result in an identifiable signature. The drift time is 30 minutes for 100 keV electron to drift 180 degrees in longitude at 6.6 Re.

There are two additional narrow band injections at s/c LA-129 at 1007 and 1040 UT which also leave no signature at any other spacecraft, including GOES-5,6. Note that the first injection at 840 UT is actually preceded by a magnetic impulse at GOES-6 by several minutes. Goes-5 senses a (presumably the same) magnetic disturbance about 14 minutes later. Their separation gives a propagation speed of about 1.6×10^{6}cm/sec. A second disturbance, with the same speed, is seen in the GOES-6 magnetometer at 1000 UT and by GOES-5 at 1014 UT. This second impulse does not appear to have an accompanying injection signature at the midnight meridian spacecraft (LA-129), or the morning sector spacecraft (LA-019).

The omnidirectional electron energy flux at the morning sector spacecraft (LA-LA-019) undergoes an increase from 14×10^{-2} ergs/cm$^{2}\cdot$sec at 830 UT (before initiation) to 34×10^{-2} ergs/cm$^{2}\cdot$sec by 900 UT, and then decreases gradually back to the pre-substorm level. The decrease is not completely monotonic; about 1030 UT a slight increase in energy flux is evident, but as discussed below, this probably arises from local acceleration. The later injections (1007 and 1040 UT) at s/c LA-129 mentioned above show up in the electron moments as a significant increase, but this is not reflected at all at the other spacecraft. Note that Figure 3.4 indicates a maximum magnetic bay is reached at about 1030 UT. The afternoon spacecraft (LA-LA-037) shows a trend in the energy flux which does not correspond to either the midnight behavior of the energy flux or the morning sector energy flux. This is apparent from 1000 to 1030 UT, when the energy flux decreases to values well below the pre-initiation value ($2.9{\times}10^{-2}$ ergs/cm^2·sec). During this time interval of decreasing afternoon energy flux, both the midnight region and the morning sector are maintaining much steadier values.

Figure 3.11 shows a succession of electron differential energy spectra taken every half hour throughout the 830-1130 UT interval, on log-log plotting scales. The top panels are from s/c LA-019 while the bottom are from s/c LA-037. The morning sector electrons have a hard spectrum before onset at 830 UT, and obtained the softest energy spectrum by 900 UT. The spectra indicate various changes and different amounts of structure. For instance, the energy turn-over at about 90 keV is probably due to the arrival of the higher energy particles first from the source region. The differences between the morning sector and the afternoon sector spectra seem to be primarily in the lower energy (<300 keV) electrons. The morning sector electrons often have a relatively smooth power law spectrum during the 830 to 1130 UT interval, while the afternoon always has considerable structure. In neither location was there ever any indication of an exponential spectrum, neither single or two component. The afternoon spectra are too structered to model with either power law or exponential. Table 3.3 summarizes the electron characteristics at all three of the Los Alamos-DOD spacecraft. Since the electron spectra from s/c LA-037 could not be well parameterized by a single number such as the spectral-index or e-folding energy, these were not given for this spacecraft in Table 3.3.

Table 3.3 Electron moments summary.

	Time (UT)						
	830	900	930	1000	1030	1100	1130
s/c LA-129							
Flux ($10^5 e^-/cm^2 \cdot sec$)	1.1	15	15	15	24	26	8.0
Energy Density ($10^{-11} ergs/cm^3$)	2.0	15	15	15	21	23	8.2
Energy Flux ($10^{-2} ergs/cm^2 \cdot sec$)	1.9	23	22	23	35	39	12
Spectral Index	-	2.8†	2.8†	-	3.7†	3.5†	2.4
s/c LA-019							
Flux ($10^5 e^-/cm^2 \cdot sec$)	8.9	19	18	17	19	18	15
Energy Density ($10^{-11} ergs/cm^3$)	9.3	34	27	24	28	23	20
Energy Flux ($10^{-2} ergs/cm^2 \cdot sec$)	14	34	30	29	32	29	25
Spectral Index	2.9	4.1	3.7	3.3	3.2	3.3	3.3
s/c LA-037							
Flux ($10^5 e^-/cm^2 \cdot sec$)	1.8	1.8	2.4	1.6	0.9	1.8	2.8
Energy Density ($10^{-11} ergs/cm^3$)	3.5	4.0	5.7	3.8	2.4	3.7	4.9
Energy Flux ($10^{-2} ergs/cm^2 \cdot sec$)	3.1	3.2	4.6	2.9	1.6	3.2	4.8
Spectral Index	-	-	-	-	-	-	-

\- Highly structured spectrum (non-thermal, non-power law), see text.
† Two component power law spectrum, low energy component only.

The time variation in the differential electron fluxes at the three spacecraft exhibit energy dependence in their behavior. The dawn sector and early afternoon sector spacecraft (s/c LA-019 and s/c LA-037) both show energy dispersion for the 830 UT onset that would be expected for gradient and curvature drifts. This is indicated in Figures 3.6 and 3.7. There are additional energy dependent features that are not consistent with drifts from a nightside source, however. Several distinct electron flux enhancements in energy channels 30-900 keV during the time interval 1015 UT to 1040 UT at s/c LA-019 show a distinct lack of energy dispersion. The early afternoon spacecraft (s/c LA-037) senses the passage of flux enhancements similarly structured to those at s/c LA-019 during the time interval 1015 to 1040 UT, (a few minutes after the occurrence in the morning sector) and with energy dispersion of about 4 minutes for the 65-95 keV range. This dispersion time is consistent with the particles originating in the morning sector, at the time the dispersionless enhancements are seen at s/c LA-019. The high energy electron fluxes indicate the presence of relativistic electrons at both the nightside and the dayside, yet the appearance of these particles on the dayside is delayed considerably longer than would be expected for electrons drifting along a constant L shell, or for drifts across many L shells.

Morning Sector Auroral Zone Observations

The UW and SRI balloons were located almost midway between these two satellites in local time, at an L value of 5.4 (as determined by Mead-Fairfield disturbed magnetic field model). Figure 3.12 shows a four hour plot of X-ray data from both the SRI and the UW experiments. The SRI balloon was located slightly west (about 80 km, see Figure 3.2) of the UW balloon, and apart from variations in some of the details, detects a similar time profile of X-ray fluxes. Both detected the initial X-ray onset at about 905 UT and both reached maximum intensity by 910 UT, which is well correlated with the passage of electrons at the morning sector spacecraft, LA-019. The X-ray fluxes have decreased to near a pre-onset level by 940 UT, yet, as discussed above, the morning sector electron moments and spectra have remained close to the values attained following the onset.

The second bremsstrahlung X-ray onset at the balloons, commencing at about 1005 UT, does not appear to be accompanied by the distinctive electron flux enhancement seen at s/c LA-019 or s/c LA-037 as does the 905 UT onset. Nor were there marked changes in the energy-spectral characteristics for the electrons drifting towards the precipitation region. Indeed, the characteristics of the drifting electrons appear to be returning to pre-onset values (see Table 3.3 and Figure 3.6) in the time interval preceding and during the X-ray onset at 1005 UT rather than indicating a passage of new electrons from the nightside to the precipitation region. The temporal behavior of the X-ray fluxes during the interval 1030 to 1050 UT show similarity to the behavior of the electron fluxes at both the morning and afternoon sector spacecraft.

In order to further understand the smaller scale features for this event, X-ray, electric field, and riometer data will be examined. (See Figure 3.2 for a map of the region.) Figure 3.13 shows the superposed time profiles for the X-ray fluxes detected at the two different balloons for the one hour period 930 to 1030 UT. Although the X-ray fluxes seen at the SRI balloon for the 1005 UT event saturate the spectrometer, there is good indication of simultaneous onset of the 1005 UT event. Figure 3.14 is a four-hour composite of both X-ray data sets, riometer data from Sodankyla (L = 5.4), and Kevo (L = 6.1) and the electric field data from the SRI balloon. The time of maximum intensity at the riometer stations is seen to be later at higher latitudes, progressing from 950 UT at L = 5.1 to 1000 UT at L = 6.2. The second onset of X-ray fluxes does not begin until 1000 UT, and the maximum at the UW balloon is reached at about 1015 UT. There is structure visible in both riometer time profiles around 1040 that is similar to that seen in the UW X-ray fluxes and the electron fluxes.

The SRI electric field data undergoes both amplitude and direction changes during the 900 to 1100 interval. The bottom panel of Figure 3.14 shows the north-south and east-west components, as well as the total horizontal field strength. These changes are not exactly correlated with the X-ray onsets, but show some similarities. The local acceleration event at 1040 UT is also apparent in the time profile for the north-south component, with the X-ray flux increases correlated with the field becoming more northward.

The University of Washington's X-ray imager allows small scale spatial features to be resolved. Images during most of the 1000 UT event are fairly featureless, but at the onset of the event there appears to be a southward progression of the X-ray activity. This is shown in in the image (upper panel) in Figures 3.15. This was obtained as the X-ray fluxes at the detector were undergoing the sharp rise at 1005 UT indicated in Figure 3.13. The image view is looking down on the auroral zone, with north at the top of the image. The 1005 UT image show a generally enhanced emission over the entire imaged area, but the northern region has higher fluxes than the southern. Finally, the last image, at 1010 UT, shows the entire image plane uniformly filled, without north-south gradients. The middle panel of Figure 3.15 is a contour plot of the 1005 UT image in the top panel. This will help see the south to north gradient in the precipitation. The bottom panel is an intensity profile obtained by taking a cut through this image. The error bars represent spatial resolution and the variance associated with the intensity of each pixel.

The two X-ray events, at 900 and 1000 UT, show similar behavior in their energy spectral characteristics. Note that the time the spectra were sampled was several minutes after the onset for both events. This is due to the imager operating configuration; energy spectra are more accurately obtained during a 'raw' data mode rather than an 'imaging' mode of operation. Figure 3.16 shows the energy spectra for these two events, along with a spectrum from an earlier time of very low X-ray activity. The e-folding energies for the active periods are about 26 keV (5 keV), while the quite time spectrum is harder, having an e-folding energy of about 44 keV (5 keV).

3.3. Discussion

The above measurements and observations represent several different processes occurring globally and locally. The major points we wish to draw attention to are the following: (1) Plasma injected near midnight has a strong energy dependence in reaching the dayside. Narrow energy-band injections, even if high in energy-flux, will not necessarily contribute strongly to dayside precipitation. (2) The variations in the electron moments at geosynchronous altitudes in the path of drifting electrons is not a good predictor of the intensity or time variations in energetic electron precipitation in the morning sector. (3) Pre- and post-onset magnetospheric electron fluxes in the midnight, morning, and afternoon sectors indicate a strong loss region in the morning sector. If it is assumed that drifting electrons are a major source of afternoon fluxes, and these same particles have drifted through the morning sector en route to the afternoon sector, then the morning sector acts as a 'non-linear' filter to the drifting plasma, i.e., the flux lost is not linearly proportional to the flux levels of the particles drifting into the loss region. This, in conjunction with the second point, suggests that precipitation losses are not a simple result of wave-particle induced pitch angle diffusion driven by the drifting electrons. (4) There are distinct indications of local acceleration in the morning sector, which may also suggest other local mechanisms to be involved in causing the observed particle losses. (5) The local morphology of the plasma flows and precipitation in the morning sector suggest a source region for the precipitating electrons that is moving radially outward and westward, at least over some finite length scale.

Energy and Drift Features

The comparison of the low energy (30-300 keV) electron fluxes between the three geosynchronous satellites indicates variations that are not simply related, although there are some general trends that can be stated. The strong temporal variations near the injection region are not evident in either of the other two spacecraft. These variations are strongest in the lower energy channels. The characteristics of the morning sector energy spectra and the lack of appearance on the dayside of the the 920, 1007, and 1040 UT nightside injections, all of which were narrow band, suggests that the lower energy particles are preferentially lost in transit to the dayside. This suggests that dayside precipitation is dominated by the higher energy component of nightside injected electrons.

The presence of dispersionless flux enhancements in the electron fluxes from 1015 to 1030 indicate that the nightside is not the only region of energization. The multiple injections at 1030 UT at s/c LA-019 gives a signature that is also apparent in the balloon X-rays and the afternoon electron fluxes. However, the presence of dispersion in the afternoon, and the lack of signature at s/c LA-129 near midnight indicates the acceleration was not global, such as magnetospheric compression, but was local to the morning sector.

Morning Sector Dynamics

The presence of drift dispersion features in the afternoon electron fluxes indicates that the source of electrons is elsewhere. The onset at 900 UT in the afternoon has dispersion and time-lag relative to both the morning and midnight sector observations that are consistent with the source being the 840 UT injection near local midnight. The dispersion features at 1040 UT in the afternoon sector, with the ground observations, are consistent with a multiple injection occurring in the morning sector. These coupled observations in the morning and afternoon sectors give strong support for the source of afternoon electrons being drifts from the nightside through the morning sector. This is expected when gradient and curvature drifts dominate convection. This identification allows us to probe the late morning sector by watching the 'input' electron fluxes at s/c LA-019, the 'output' electron fluxes at s/c LA-037, and the losses as deduced by the X-ray intensities and riometer absorptions. This idea is shown schematically in Figure 3.18. This probing technique will be used in the discussion that follows to investigate the loss mechanism in the morning sector..

The initial X-ray burst at 900 UT is well correlated with the passage of the first injected electrons to the dayside. This injection results in a signature in all three spacecraft and the balloons X-ray detectors. The second X-ray onset is not associated with a signature in any of the dayside spacecraft, but could possibly be related to the injection at 920 UT at s/c LA-129. This would require an injection to a lower L value. The lack of signature for the 1005 X-ray onset is even more dramatic in the afternoon electron fluxes, which are undergoing a decrease rather than maintaining a fairly constant level as the morning fluxes do. Using the notion of input, output, and losses as described above, the electron fluxes (and other moments) into the region are steady or slightly decreasing (aside from the local injections), the output is strongly decreasing in all the electron moments, and the losses are seen to be stronger than when the energy flux input was much higher and the spectrum was softer, as during the 900 UT onset.

Relationship Between Midnight Auroral Zone and Morning Sector

The magnetic bay observed in the College magnetometer lasts from roughly 900 UT until 1100 UT, and indicates nightside auroral energy deposition during this entire interval, with the maximum occurring at about 1030 UT. However, as stated above, the particle signatures at dayside geosynchronous orbit reflect only the 840 UT injection. Is there a contradiction between the extended bay on the nightside, but only a single identified dayside electron enhancement that has dispersion characteristics consistent with a nightside source? We do no think so since the multiple midnight injections are more narrow band in energy, i.e., do not extend to the higher energy (>65 keV) electrons. As noted above, these lower energy electrons do not produce a strong signature in the morning sector at geosynchronous altitude. The picture we propose is that the lower energy electrons are much more important in the midnight sector aurora and are lost before entering quasi-trapped drift orbits. This picture is also consistent with the extended magnetic bay since currents are dominated by the lower energy, higher number-density particles, so the auroral electrojet will be driven by low energy particles which are not necessarily well correlated with the high energy component. Therefore, nightside auroral magnetometers are not necessarily good indicators of energy transport to the dayside, at least not for the higher energy component that appears to be the source for the 1010 UT precipitation.

The possibility that the drift paths for the 920, 1007, and 1020 UT injections near midnight are inside of geosynchronous altitude in the morning sector still needs to be addressed. This would imply a narrow injection region closer to Earth than the one at 840 UT. *McIlwain* [1985] and *Newell and Meng* [1987] argue that the radial extent of injection will not account for energetic particle precipitation (>10 keV) at sub-auroral latitudes in the morning sector, and believe these events are caused by electron injected near midnight that subsequently convect along constant geomagnetic latitude. Note that this restriction to the higher energy particles is consistent with our assertion that the nightside aurora may be dominated by the lower energy particles, while the dayside precipitation is dominated by the higher energy particles. This morning sector precipitation has been called the mantel aurora [*Sandford*, 1968; *Meng and Akasofu*, 1982]. [*Meng and Akasofu*, 1983] also attribute the mantel aurora to drifting of electrons from a nightside injection. These models, and the above observations, only address the problem of the source of the precipitating particles. The mechanism that allows these to precipitate will now be discussed.

Drift-Induced Precipitation Models

The drift-precipitation model of *Jentsch* [1976] and *Kangas et al.* [1975] assumes that dayside precipitation is the result of a nightside particle injection, which drifts to the dayside by convection, curvature, and gradient drift forces. The latter two are energy and pitch angle dependent and thus result in anisotropic velocity distributions. If the anisotropy is large enough, the whistler mode wave will be unstable and grow, giving rise to scattering of the resonant particles into the loss cone. This would be observed as particle precipitation.

To analyze the current observations in the context of this model requires a more detailed discussion of the relevant theories. Furthermore, the observations we present can only make inferences about the presence of waves based upon the results of previous works and theories. These theories predict behavior that should be evident in the data we have examined. The formulation proposed by *Kennel* [1969] is a generalization of an earlier theory [*Kennel and Petschek*, 1966] to describe the diffusion of particles in pitch angle, and possible energy, by wave turbulence. The quasi-linear expression for diffusion is given as [*Kennel and Engelmann*, 1966];

$$\frac{\partial f}{\partial t} = \lim_{V \to \infty} \int \frac{d^3k}{(2\pi)^3 V} \sum_n \left[G_k + \frac{\omega_k - k_z v_z}{\omega_k v_{perp}} \right]^* \times \frac{\delta((\omega_k \pm n\Omega_\pm)/k_z - v_z)}{|v_z - \partial\omega_k/\partial k_z|} |\Theta^\pm_{n,k}|^2 \, G_k f(v)^\pm \tag{3.1}$$

where the z-subscripted quantities are parallel to **B**, the ± superscripts refer to ions or electrons, G_k is a differential operator on the velocity distribution function, $f(v)$, and $\Theta^\pm_{n,k}$ contains information on the coupling of the waves to the particles. The function

$\Theta^{\pm}_{n,k}$ allows any wave mode to be considered, by expressing the coupling through the wave electric field as two circular (right and left hand) and one parallel polarization component. The delta function picks out only the resonant waves, and the integration is over all wave numbers. A Fokker-Planck formulation differs from (3.1) by leaving the diffusion and friction coefficients unspecified. Once the Fokker-Planck coefficients are calculated in terms of the physics of the medium these two theories yield the same result.

For the special case of the whistler mode with $\omega \ll \Omega^-$, nearly parallel propagation, and a smooth wave *k*-spectrum, Eqn (3.1) reduces to a more familiar diffusion equation for the pitch angle [*Kennel*, 1969];

$$\frac{\partial f}{\partial t} = \frac{1}{\alpha}\frac{\partial}{\partial \alpha}\left[D_\alpha \alpha \frac{\partial f}{\partial \alpha}\right] \tag{3.2}$$

where a small angle approximation has been used. The pitch angle diffusion coefficient D_α is given approximately by

$$D_\alpha = \frac{\Omega^- \beta_\omega}{\cos\alpha} \tag{3.3}$$

where β_ω is the ratio of wave magnetic energy to total magnetic energy. Other wave modes may not result in a similarly expressed diffusion equation or coefficient using the formulation of Eqn. (3.1).

This expression for whistler mode diffusion allows two limits to be examined. For the weak limit, the time scale for a particle to random walk into the loss cone is much longer than the time for the particle to leave the interaction region, so most particles which enter the loss cone will not have time to exit before being lost to the atmosphere. In this case the precipitation rate is proportional to D_α. Strong diffusion is the opposite; a particle can diffuse in and out of the loss cone many times without being lost and the loss rate is nearly independent of D_α since the loss cone is nearly full. In either case the diffusion coefficient is still proportional to the wave energy density. Since wave amplitudes are not readily calculable, the common approach at this point is to determine the linear theory growth rate, which is an easily calculated quantity but of limited value. The "marginal stability" concept in the weak diffusion limit [*Kennel and Petschek,* 1966] is one successful application of growth rate analysis in understanding magnetospheric particle flux limiting. A sufficiently fast growth rate is probably a necessary requirement, but not a sufficient one, to achieve stronger diffusion.

For plasma with a cold density much greater than the hot density, the whistler mode dispersion relation is independent of either the hot or the cold electron properties, while the growth rate is determined by the hot electrons. Therefore, changes in the cold electron characteristics should not affect either the dispersion or the growth rate and any pitch angle diffusion caused by whistlers will not be influenced by electrons for which we have no measurements. However, there is no *a priori* reason why the wave mode must be a whistler. The only requirement is the resonance condition,

$$V_R = \frac{(\omega_k - n\Omega)}{k_z} \tag{3.4}$$

where V_R is the velocity of the resonant electron and n is any integer (positive, negative, or zero). Using (3.3), and the whistler dispersion relation, it is found that the electromagnetic wave frequencies (several kHz) observed in the magnetosphere would resonate with electrons of energies up to 100 keV.

Assuming that the electrons drifting from the nightside to the precipitation region after about 930 UT are not confined to L shells inward from the spacecraft and that the precipitation mechanism is a velocity space diffusion process, what can be said about the pitch angle diffusion given the observations? The precipitation rate is not a function of the omnidirectional electron moments or the energy spectra of the electrons entering the region. This follows directly from the geosynchronous electron data near the morning sector. The connection between precipitation rate and the diffusion coefficient depends upon the diffusion regime. For the interval 1000 to 1100 UT, the minimal change in 'input' characteristics but significant change in the 'output' and 'loss' characteristics of the precipitation region suggest that the loss mechanism is being driven by something other than the input drifting electron fluxes. Since the input fluxes are not driving the system, the precipitation rate must be dominated by either the lower energy particles, which we have no information about, or the dominate influence are local effects. The *Kennel and Petschek* [1966] theory predicts that the resonant particles, i.e., the ones being precipitated, determine the diffusion and the loss rate. The data also indicates that electrons of all energies are being lost in the morning sector indicating a fairly broad-energy band loss process. This follows from the observed prominent drop-out in the fluxes of electrons of all energies drifting into the afternoon sector from the morning sector.

As noted above, the precipitation does not have to be a caused by pitch angle diffusion, a non-diffusion process can be working also. The requirement is to violate the particles adiabatic invariants and disturb their stable bounce orbits. Some examples of non-stochastic, and hence not diffusive, processes are adiabatic decompression and electric field acceleration. In either case, acceleration is relevant only when in the parallel direction, since the loss cone must somehow be populated, which is accomplished by giving the particles a boost in their parallel velocities. Since wave activity is commonly observed in the morning sector, and often with intensities greater than other regions of the magnetosphere, this is a reasonable starting point for a model of precipitation in this region.

Local Morphology

The observations from the riometers and balloons may play a role in the dynamics of the precipitation region. The time lag for the maximum to occur in the riometer stations indicates a northward motion of the precipitation region with a velocity of about 3 km/sec in the northward direction. The delay between onset at the Sodankyla riometer station (at L=5.1) and the maximum in X-ray intensity at the balloons (at L=5.4) is about 15 minutes giving a velocity of about 0.6 km/sec in the westward direction. These translate to about 12 km/sec. radially outward and 3 km/sec. westward on the equator at L=5.4. The shape of the front is not known, so these values must be used with caution. Never-the-less, there is a westward component to the motion, which is opposite to the direction of the electron drifts. The observed northward component to the motion in the riometer data is consistent with the X-ray imager observations of a south-to-north gradient in the X-ray fluxes at the 1005 UT onset.

The electric field data from the SRI balloon may be related to convection flows in the equatorial plane, although the mapping becomes complicated if parallel electric fields are present [*Chiu et al.*, 1981; *Chiu*, 1974]. The electric field is rotating from east to north, which corresponds to radially outward, anti-sunward flow. Although these directions correspond well to the above observations, the timing is not exactly matched between the onset of the X-ray intensities and the convection flow rotation. The electric field can only be related to convective flow, not to other drift motions. In this sense, if the two observations of motion are indeed caused by the same thing, than the precipitation region is not being driven by the drifting electrons from the nightside, since the motions are in the opposite direction to the drifts.

The 1015 UT injection in the morning sector as deduced from the electron fluxes may play a role in the onset of X-rays at the same time. Since there is no time delay between the maxima of the two events, the acceleration region would have to extend from about 800 LT to 1100 LT. If the magnetic impulse at GOES-5 at the same time is related, than the longitudinal extent would be even larger (by three hours). Note however that the magnetic field disturbance appears to be propagating from the nightside with a speed much less than could account for the 1015 UT events. The morning sector injections are also not completely correlated with the electric field variations.

Other Precipitation Models

Purely temporal precipitation models have been examined for morning sector events. *West and Parks* [1984] made correlated measurements of ELF wave activity and bremsstrahlung X-rays near local noon. An analysis by *West and Parks* in the context of wave-particle interaction led them to conclude that the observations were consistent with the *Coroniti and Kennel* [1970] model for self-excited whistler wave turbulence modulated by micropulsations. The work of *West and Parks* made advances in relating the loss mechanism to whistler waves, but could not relate this to possible sources or what the driving mechanism for precipitation in this sector may be.

A precipitation mechanism will be speculated on as follows: the initial X-ray event at 900 UT is caused by the first injection of particles on the nightside at 840 UT which have drifted to the dayside. This precipitation is due to the drift induced enhanced anisotropy as proposed by *Kremser et al.* [1974] and *Jentsch*, [1976], resulting in pitch angle diffusion in the manner of *Kennel and Petschek* [1966]. This process is largely driven by the lower energy component (<60 keV) of the drifting electrons as determined by the soft spectrum at the beginning of the event. As the spectrum becomes harder the precipitation reduces, until about 950 it has returned to near background levels. This is reflected in the abatement of the bremsstrahlung X-rays at this time.

In this scenario, the second event is also due to wave-particle induced pitch angle scattering, but the waves are no longer being driven by the drifting particles. A possibility suggested by the detected motions at the equator is an interaction at the plasmapause, which is expanding outward, or possibly a detached piece of the plasmasphere. In either case the scattering waves would be drift waves, which are always unstable and are driven by the free energy in density gradients [*Melrose*, 1986; *Krall* *and Trivelpiece*, 1973]. This has been proposed by *D'Angelo* [1969] as a modulation mechanism, but not as a means of pitch angle diffusion. *Hasegawa* [1971] investigated a restricted temperature regime to decouple the drift mode form the Alfven wave and found sufficiently fast growths were easily obtained at the plasma pause for hot electrons. There are other regimes which may lead to different results, but the final analysis must include the resonance condition of (3.4) and an application of (3.1). Until that time the coupling of this mode to the energetic electrons is not known.

The plasma pause would not normally be considered to be out at the region mapping to the highest L value of detected precipitation (L=6.2 at Kevo riometer), but the auroral oval is seen to be far to the north of the balloon positions as indicated in the Viking UV image of Figure 3.19 (The balloon position is marked with a dot and the satellite footprint with a #-sign). This suggests that the plasma pause may not be compressed inward very far during this substorm. *Thorne* [1974] proposed a model for relativistic (>1 MeV) electron precipitation in the morning sector that is caused by ion-cyclotron waves in a higher density plasma blob detached from the plasmasphere. *Chiu, et al.*, [1983] have developed a theory of precipitation modulation in the morning sector involving the mirror instability to spatially modulate electrostatic electron cyclotron induced diffusion. However, as pointed out above, this wave mode cannot substantially affect the high energy (>10 keV) electrons.

3.4. Conclusions

In conclusion, this study has made a detailed analysis of a single substorm with multiple injections at the nightside. The initially injected electrons were found to undergo well ordered drift motions that resulted in both a large azimuthal (i.e., Local Time) change, but also an inward motion to L = 5.4, as observed by bremsstrahlung X-ray data. Further injections on the nightside did not have accompanying signatures on the dayside, and a second very intense X-ray event could not be ascribed to another distinct passage of particles from the nightside. This indicated either a purely temporal effect or a very narrow radial extent, less than 6.6 Re, for the electrons that drift to the dayside and precipitate. The temporal and energy characteristics to the drifting electrons was examined at three local time sectors and was found to exhibit energy dependent changes. The morning sector drifting electron moments were shown to not be a good predictor of precipitation at a later morning sector location. The precipitation was examined in the context of wave-particle theory and it was suggested that the pitch angle diffusion is not driven by the electron fluxes drifting from the nightside, but is influenced by other processes. This was speculated to either be local acceleration or possibly drift waves at the plasma pause.

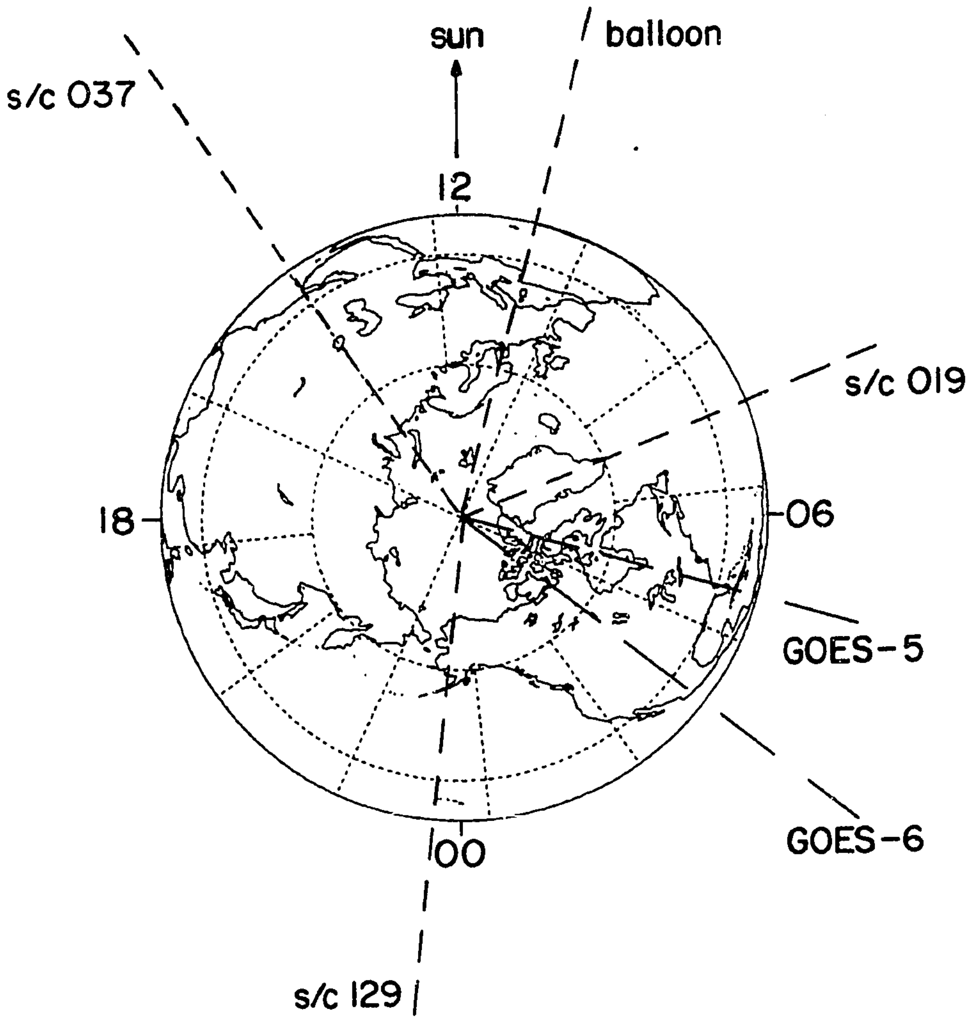

Figure 3.1 Polar-view map of balloon, ground station, and spacecraft positions at 1000 UT, 27 July 1986.

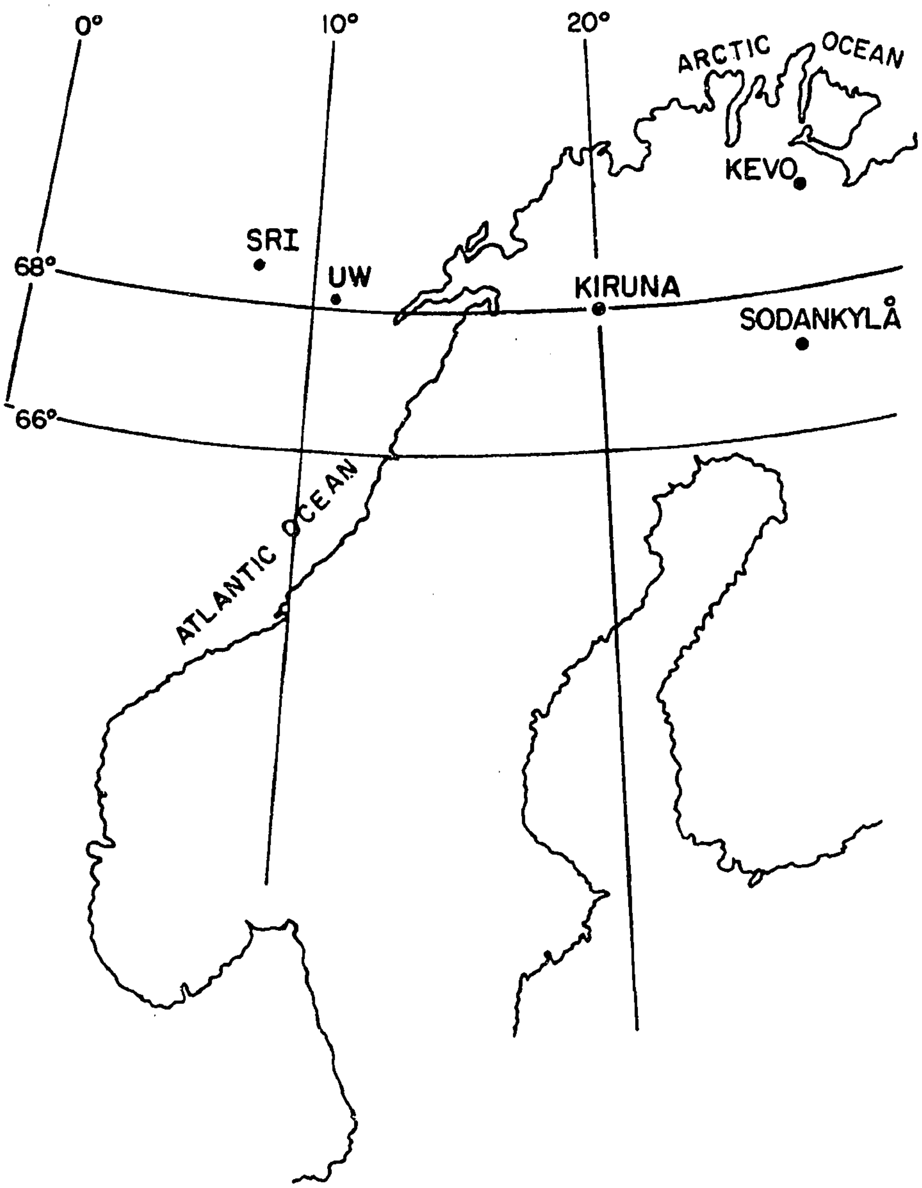

Figure 3.2 Positions of day side riometers and balloons.

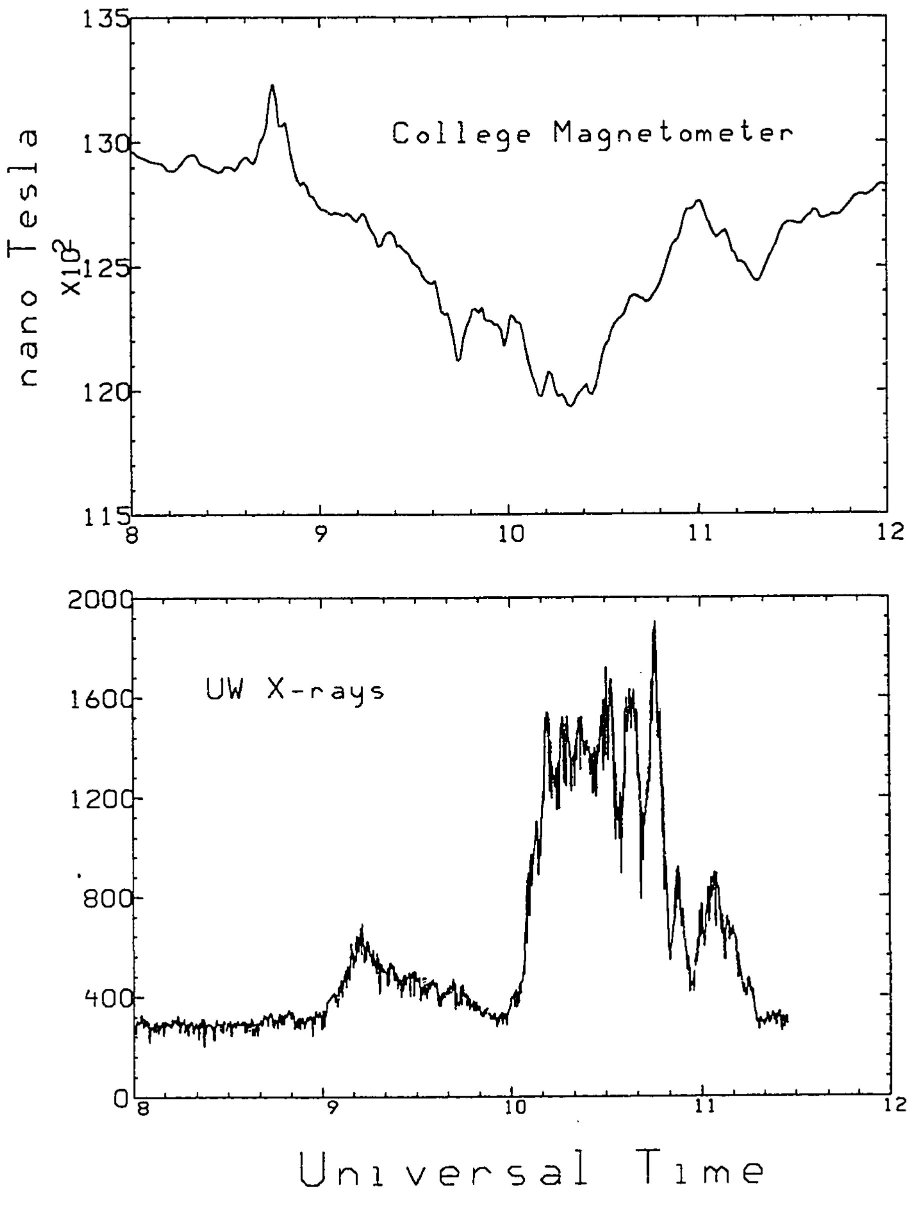

Figure 3.3 Horizontal component of the College, Alaska (0030 LT at 1000 UT) Magnetometer on 27 July and X-ray fluxes at the UW balloon (1100 LT).

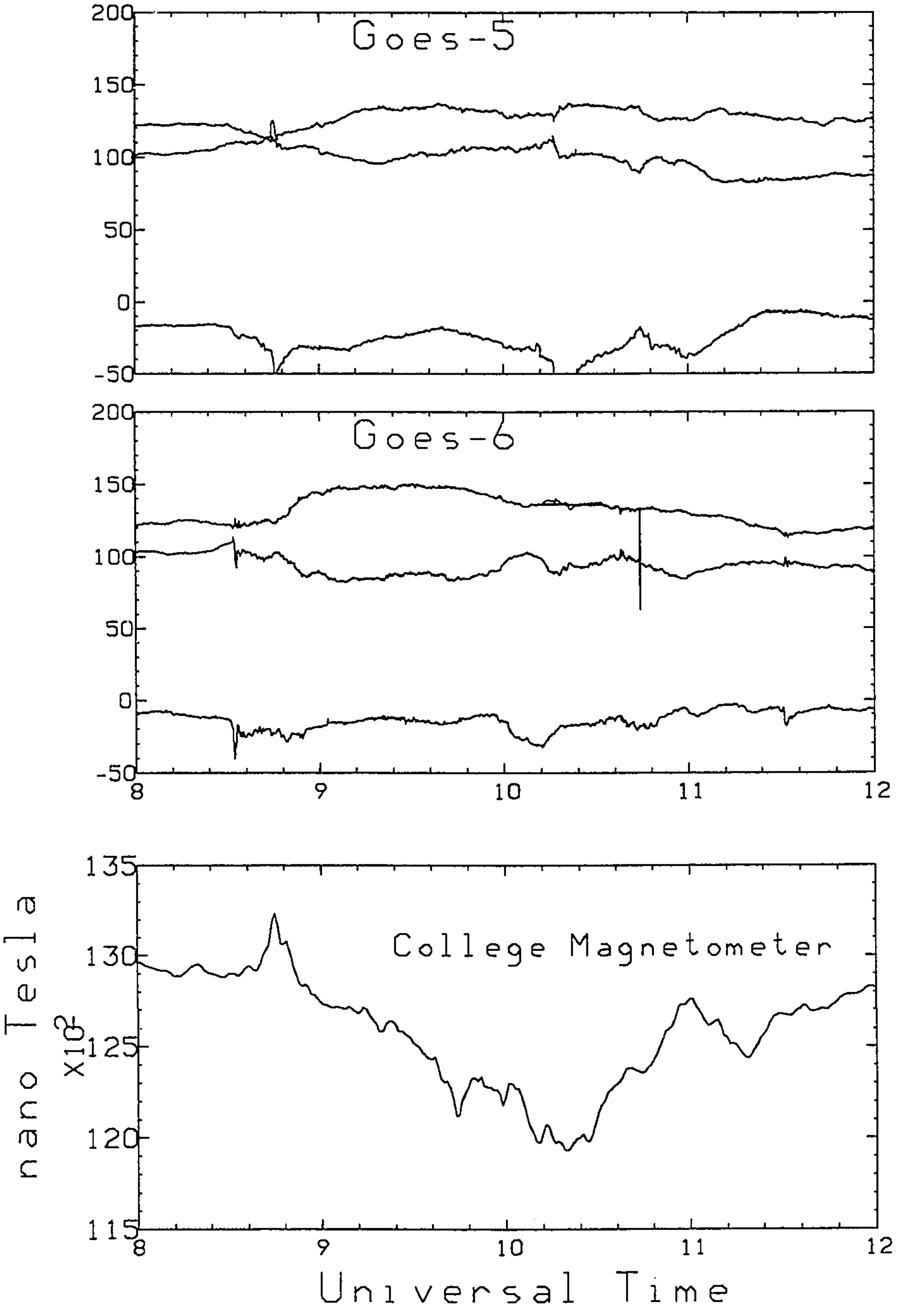

Figure 3.4 College Magnetometer and GOES 5,6 (6.6 Re altitude) magnetometers.

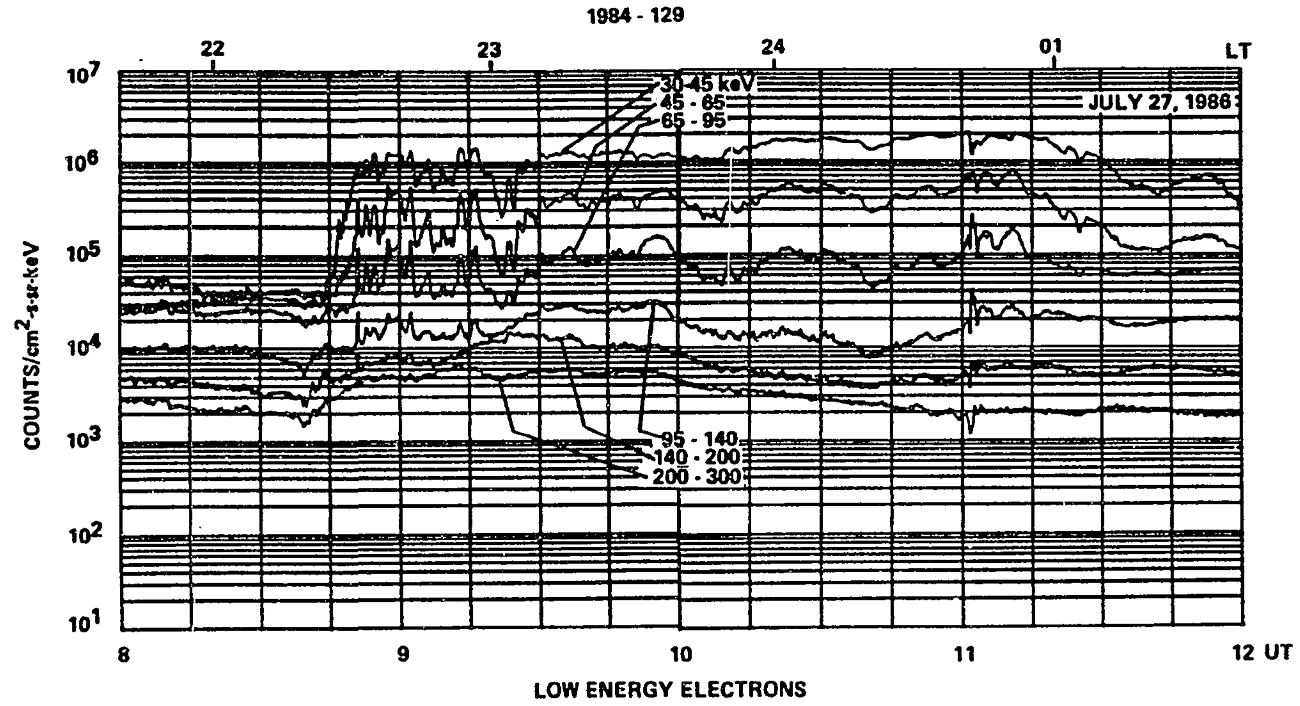

Figure 3.5 Low energy electron fluxes near midnight.

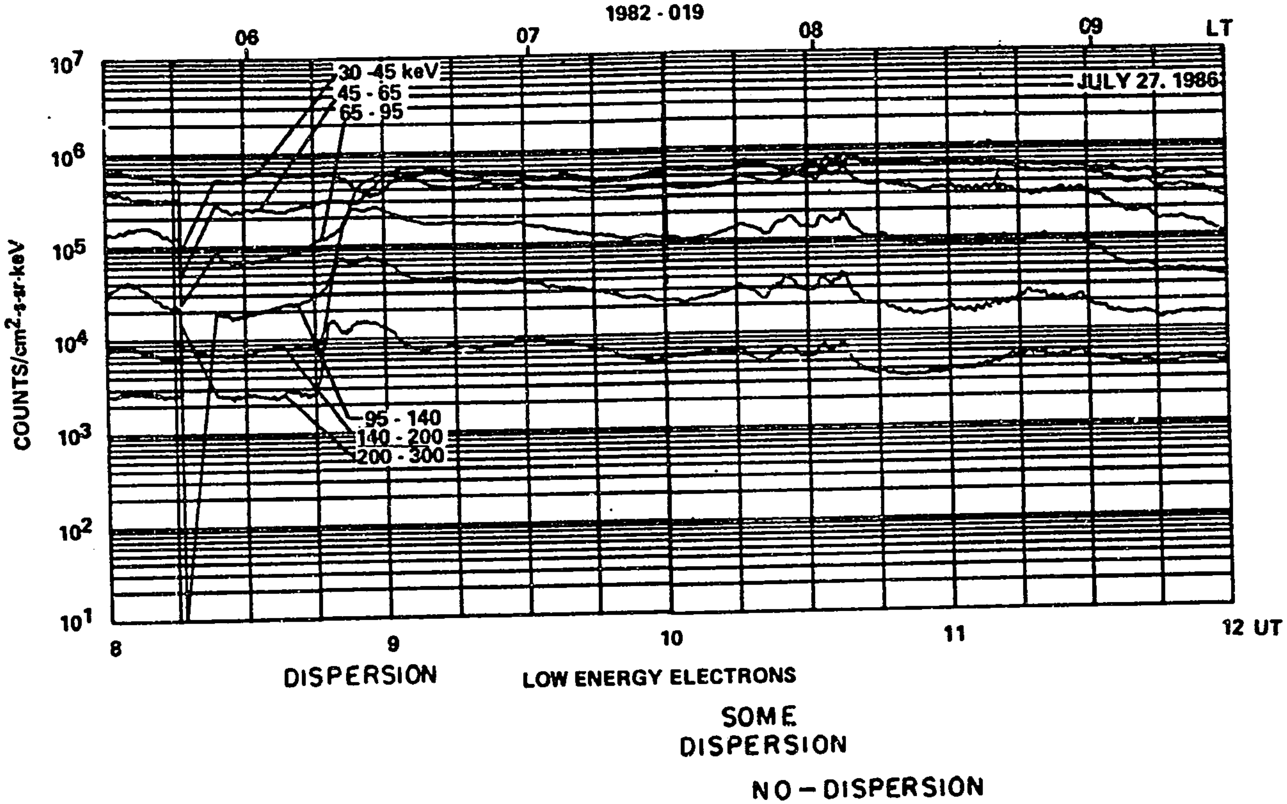

Figure 3.6 Low energy electron fluxes in morning sector.

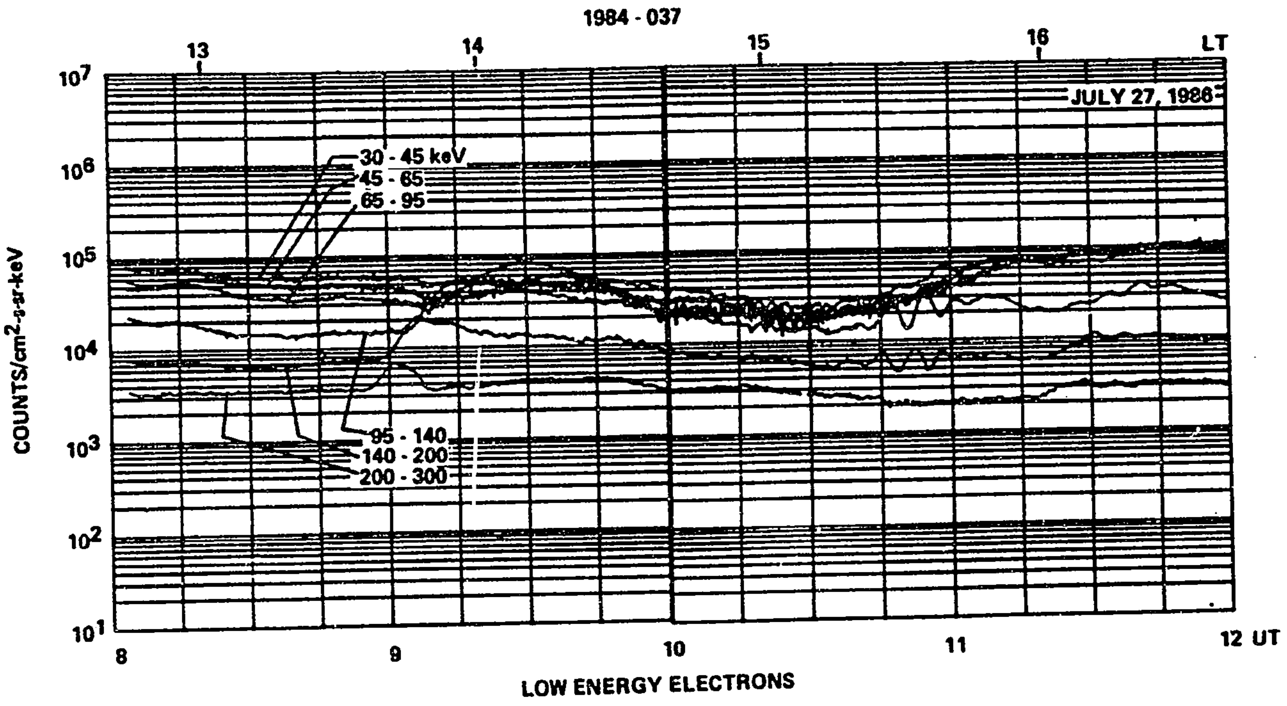

Figure 3.7 Low energy electron fluxes in afternoon sector.

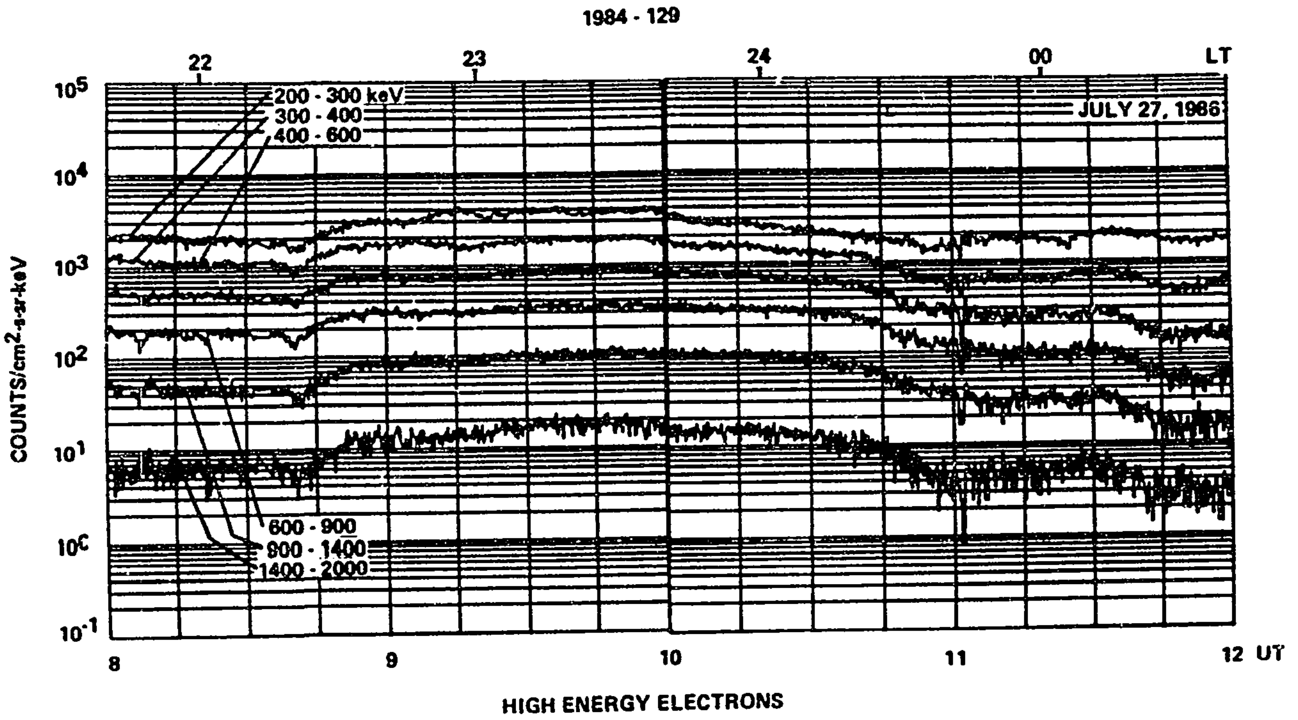

Figure 3.8 High energy electron fluxes near midnight.

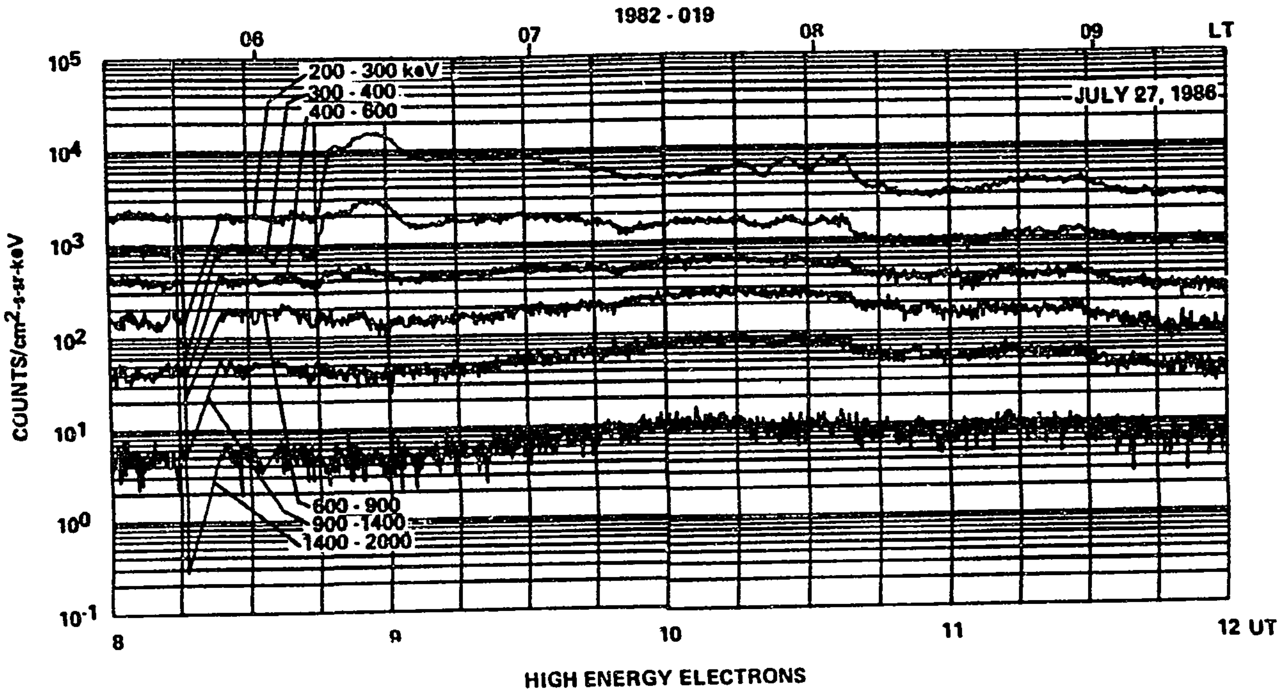

Figure 3.9 High energy electron fluxes in morning sector.

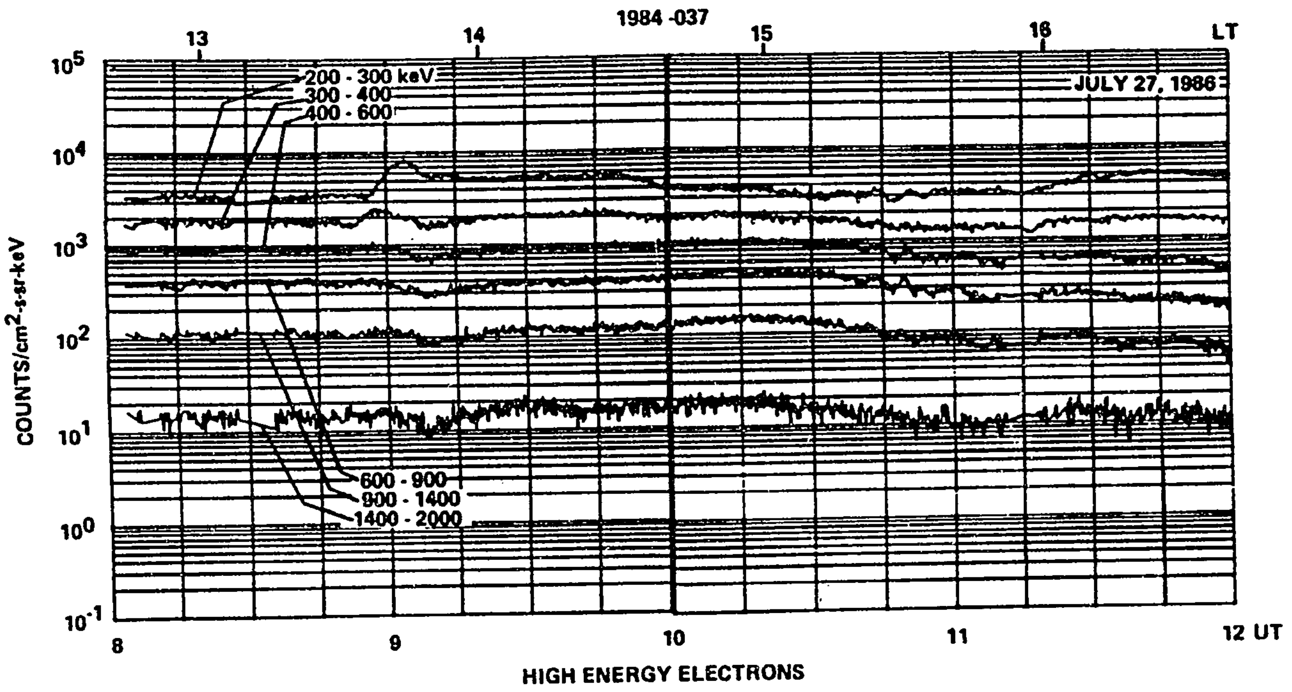

Figure 3.10 High energy electron fluxes in afternoon sector.

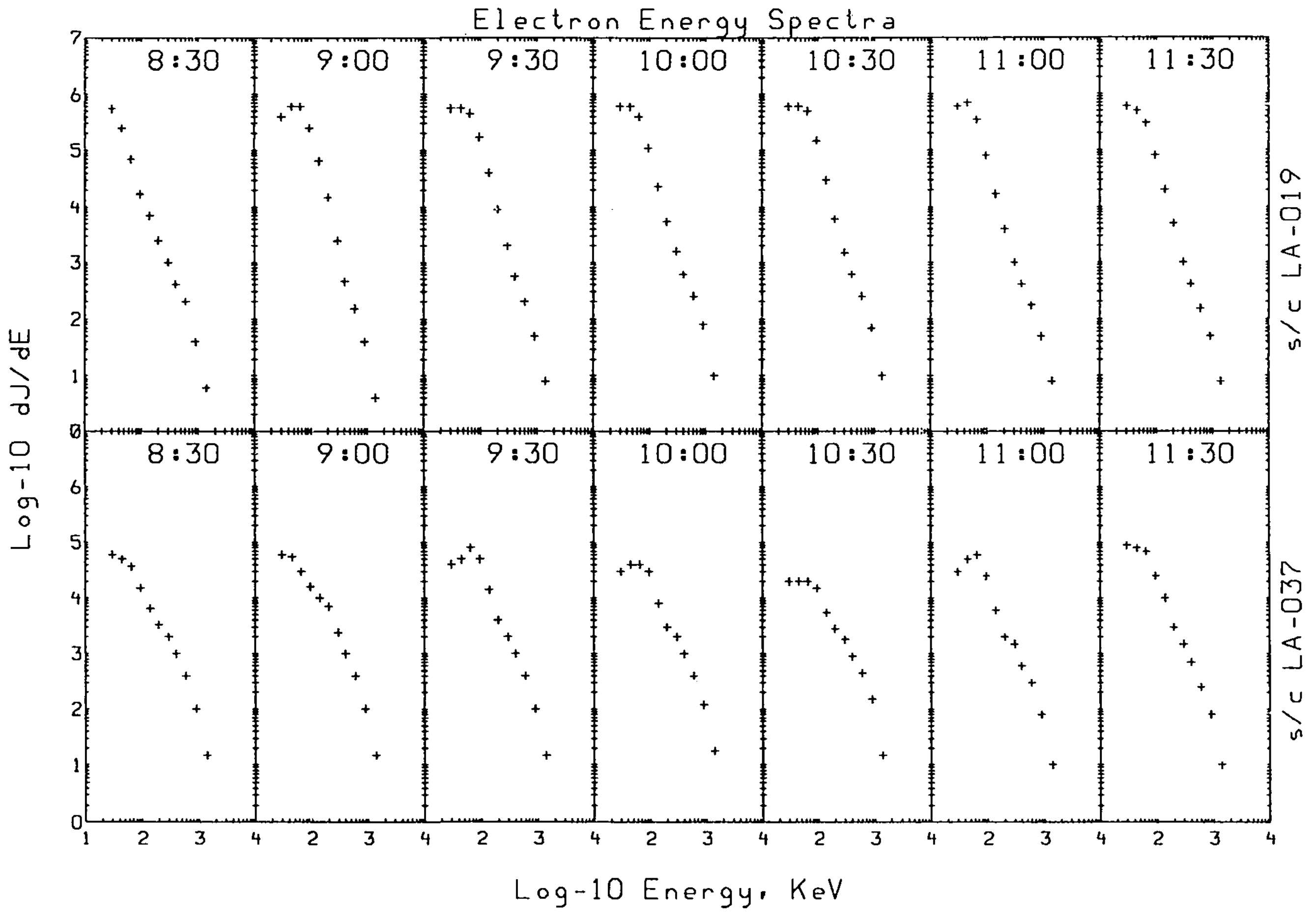

Figure 3.11 Electron energy spectra in morning and afternoon sectors.

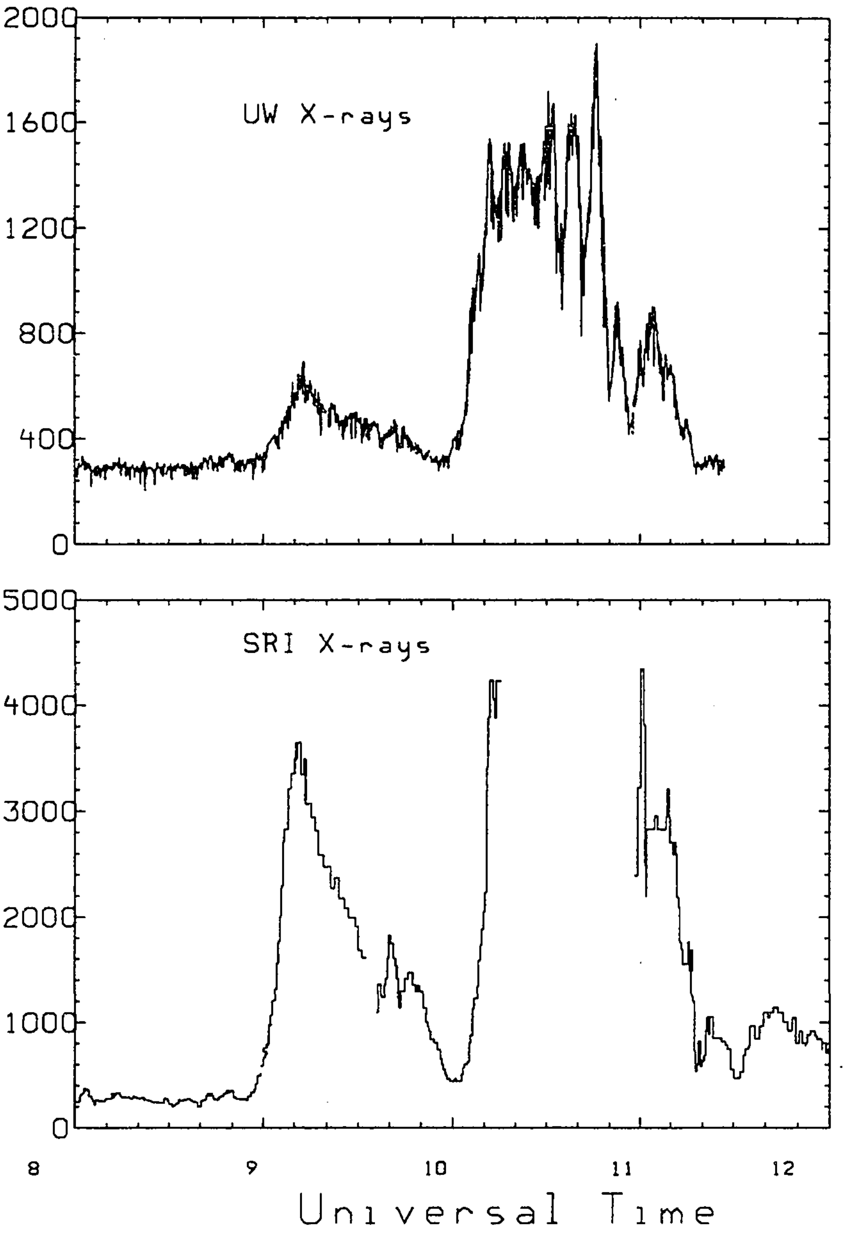

Figure 3.12 Time profile for X-ray counts at UW and SRI balloons.

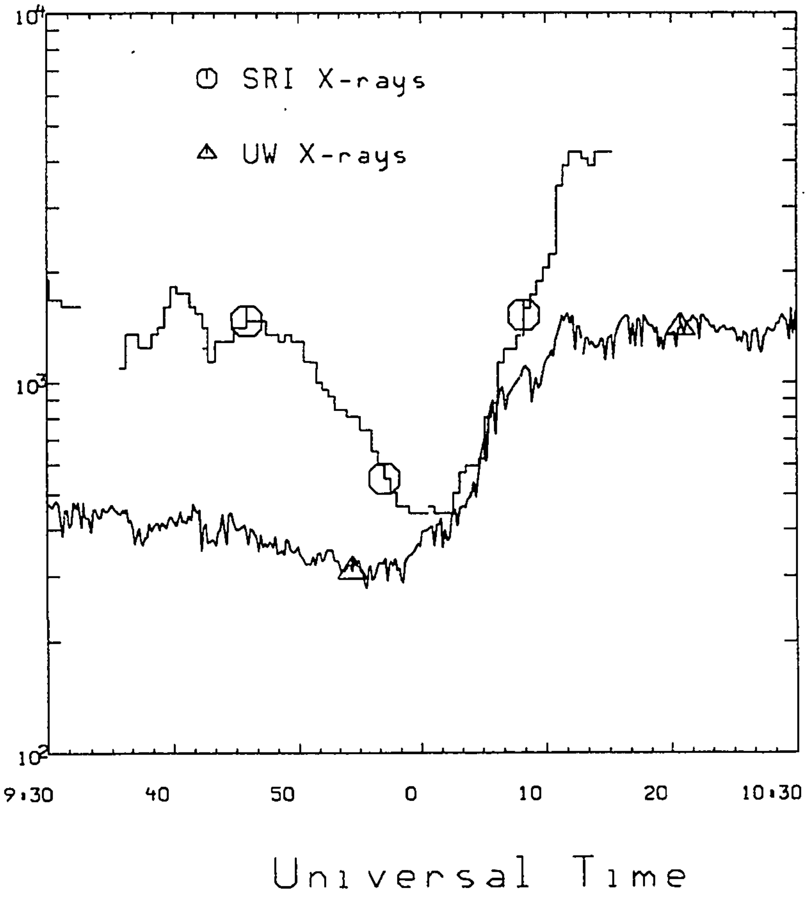

Figure 3.13 One hour super-position of X-ray data at the UW and SRI balloons.

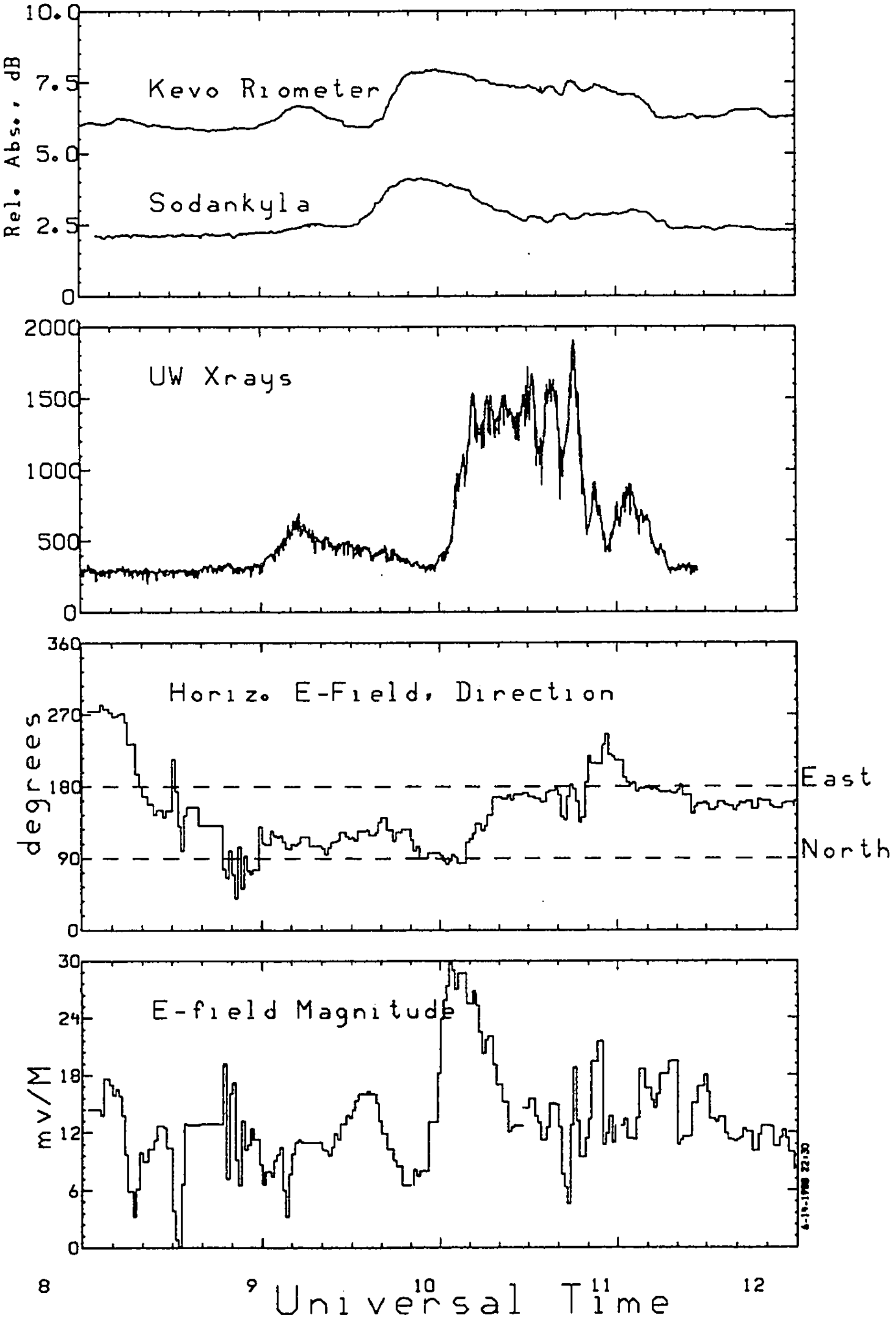

Figure 3.14 X-ray, riometer, and electric field data. The riometers are east of the balloons and on similar L shells, yet attain maximum absorptions about 10 minutes prior to the balloon X-rays. The precipitation propagation is opposite to the electron drifts.

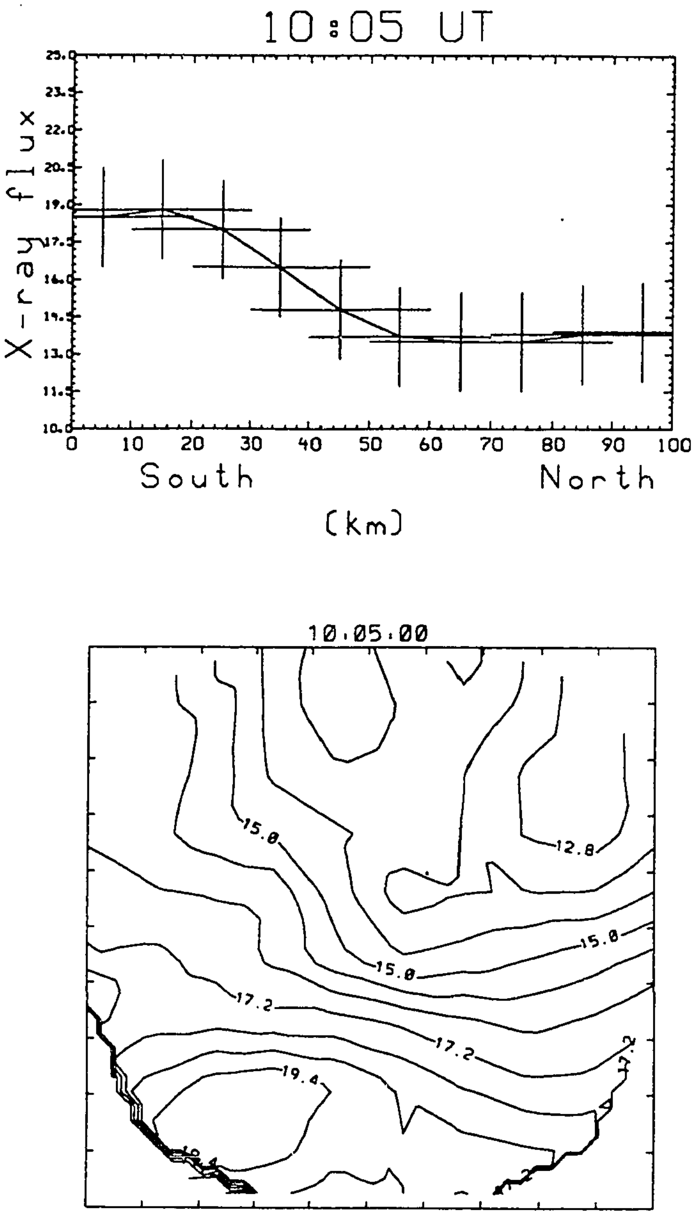

Count Rate: 667. Time: (s) 26

RMS-Noise: 0.73. S/N Ratio: 12.63

Figure 3.15 X-ray image from UW balloon and north-south intensity profile obtained at the 1000 UT onset.

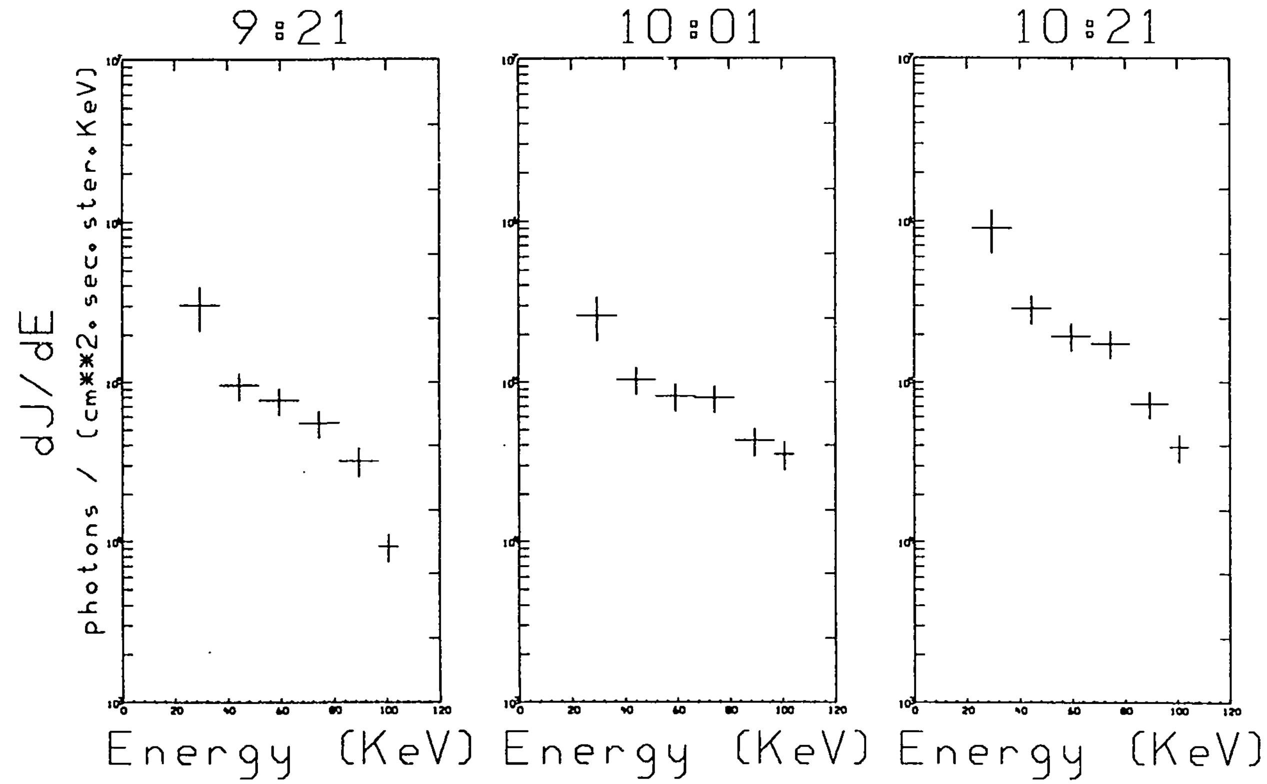

Figure 3.16 X-ray spectra during three phases of the event.

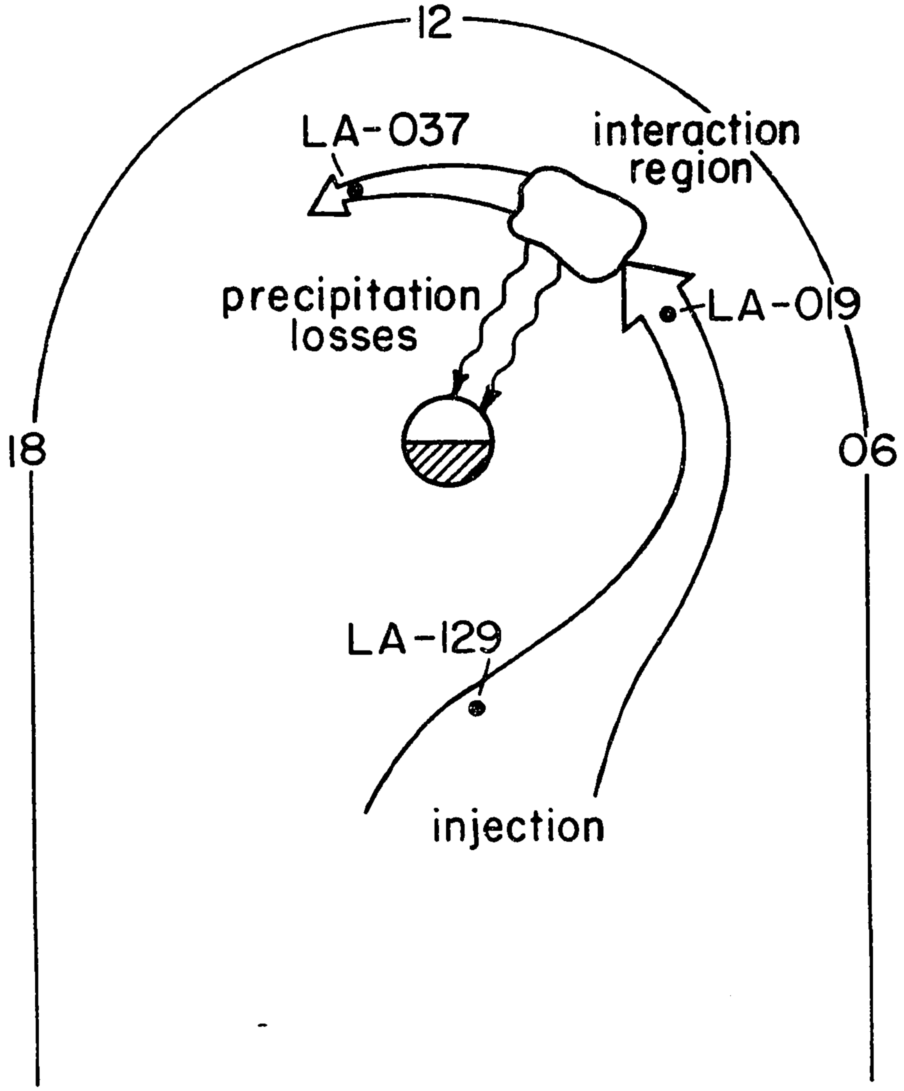

Figure 3.17 Schematic of morningside dynamics. The two geosynchronous spacecraft allow the electrons drifting into and out of the morning sector to be sampled, and the balloons and riometers observe the precipitation losses from the "interaction region".

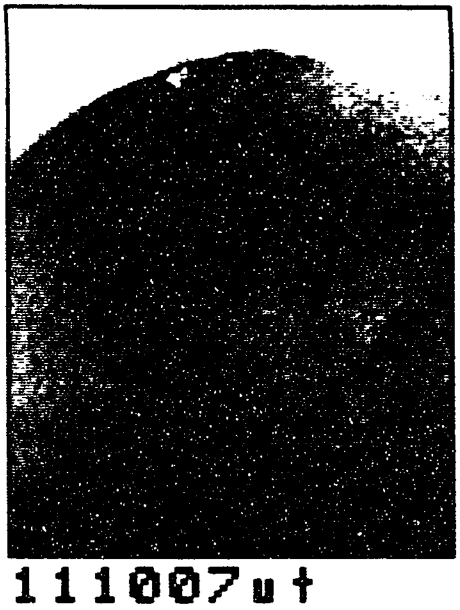

Figure 3.18 Viking satellite UV image of day side auroral oval. The satellite footprint is shown with the #, and the balloon's position is given with the dot. The balloon is well equatorward of the auroral oval.

Chapter 4

Pulsating Aurora

4.1. Introduction

The phenomenon of pulsating aurora has been studied for many years, both experimentally and theoretically. The original use of the term was to denote the early morning, post-breakup occurrence of pulsations in optical emissions from spatially localized regions [*Omholt et al.*, 1969; *Scourfield and Parsons*, 1969]. These emitting regions may pulse with a period of 5-15 seconds, have scale lengths of 1 to 100 km, and have shapes ranging from patches to arcs or arc segments [*Royrik and Davis*, 1977]. Pulsations of the same period in X-rays fluxes in the early morning sector have also been observed [*Barcus et al.*, 1966; *Parks et al.*, 1968], and there has been fairly good correlation between optical emissions at 3914 A wavelength and bremsstrahlung emissions [*Hofmann and Greene*, 1972], but poor correlation with the 5557 A optical line [*Rosenberg et al.*, 1967].

The long time-scale characteristics of pulsation events sometimes show a slower modulation of the count rate, with the faster time-scale variations superposed. The X-ray fluxes may show a steady increase of the long time-scale averaged count-rate, and at other times the pulsation event retains an averaged count-rate which is essentially the same as the pre-event background level [*Parks et al.*, 1968]. The onset in pulsations can also be very abrupt [*McPherron et al.*, 1968] but this could be due to a motion of the source into the field of view of the detector. Slow variations in the long time-scale behavior are also seen, and while the 5-15 second pulsations are widely thought to be temporal modulation, this longer time-scale variation could very well be motion of the source region. The frequency characteristics of the pulsations can be quite mono-chromatic [*Brown and Weir*, 1967], although this is variable also [*McPherron et al.*, 1968].

Past investigations of spatial extent of auroral X-rays during pulsation events have been restricted to large scale determinations with poor resolving ability. *Barcus et al.*, [1966] used two balloons and cross-correlation analysis to determine the spatial extent, and found that a separation of 100 to 200 km between the balloons gave a high degree of coherency between the two X-ray count-rate profiles but larger distances had poor correlation. *Parks et al.* [1968] used multiple detectors on a single balloon to also find scale lengths of 100 km during a pulsation event.

Many other studies have been made on pulsating aurora. *Parks and Winkler*, [1969] made simultaneous measurements of auroral X-rays and electron fluxes at the equator during a pulsation event and found good agreement in the frequency spectrum of the time variations but poor agreement in the actual coherency between them. Magnetic field fluctuations have been correlated with the optical pulsating aurora by *Oguti et al.* [1984] and also found to be well correlated. An analysis of timing and possible current modulation mechanisms by *Oguti et al.* [1984] led them to conclude that the source for the particle modulation was not local to the auroral ionosphere, and perhaps on the equator. This has also been proposed by *Bryant et al.* [1971] for observations of pulsations in the primary precipitating electrons. *Parks et al.* [1968] and *Brown and Weir*, [1967] noted a hardening of the X-ray spectrum during pulsations.

Pulsating aurora has attracted considerable theoretical attention. [*Coroniti and Kennel*, 1970] proposed a model in which ULF magnetic pulsations (3-300 sec period) modulate the pitch angle diffusion coefficient, alternating between weak and strong diffusion regimes. *Davidson* [1986] has suggested a mechanism that does not involve any external agent to modify the assumed whistler wave turbulence, but instead invokes a self quenching process. In this model, a feedback loop from the pitch angle diffusion to wave growth is described with a set of equations which yield oscillating solutions for the diffusion coefficient. A severe problem with these theories is that neither one can adequately explain the broad energy range (10's of eV to 100 keV) that is observed to undergo modulation during pulsating aurora, nor do they address the observed spatial features.

The purpose of this current work is to exploit the technique of X-ray imaging to obtain simultaneous measurements of the spatial, temporal, and energy features for a short pulsation event. This event was characterized by the classical 5-15 second modulations lasting for several minutes superposed on a slower varying component. The statistical limitations on the instrument will restrict the highest spatial resolving capabilities to apply only to the longer time scale features. New information on the spatial extent of the pulsation regions is still obtainable which shows only moderate localization and coherency. The scale lengths for a large "patch" are similar to those described in the literature for the optical pulsating aurora. The slower, several minute time scale component is attributed to motions of the source region. This analysis will be somewhat brief and will not have the detail of the previous chapter since the ability to make some of the important comparisons and correlations is not available.

4.2. Data

The balloon payload was launched at 1930 UT and reached ceiling altitude at about 2230 UT (2330 LT). The upper panel of Figure 4.1 shows a a four hour overview of the count rates measured by the X-ray imager for the period 2000 UT to 0000 UT. Note that bremsstrahlung X-rays were detected around 2200, but since the balloon was not at full altitude, these will not be discussed. The lower panels show the magnetic field measured at Andoya. A magnetic bay started about 2200 UT, corresponding to the X-rays as the balloon was still rising, and showed another onset at about 2305 UT. Maximum deflection (600 nano Tesla) was attained by 2330 UT.

The different characteristics of the long time-scale features will be examined by considering several different phases for the event, each one distinguished by a distinct interval of X-ray activity. The two hour time profile of X-ray fluxes in Figure 4.2 will illustrate these phases. The first interval corresponds to the second onset, at 2305 UT, and lasts from 2300 UT to 2320 UT. The second phase extends from 2320 to 2330 UT and corresponds to second intensification prior to the most intense X-ray fluxes, and the period of pulsations. The next interval, and the one following, correspond to the intense burst of X-rays at 2338 UT, and the subsequent abatement of activity. These phases were chosen by their distinctive temporal signatures and the possibility of motions of the source region as the cause of the modulations. These motions should be evident in the X-ray images.

These intervals have been 15-second averaged to reveal the longer time-scale (> several minutes) behavior. Other intervals of interest will be 5 second or 1 second averaged to examine the faster changing component. The bottom panel of Figure 4.2 shows a plot of the spectral-hardness. This is the ratio of the X-rays in the 50 - 110 keV to 20 - 50 keV energy channels, and is used as an indicator of the hardness or softness of the spectrum.

All images shown in this section will be presented in the manner to be described here. Each of the images have various statistical information printed below as discussed in Chapter 2. The spacing of the contours is adjusted to insure proper regard for the statistics, that is, the spacing is greater than the statistical fluctuation of the intensity values in each pixel (given as "RMS-Noise"). The exceptions to this are images of steep gradient, such as around 2338 UT, where the gradient falsely elevates the RMS figure. The absolute values of the contours are also consistent among the images so that it is easy to compare them to each other.

The spatial characteristics of the various phases are illustrated in two different ways. The first is through the images themselves, and the second is the use of a intensity profile along a cut through the image plane. This cut will be consistently taken through the image in the south-to-north direction, although at times there are intensity gradients present in a direction that is somewhat skewed from this direction. The intensity variations appear somewhat greater in the north-south direction, so this will be our primary focus. The objective is to seek continuous and consistent displacements in intensity enhancements as a function of time, that can be attributed to a motion of the source region. The intensity profiles will be grouped in threes for clarity in display, and the top panel has representative error bars for the uncertainty in image position (horizontal) and variance in intensity (vertical).

The first set of images and intensity profiles in Figures 4.3 and 4.4, respectively, are chosen to bracket the onset. The images indicate the formation of structure beginning with onset and returning to a more diffuse distribution as the intensities decrease. Note that the north-south gradient appears to have moved from south to north in the 2305 to 2310 UT period, but by 2313 UT there is very little gradient to the emission region.

The phase starting at 2320 UT, shown in Figures 4.5 and 4.6, indicates that the gradient in the X-ray fluxes is still present, with the slight intensity enhancement in the south. Five minutes later, structure appears in the western side of the image which increases in intensity over the next several minutes. In this case, the emission region is roughly centered in the image in the north-south direction, but remains offset toward the west.

The 2330 to 2340 interval shows a spatial structure that either migrated in to the viewing region from the north, or is a temporal, spatially stationary, flux enhancement. The first and second profiles (Figure 4.8) for this sequence suggest that the pre-2330 UT burst is not associated with the sudden appearance of the 2338 UT burst, since the 2331 UT profile suggests a disappearance of the structure to the south, while the later one indicates an appearance from the north. The images also suggest this to be the case. The 2331 UT and 2334 images (Figures 4.5 and 4.7, respectively) indicate a structure that is leaving the image area to the south-west, while the 2336 and 2338 UT image (Figure 4.7) suggest a northern appearance.

The decline of X-ray intensities will be discussed with the last sequence of images, Figures 4.9 and 4.10. The north-south profiles, in conjunction with the images indicate that the intense emission region in the north has migrated slightly east by 2340 UT, and in the next 10 minutes seems to decrease in intensity, but with no clear indication of motion in the viewing region.

The 2335 to 2340 UT interval had bursts of X-ray fluxes with 5-15 second periodicities. The time behavior of the X-rays during this interval is better described as bursts at regular intervals rather than a smooth oscillation of the intensity. These are shown in the upper panel of Figure 4.11. The lower panel contrasts these pulsations to an earlier interval without bursts. As mentioned above, the pulsation peaks are of too short a duration to obtain sufficiently good statistics for an analysis using full resolution images. The spatial and energy characteristics will be examined by summing together several pixels to obtain an image area that consists of only four pixels. This will allow a first order study of the amount of localization to the pulsations and, if localized, the location of them.

The results this sector analysis is shown in Figure 4.12. The four panels correspond to four spatial quadrants, south-west, north-west, south-east, and north-east, moving from bottom to top panels. The four panels indicate that single pulsation peaks are often localized, but in different regions of the imaged area. Some of the bursts, for instance at 2339:10, are seen in all quadrants. However, for burst activity that occurs near the center of the image plane the signature of the burst will be distributed equally to all quadrants, so this analysis must be interpreted with caution. The north-east quadrant (lower panel) has the highest average fluxes but also the most variability. Figure 4.13 shows the energy spectrum for each of the four quadrants. The softest spectrum is associated with the region with the highest X-ray intensities, the north-east quadrant.

The lower panel of Figure 4.2 shows the temporal behavior of the energy spectrum as indicated in the "spectral hardness" index, defined above.. The spectrum appears to be softening as the count rates increase, although these spectral changes do not exhibit the same variability in time as the total count rates do. The softest energy spectrum occurs at or near 2320 UT, but the maximum in total X-ray fluxes does not occur until about 2340 UT. The initial interval of the event, during which there are no pulsations, is generally harder in precipitating electrons than the final interval, which is characterized by the 5-15 second pulsations. Besides the softening trend, a considerable amount of variability in the spectrum is also evident. This trend indicates a hardening in the spectrum of precipitating particles both early and late in the event. This is apparent at roughly 2310 UT, just as the count-rate is increasing, and again near 0005 UT when the count-rate is decreasing.

4.3. Discussion

The points we wish to make with the above information are the following: (1) The images indicate stronger activity in the south during early phases of the event than in later phases, and there is a general northward trend to the precipitation region. (2) The changes in X-ray fluxes at the balloon appear to sometimes be due to a motion of the source, and at other times to a temporal change in the source region.

(3) The amount of spatial structure in the X-ray emissions shows dependency upon both the energy spectrum and the count rates, although there is a stronger dependence on the spectrum. (4) The pulsation region shows only a moderate degree of localization. The pulsation activity is also associated with a region of softer precipitation energies, and has a scale length of about 40 km for the emission region. (5) There is good agreement between the UV emission morphology and the X-ray source region.

The question of bulk motion as a cause of the modulation in X-ray count-rate during the event is hard to address if there is a lot of variability in time of the spatial forms, since identifying motion requires a feature in the image to be tagged and then to watch the motion of this feature across the field. This sort of variability appears to be a characteristic of this event on this slower time-scale, making a definitive identification of source-motion difficult. The activity during the early phase (before 2320 UT) appears stronger in the south than in the north, and this tendency is reversed in the latter stages of the event, with more activity to the north of the balloon. The overall motion of the active region from south to north during the breakup of the event is consistent with previous findings [*Kremser et al.*, 1982; *Tanskanen et al.*, 1987].

The sequences of images also reveals small-scale structure, as well as the sense of motion discussed above. This structure of the precipitation source imbedded within the northward tending large-scale precipitation region is a new observation for energetic (>20 keV) particles, although *Mauk et al.* [1981] saw similar scale lengths in a stationary precipitation region. Spatially structured aurora with scale lengths on the order of tens of kilometers is of course a well known feature of the visual aurora during active times. The observations of similar scale-lengths in the X-ray emissions implies that the underlying mechanism for the small scale morphology for both the optical and the X-ray emissions are not in the auroral acceleration region, since this will have little effect upon the electrons producing the X-rays, but lies much deeper in the magnetosphere.

The sequence of intensity profiles does, at times, suggest that an enhanced precipitation region has moved into or out of the field of view. This appears to be predominately in the north-south directions, but at times shifts slightly eastward or westward. The most intense emission period, around 2338 UT, appears to be an exception to this. In this case there is a possibility for movement into the field of view, but the region appears to then temporally decrease in intensity. Note that this is also the time period for the pulsation activity.

The pulsation activity occurs when the precipitation region has the smallest spatial structure during this event, attaining a form suggestive of a beam-like structure to the precipitating energetic electrons. This type of localization of the emission region is similar to that reported for the visual pulsating aurora [*Royrik and Davis*, 1977]. Pulsating aurora has been theoretically attributed to a temporal modulation of the *Kennel and Petschek* [1966] pitch angle diffusion model [*Coroniti and Kennel*, 1970] This explanation relies upon the existence of a loss cone that is filling and emptying with two different time scales. However, in the region of continuing particle injection, such as near midnight during the main phase of the aurora, the rapid filling of the inner magnetosphere with fresh plasma may fill the loss cone before diffusion processes can be driven by the loss cone anisotropy. The resolution to this is that these pulsations are occurring during recovery, and injection of new plasma may have ceased.

The energy spectra for the four sectors examined shows a slightly softer spectrum for the region of higher X-ray intensity, and also indicates the presence of a soft component superposed on a harder one. This is a feature which persists in much of the X-ray data for the post-breakup phase. *Mauk et al.* [1982] and *Mauk and Parks* [1981] reported observing a two component energy spectrum with an e-folding energy of about 10 keV for the lower energy component and X-ray enhancements are primarily below 45 keV in energy. The implications for this in the context of magnetospheric processes is that there are two different processes, one process is modulating the lower energy electrons while another is affecting the higher energy particles in a different way. These could be either acceleration mechanisms, loss cone diffusion process, or a combination of both. Note that the energy break in the spectrum occurs near 60 keV. This is close to the cross-tail potential, which is one possibility for energization of the lower energy component.

The polarity change in the vertical component of the magnetic field at Andoya indicates a motion of the overhead current sheet in a south to north direction. This is in the same sense as the general trend in activity to move from predominately in the south to predominately in the north. Although no explicit motions in the X-ray emission region are found that can be well correlated with the motion of the current sheet, the sense of motion is correct.

The importance of the spectral characteristics is also seen in the observed dependence of the amount of spatial structure upon the spectrum of the bremsstrahlung X-rays. The association of a more structured source region and the presence of softer X-rays suggests that the lower energy component (20-50 keV) of precipitating particles are modulated by a different mechanism than the higher energy component. However, the energies of these "low" energy particles are beyond the range of observed ionospheric acceleration mechanisms. The implication is that we are observing structure which has its origins much deeper in the magnetosphere.

The ultraviolet (UV) images (Figures 4.14-4.17) from the Viking satellite during the interval 2330 - 2340 UT show an arc-like feature in the vicinity of the balloon, which is located at 68.2° latitude and 19° longitude geographic (longitude and latitude lines are drawn for reference in Figures 4.16 and 4.17; the two longitude lines are at 18° and 20°, the 18° label is somewhat obscured). Note that the appearance and disappearance of the arc is fairly well matched by the growth and decay of X-ray intensity. Furthermore, many of the spatial characteristics apparent in the UV images are also seen in the X-ray characteristics. These include the rapidly changing spatial forms and the breakup into smaller patches by 2340 UT.

4.4. Conclusion

In conclusion, we see that two different observations are both associated with the softer component of the bremsstrahlung X-rays; the degree of structure in the precipitation region and the regions of enhanced X-ray emission. The temporal modulations of X-ray fluxes can possibly be attributed to motions of the source region some of the time, but there is also evidence of purely temporal modulations. The latter is associated with the most intense emissions of the event and also the onset of 5-15 second pulsations. The general sense of motions during the event is south to north, and this is most evident for a large region of X-ray activity rather than s quasi-static spatial form which migrates northward. The time scale for the slow spatial motions and temporal variations is several minutes, while the spatial scales are as small as 30-50 km during the most intense emissions of the event. The spatial morphology of the X-ray source is in fairly good agreement with the spatial characteristics of the UV emissions.

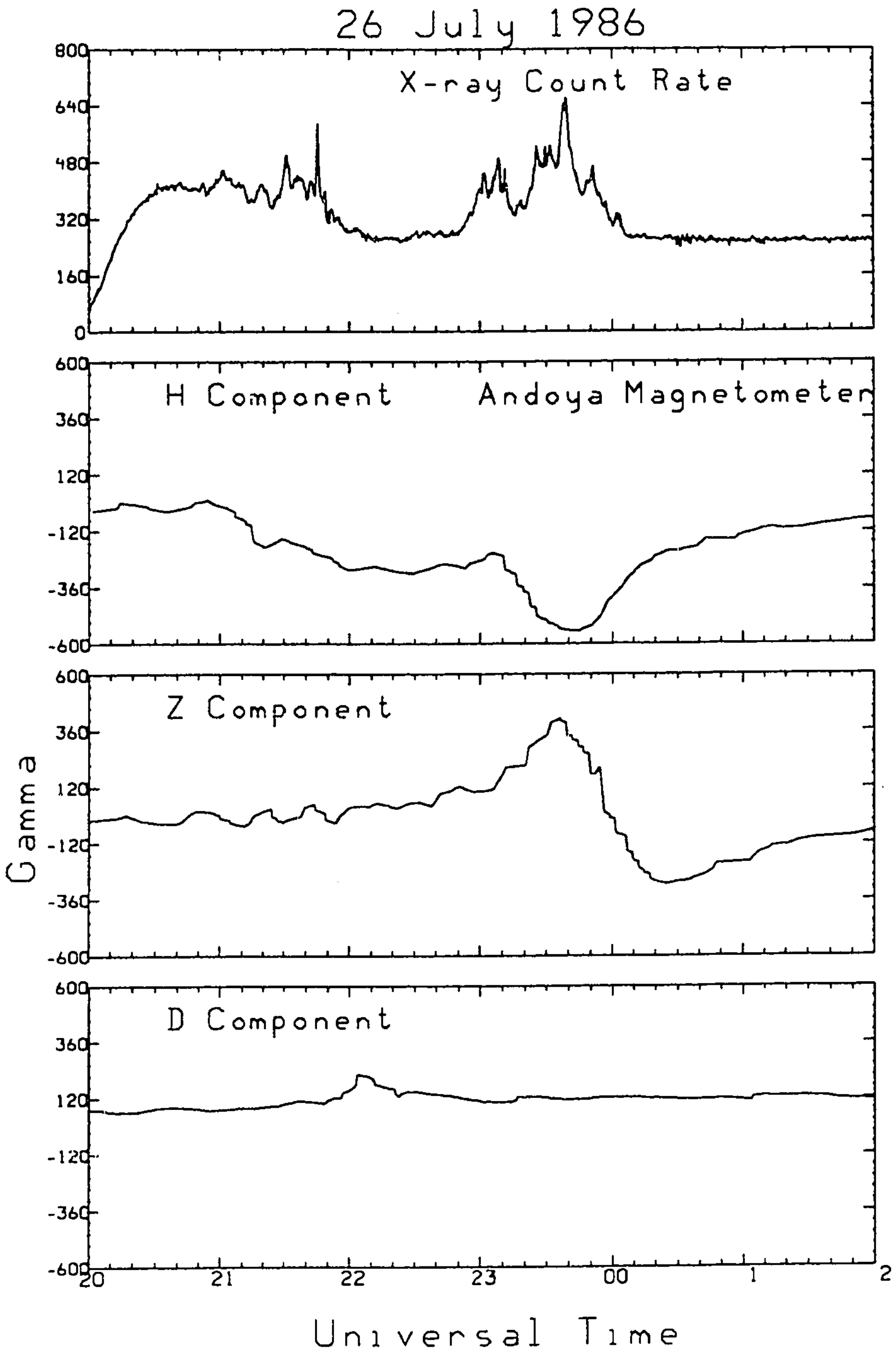

Figure 4.1 X-ray count rate and Andoya Magnetogram.

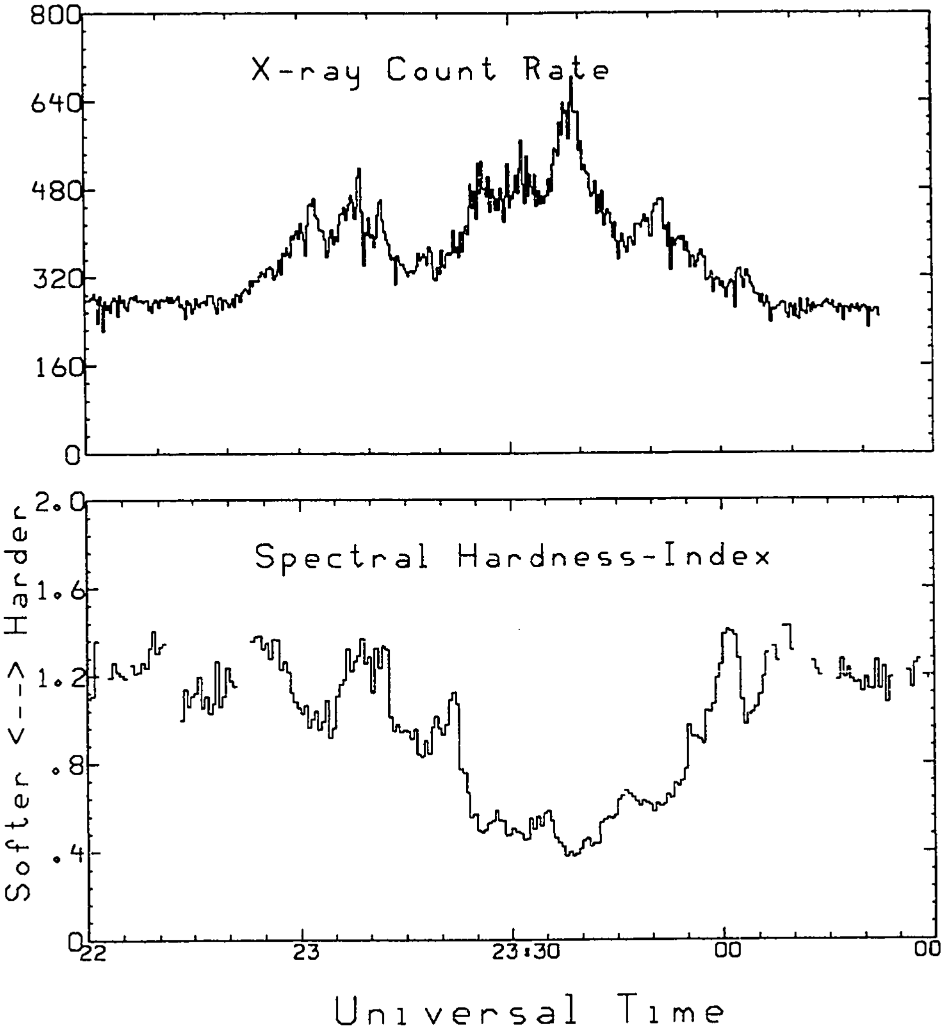

Figure 4.2 X-ray count rate and spectral index, 2230 - 0030 UT.

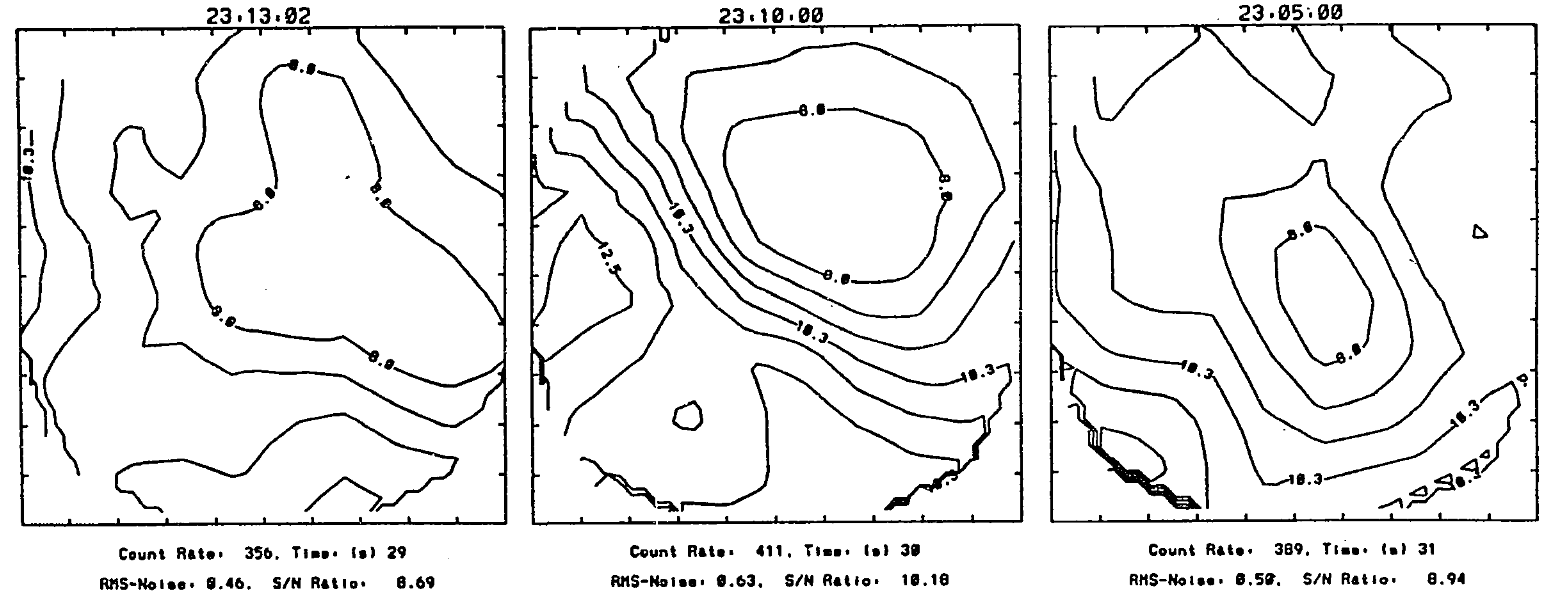

Figure 4.3 Sequence of images during early phase of the 2250-0010 UT portion of the event.

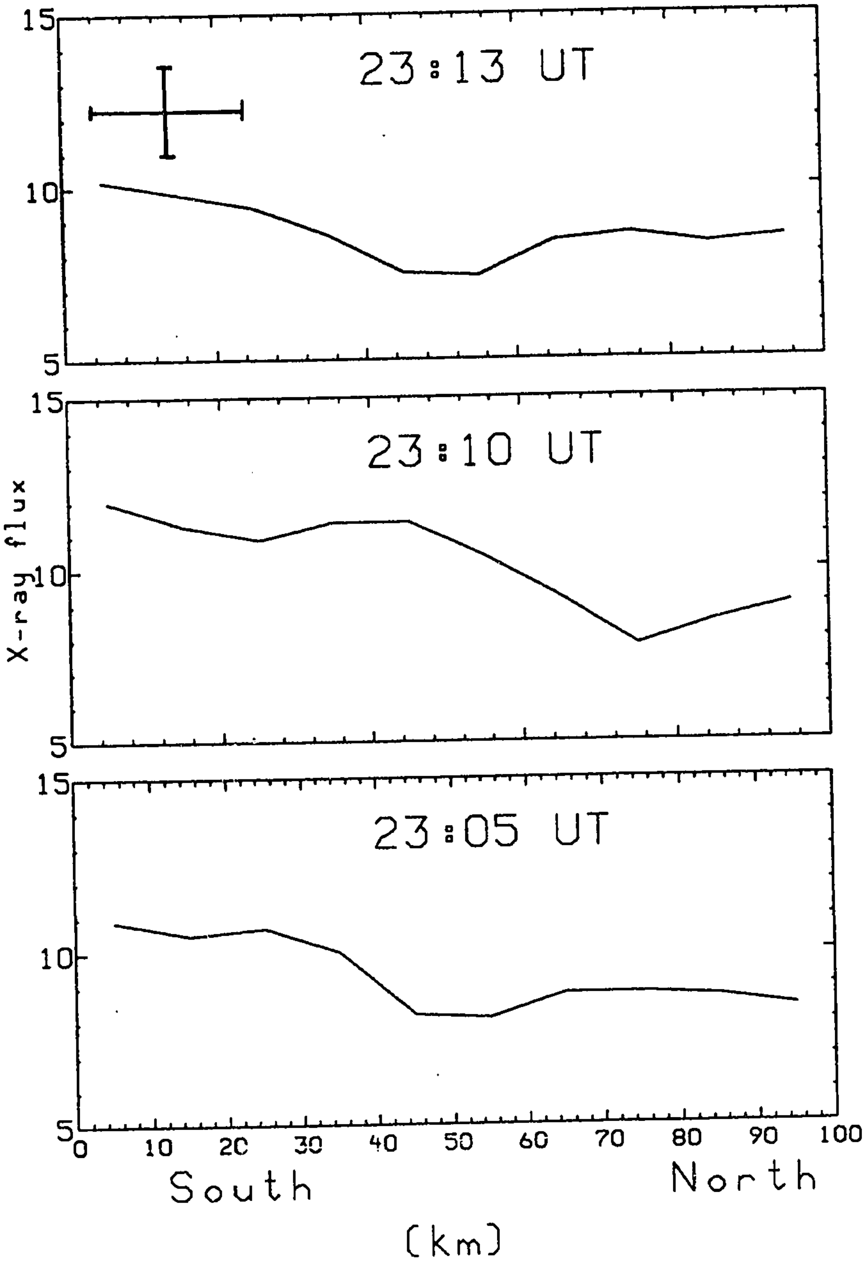

Figure 4.4 Sequence of North-South intensity profiles for the sequence in Figure 4.3.

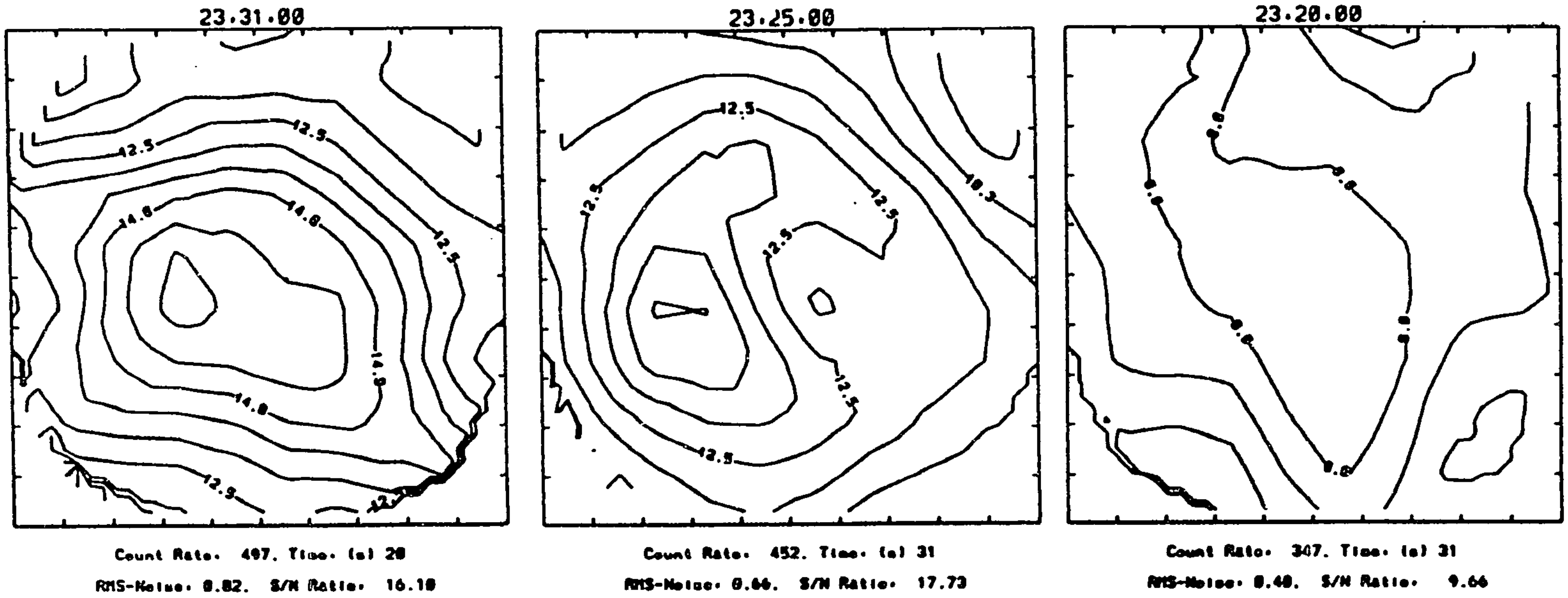

Figure 4.5 Sequence of images during the intensification of the 2250-0010 UT event.

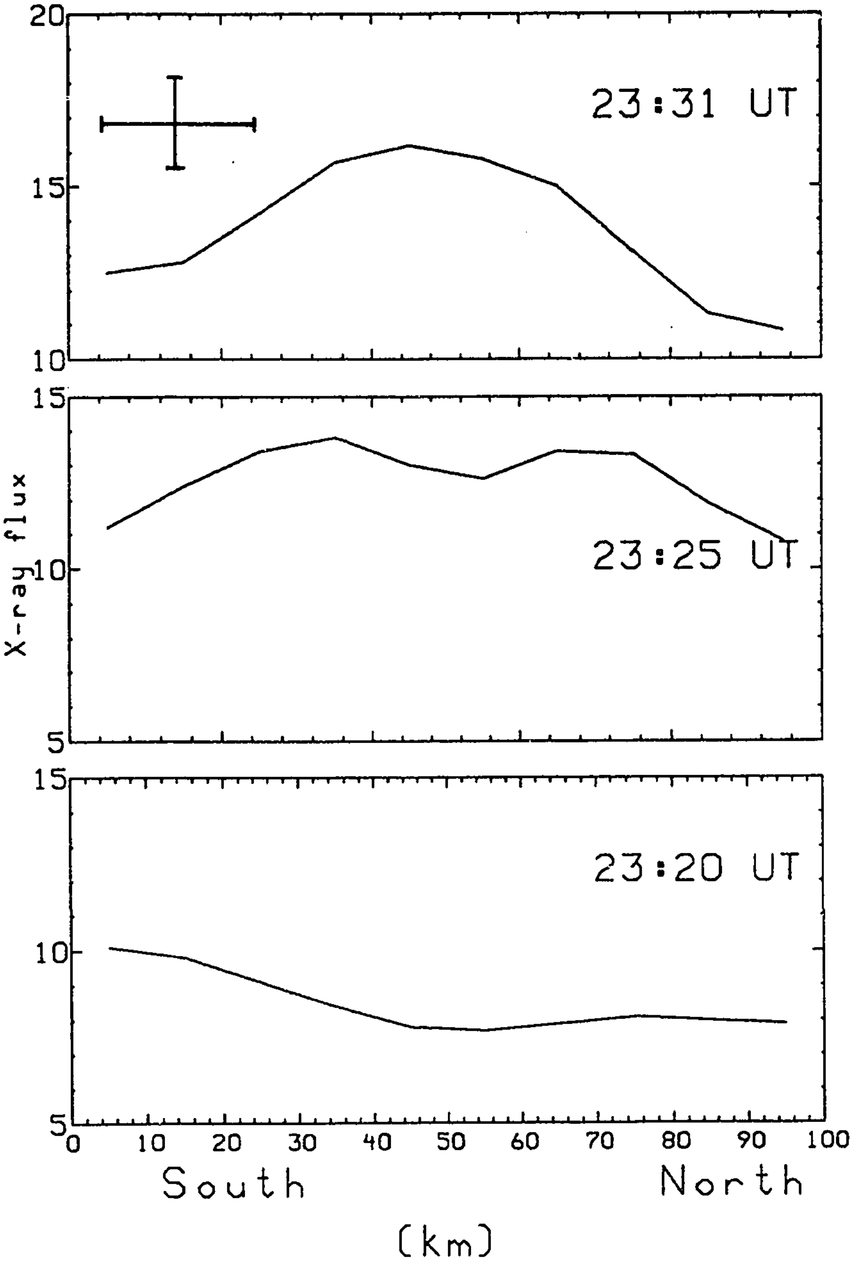

Figure 4.6 Sequence of North-South intensity profiles for the sequence in Figure 4.5.

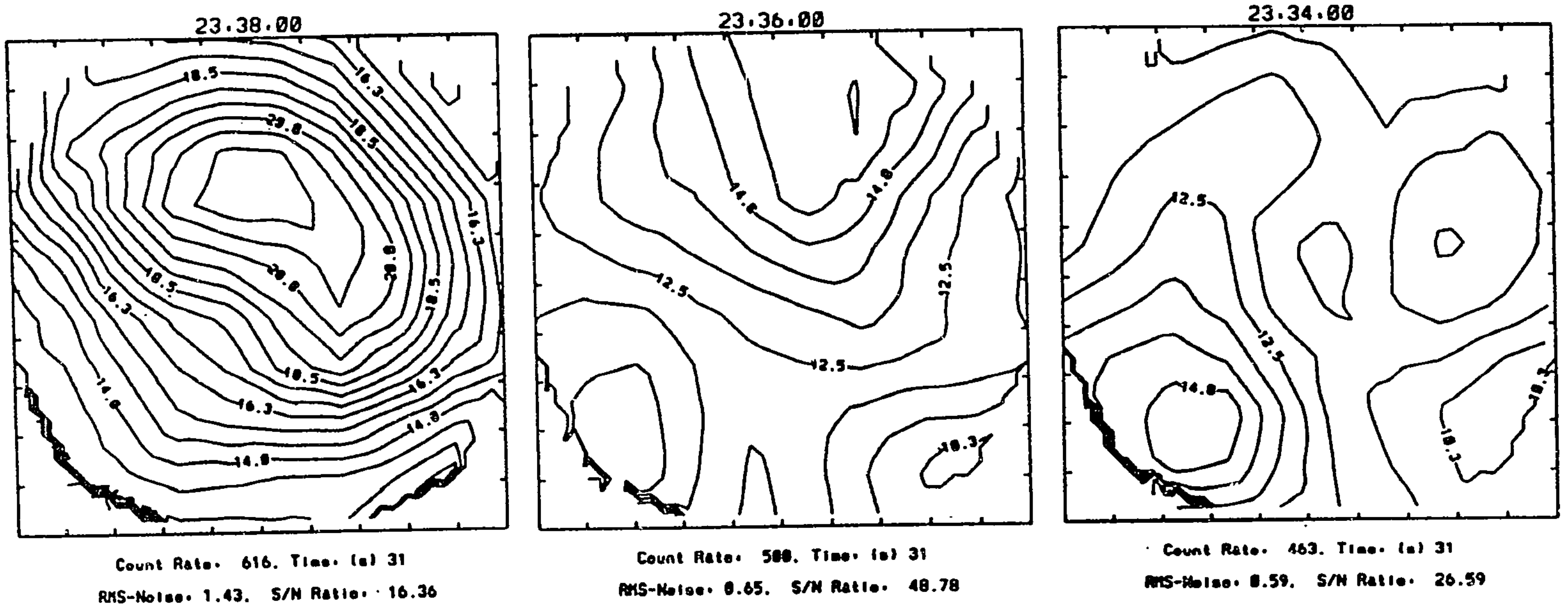

Figure 4.7 Second Sequence of images during event intensification.

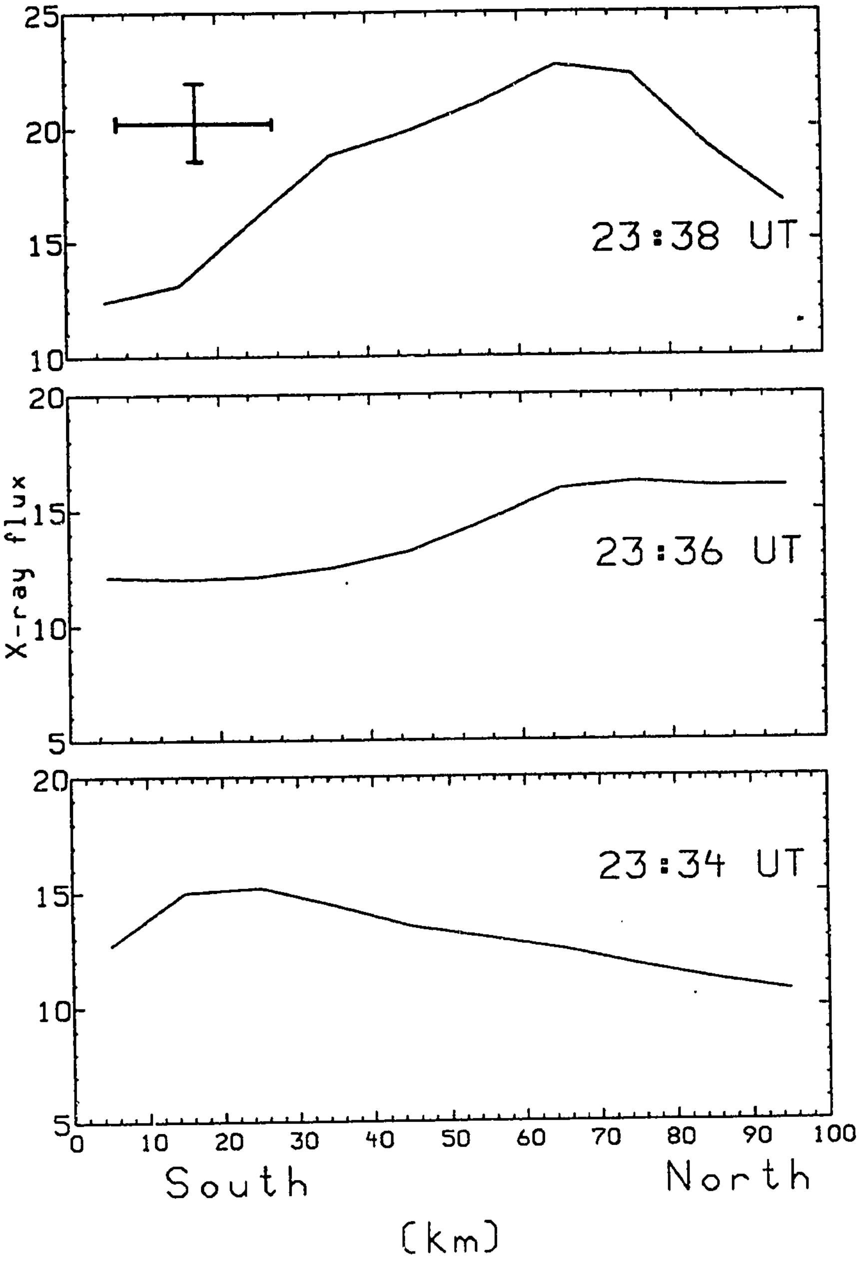

Figure 4.8 Sequence of North-South intensity profiles for the sequence in Figure 4.7.

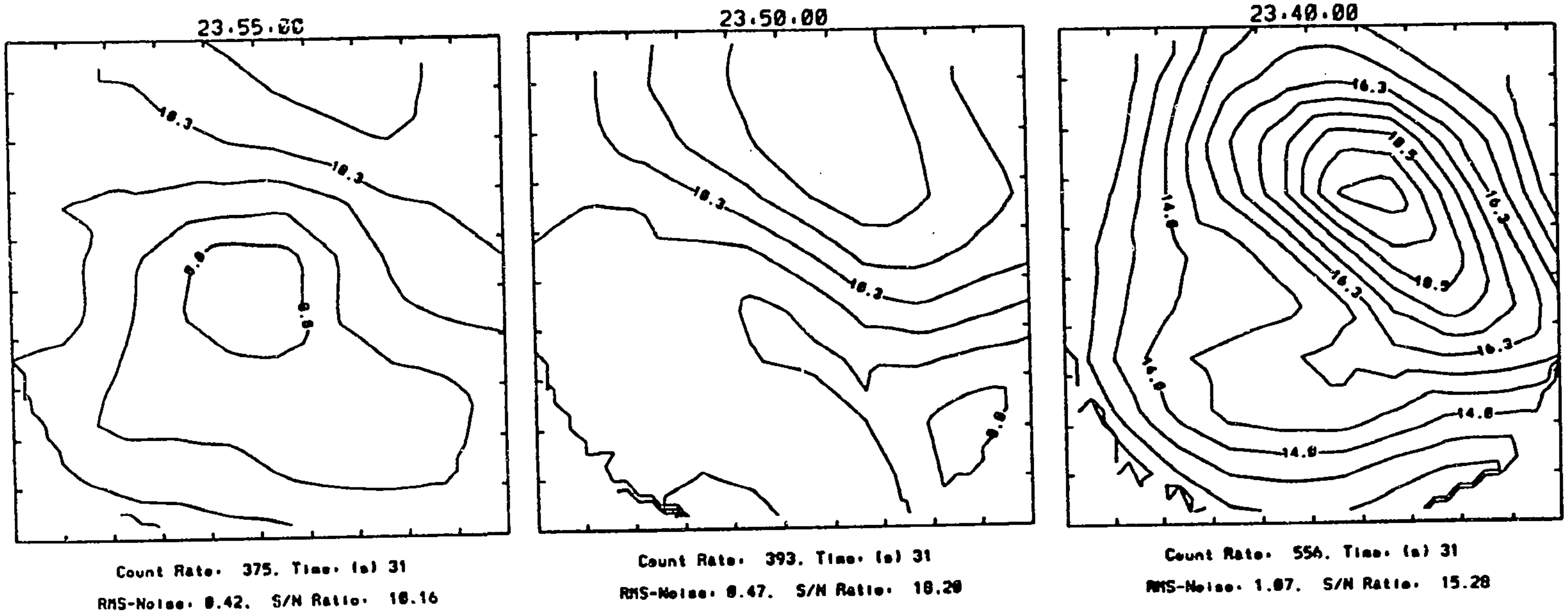

Figure 4.9 Sequence of images obtained in the ending phase of the 2250-0010 UT event.

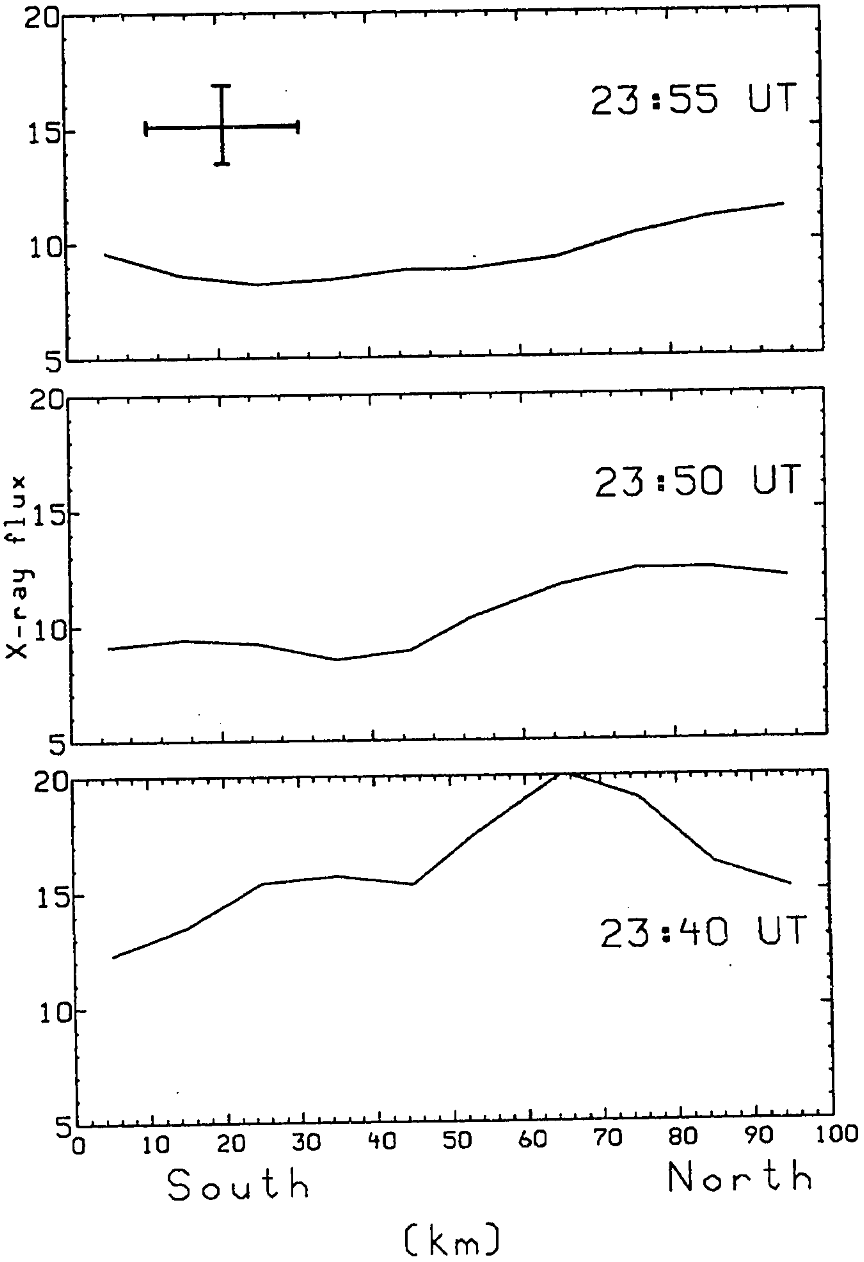

Figure 4.10 Sequence of north-south intensity profiles for the sequence in Figure 4.9.

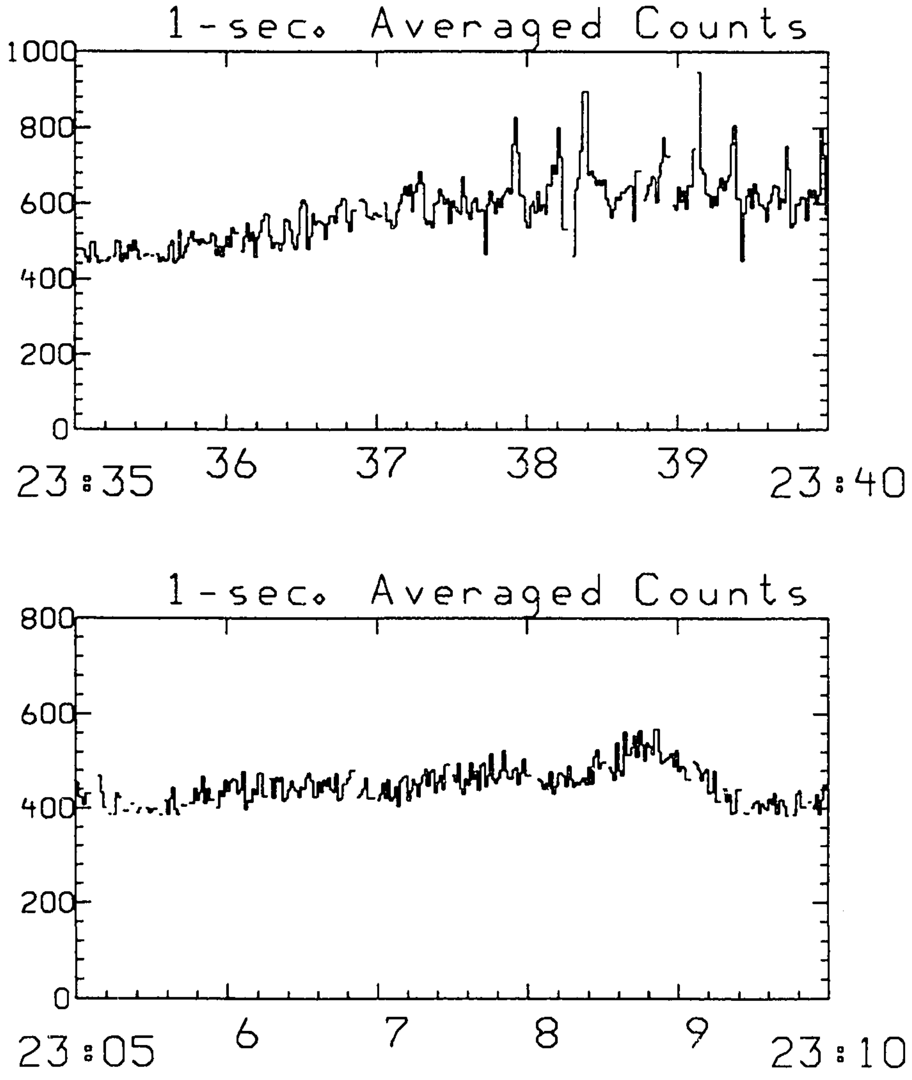

Figure 4.11 X-ray count-rate profile of 1-second averages at 23:30 - 23:40 illustrating the pulsation character. An earlier segment of data is shown for comparison in the lower panel.

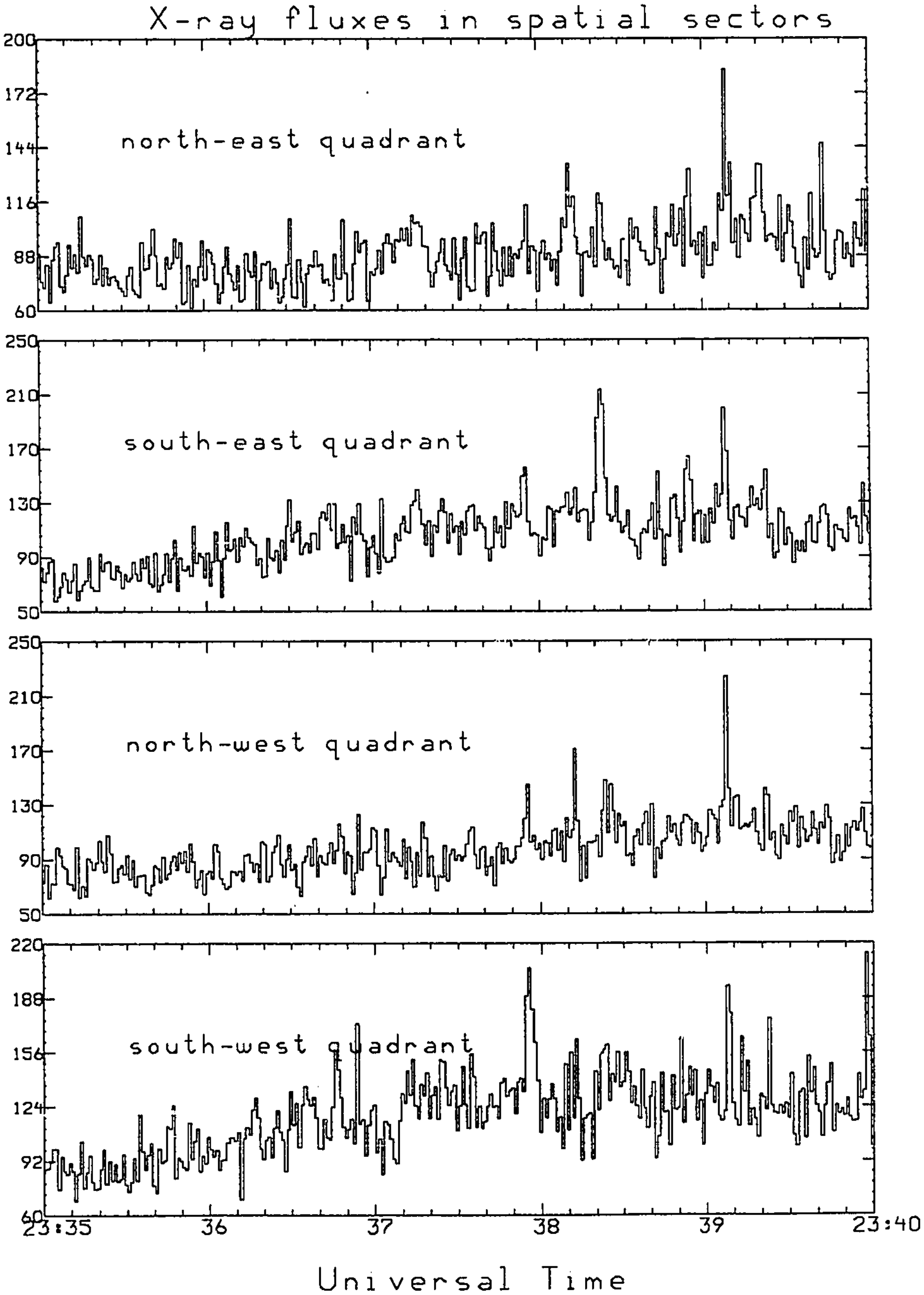

Figure 4.12 Count rates during the pulsation interval for four of the image-area quadrants. The panels correspond to spatial quadrants, south-west, north-west, south-east, and north-east, moving from bottom to top panels.

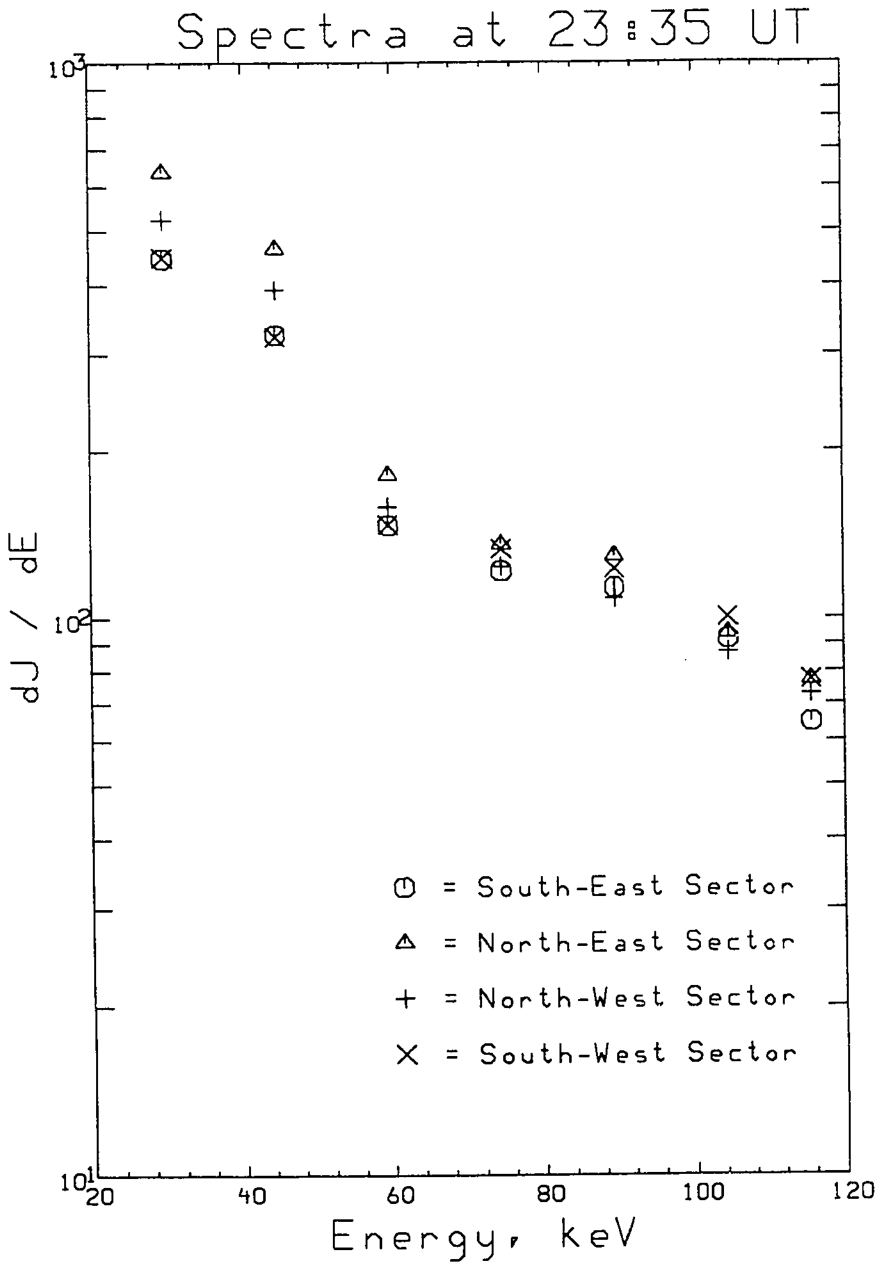

Figure 4.13 Energy spectra from four quadrants of the imaging area during the interval 2335-2340 UT.

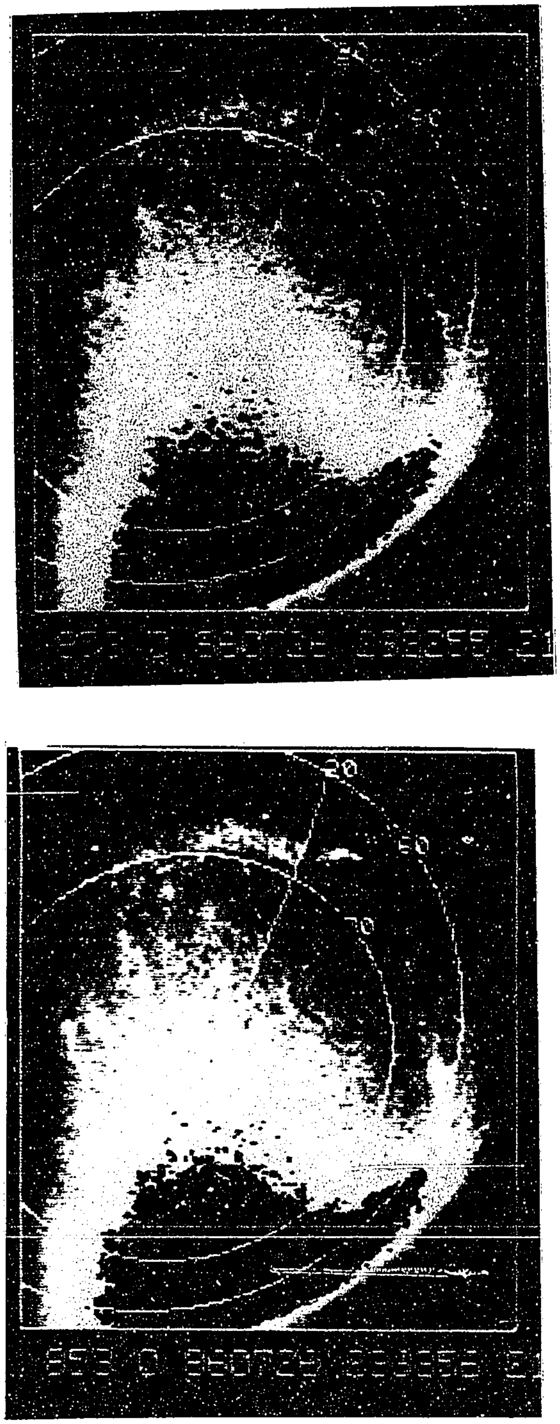

Figure 4.14 Viking UV images at 2333 and 2334 UT.

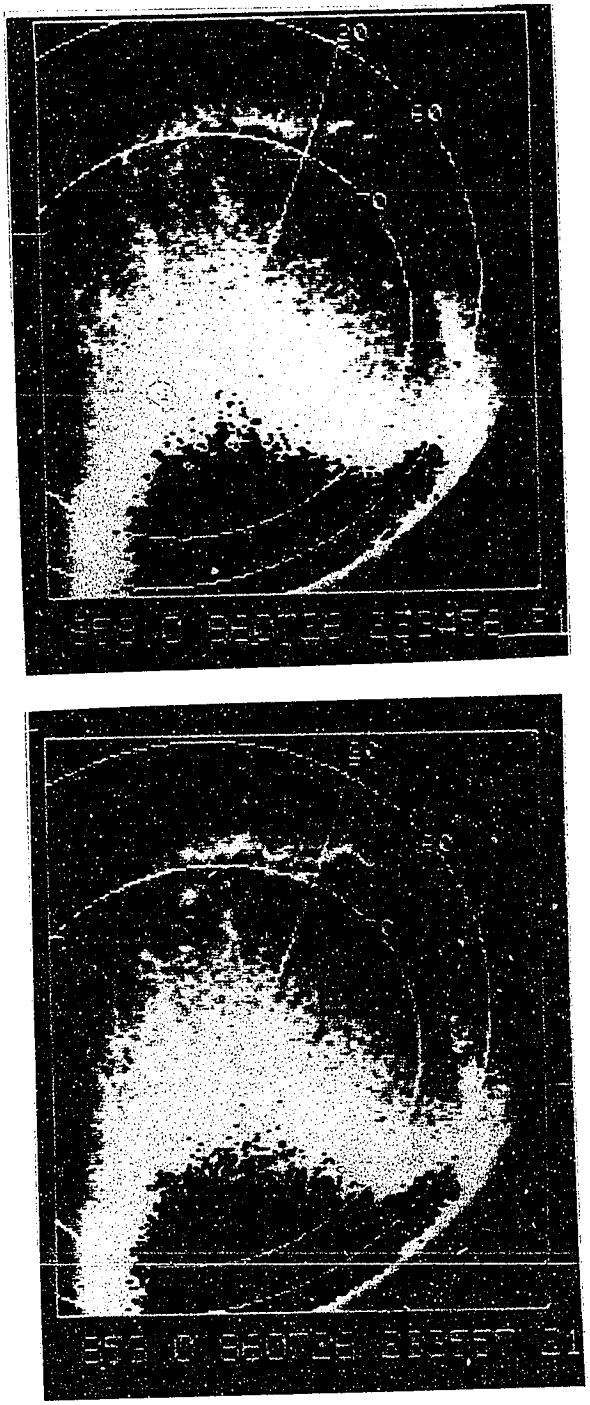

Figure 4.15 Viking UV images at 2335 and 2336 UT.

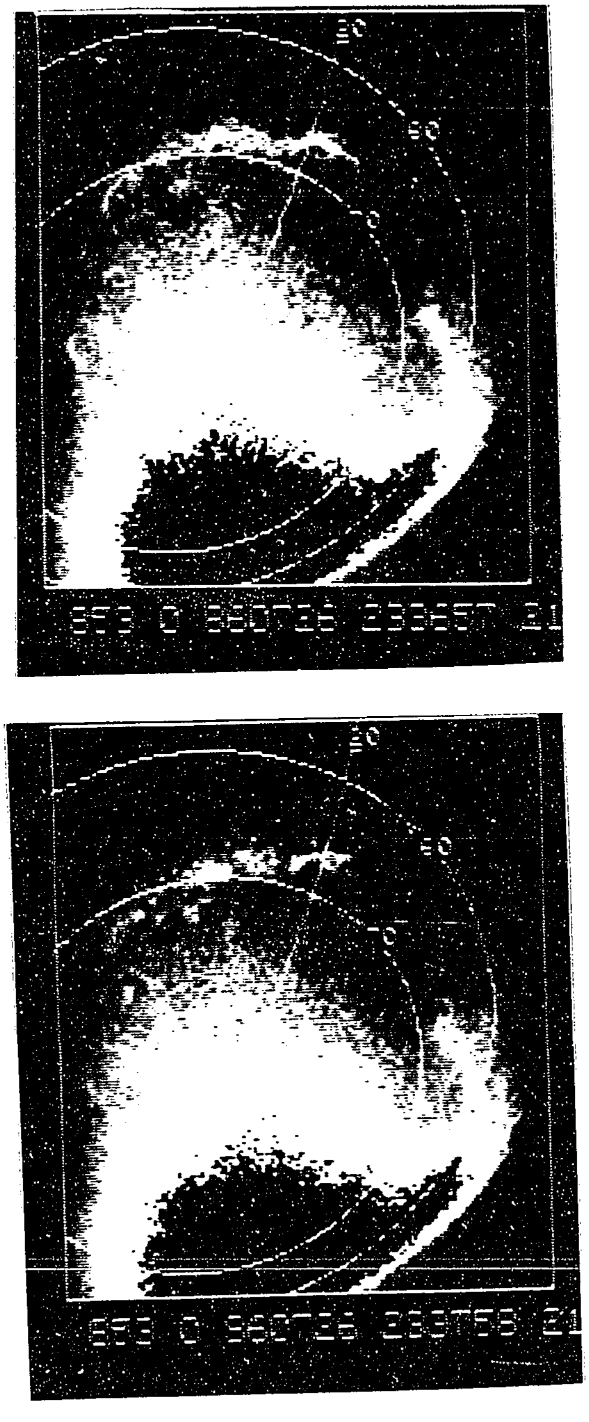

Figure 4.16 Viking UV images at 2337 and 2338 UT.

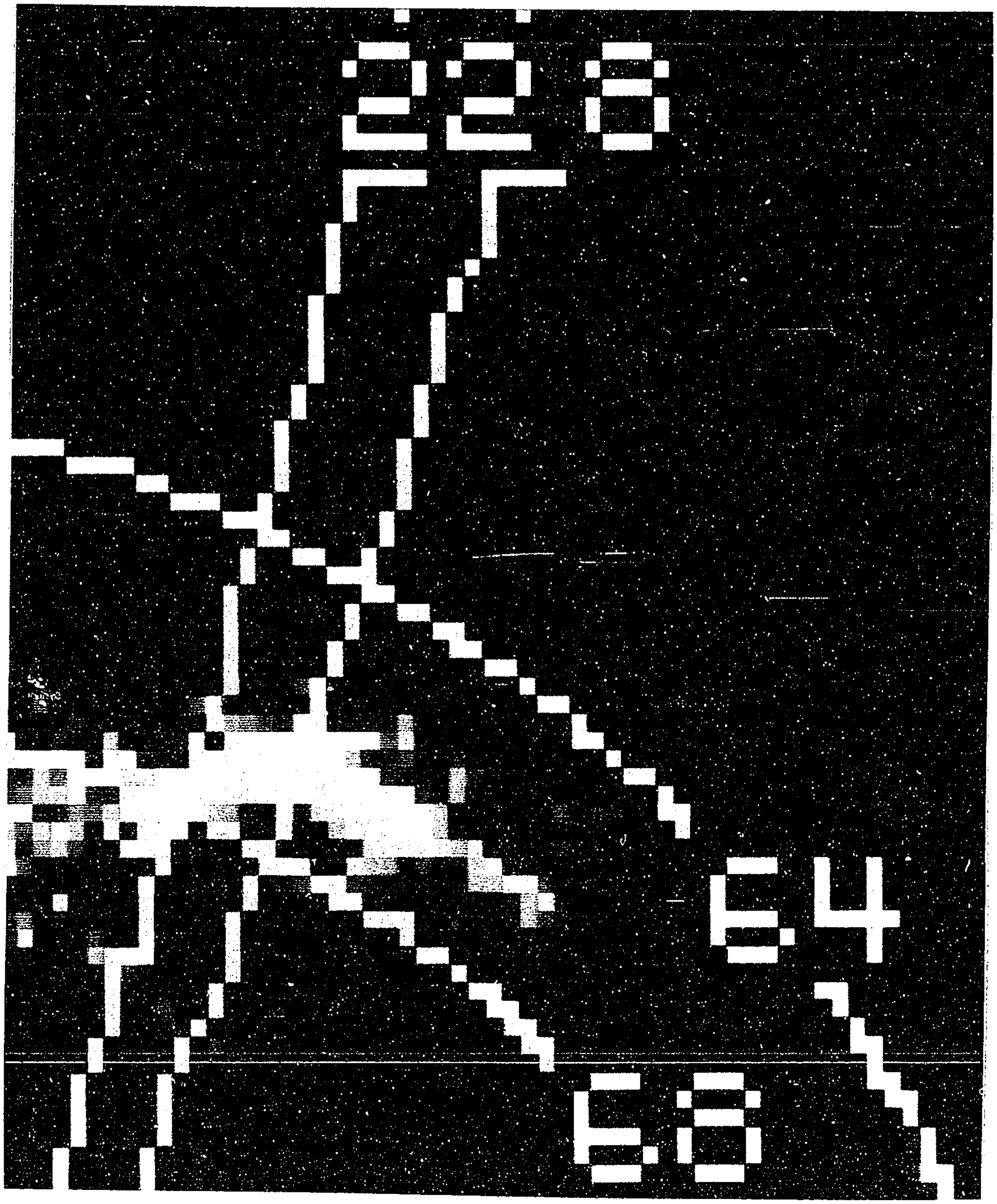

Figure 4.17 Blowup of the 2337 UV image in Figure 4.16, with geographic latitude lines (18° and 22°) and longitude lines (64° and 68°) superposed. The balloon was at 19°, 68.2°.

Chapter 5

Summary and Concluding Remarks

5. Scientific Results

The common thread throughout this work has been the study of energetic particle precipitation through the measurement of the by-product of this process, bremsstrahlung X-rays. For the case of the dayside precipitation the experimental results have added new information to the details of the relationship between a nightside source and the loss of these drifting particles on the dayside. The strong indications of dynamical processes local to the dayside and the lack of a clear cause-effect relationship between the time variations in the energetic particle fluxes and the precipitation losses suggests that the precipitation mechanism is influenced by events outside of the drift induced wave-particle-interaction model. This conclusion does not necessarily reject the drift-precipitation model, rather it may indicate a perturbation on it.

Pulsating aurora is widely believed to also be a truly temporal process, and the most popular theories also involve modulations of the *Kennel* [1969] process of wave-particle interactions that induce scattering into the loss cone. These two events we have studied are both examples of probable wave-particle interactions, but also serve to illustrate how little we really know about the details of the process. There is a strong need of additional measurements and theory to fully understand this.

The theory of whistler waves which cause scattering into the loss cone is quite attractive in many respects; the whistler grows in the presence of a loss cone distribution, which is a characteristic of magnetospheric particles, it can interact with the correct energy particles, and it is often observed ("hiss" or "chorus") in the magnetosphere. However, the experimental correlation between natural precipitation as a direct result of whistler waves is not always good. For example, *Kremser et al.* [1986] found some periods of very good agreement between wave amplitudes in the equatorial magnetosphere and bremsstrahlung X-rays, but also other instances of little or no correlation. Other problems in the theory include the fast changes that are sometimes observed, such as micro-bursts (10 Hz), or the very broad energy range of particles that are modulated (10 to 10^5 eV) in pulsating aurora. The first implies growths that are faster than reported, the second indicates a very broad bandwidth of whistlers.

A theoretical re-examination of these problems should include a better calculation of the whistler growth-rate, including the effect of inhomogeneities. If the time scale for wave growth is fast relative to the time scale for loss of wave energy from the region, than saturation amplitudes will be a more important quantity to calculate than growth rates. This corresponds to any diffusion regime that is above the weak limit, which is probably the case with the intense dayside events and during the pulsation peaks in pulsating aurora. Other wave modes should be examined for more favorable growth rates, including the various drift modes. The latter is potentially very important at the plasmapause and may be important in places of local inhomogeneities, but probably not for the pulsation events.

5.1. Future Work

In general there are two experimental methodologies in space physics; statistical studies and event analysis. The latter can be used to elucidate the fine details of the physics for various processes which may or may not represent typical behavior for the class of phenomena to which the event belongs. In other words, the statistical significance of the final conclusions is not determined. The statistical approach considers an ensemble of events and can therefore determine the average behavior, extremes, etc., but may gloss over the detailed physics. In complex systems such as substorm processes, the task of defining the class of events to comprise an ensemble requires sufficient knowledge to isolate the desired effect, that is, a set of criteria for event selection. This necessitates sufficient knowledge to define and identify the proper events, and this knowledge must evolve through detailed analysis of individual events. These two approaches are a direct result of the impulsive, highly variable nature of time-dependent magnetospheric processes which dictates what is to be measured. The two techniques should be viewed as complimentary rather than competitive. In this sense, the X-ray studies in this thesis (event type analyses) would be well augmented by statistical studies of similar experiments. This can be achieved either with long duration balloon flights or many individual launches.

In the context of obtaining statistics, the results of the morning sector analysis would again require the presence of geostationary spacecraft to perform a similar study of the drifting particles. For studying any precipitation event in terms of wave particle interactions, it is extremely useful to have VLF and ELF wave data that can be correlated with the X-ray data. This combination is very reasonable in terms of size for balloon payloads and would yield very good science.

For the case of dayside dynamics, there are few direct measurements of the high energy (10 keV to relativistic) precipitating electron component, yet this energy regime is very important in this sector. A compliment to the above experiment would be the in situ measurement of the precipitating particles' velocity distributions with a rocket payload. In this situation, the balloon payload would provide information on the long-time scale and spatial features, which could be used in real-time to optimize the launch time for a sounding rocket. The rocket would obtain high time- and energy-resolution information on the primary electrons and ions, as well as adding further knowledge to the relationship between precipitating electrons and bremsstrahlung X-rays. The plasma wave (VLF and ELF) experiments in conjunction with the particle and X-ray data would help understand the exact mechanisms involved in the often observed intense precipitation in the morning sector, as well as the various different temporal modulations of the energetic particles in the early to late morning and noon sectors (e.g., pulsations and micropulsations). This experiment may sound somewhat grandiose relative to the imaging experiment, but in terms of current graduate student experimental training it is probably well suited for PhD theses.

5.2. Future Experimental Improvements

The use of X-ray imaging as an investigative tool for magnetospheric research can be very powerful. The deconvolvement of space-time effects is one of the difficult problems in conducting space plasma physics experiments, and imaging the auroral ionosphere provides one method of overcoming this problem. The method is not without shortcomings. The X-ray imaging technique is heavily controlled by statistics, due to both the source emissions and to the response of the instrument. The ability to obtain good results is determined largely by how many X-rays can be analyzed, which is a function of the emission intensity and the instrument throughput. There is a reciprocal relation between the resolving ability in space and time, but the ultimate resolution still cannot be any better than the intrinsic limits of the instrument. Since we have no control on what the X-ray fluxes will be, but do have some idea what they are during times of activity, the best that can be done is to attempt to improve the statistics through a better instrument.

The ideal X-ray imager must be able to use all information, all of which has minimum error introduced by the instrument. As discussed in this thesis, the reduction of instrument error requires careful attention to the scintillator-PMT geometry and to the electronics. For low energy X-rays, which constitute the bulk of the measurements, maximizing the information means minimizing the loss of scintillation photons. This is the philosophy behind the use of hexagonal PMTs that can be close-packed. Losses can be further minimized with the optical configuration; reduce the number of internal reflections to increase the number transmitted into the PMT.

Information can also be maximized by using all X-rays in image computation. Currently, the system is data rate limited, so X-rays are rejected after the limit for the frame has been met. Improvement can be achieved either through more sophisticated algorithms for the on-board computation of positions, or by significantly increasing the telemetry rate. Data rates are often fixed by practicable experimental constraints so the computational process is the area of improvement that will be most beneficial.

There are many other improvements that can be implemented. For instance, one possibility is to have the aperture size be determined dynamically by the computer. This could be influenced by such things as the X-ray fluxes or the type of activity. Fast pulsations can be temporally resolved with poor spatial resolution by opening up the aperture, while slower time scale features with high fluxes would have the aperture stopped down. Other improvements in the imaging technique could be instituted by attempting to reduce the statistical nature of the distribution of scintillation photons in the optics. In particular, one possible design would involve a significant departure from the present design by using a segmented scintillator with an image intensifier.

Ultimately, however much the imager is improved, additional measurements are still necessary to deduce source characteristics. These ideally would include VLF and ELF plasma wave data, and particle measurements from satellite or rocket. As discussed in the introduction, X-ray imaging is a good technique for measuring a particular aspect of energetic particle dynamics, the mechanism for acceleration or filling the loss cone, but must be accompanied with other measurements to obtain logically and physically sound conclusions. This, however, is true in many other experiments in space physics and does not in itself limit the usefulness of the X-ray imaging technique.

Bibliography

Akasofu, S.-I., *Polar and magnetospheric substorms*, Springer-Verlag, New York, 1968

Anger, H.O., Scintillation Camera, *Revs. Sci. Instr.*, **29**, 27, 1958

Arfken, G., *Mathematical Methods for Physicists*, Academic Press, New York, 1985

Barcus, J.R. and T.J. Rosenberg, Energy spectrum for auroral zone X-rays, 1, Diurnal and and type effects, *J. Geophys. Res.*, 71, 803, 1966

Barcus, J.R., R.R. Brown and T.J. Rosenberg, Spatial and temporal character of fast variations in auroral-zone X-rays, *J. Geophys. Res.*, 71, 125, 1966

Berger, M.J., S.M. Seltzer, and K. Maeda, Energy deposition by auroral electrons in the atmosphere, *J. Atmos. Terr. Phys.*, **32**, 1015, 1970

Berger, M.J. and S.M. Seltzer, Bremsstrahlung in the atmosphere, *J. Atmos. Terr. Phys.*, **34**, 1015, 1971

Bewersdorff, A., G. Kremser, J. Stasdnes, H. Trefall, and S.L. Ullaland, Simultaneous balloon measurements of auroral X-rays during slowly varying ionospheric absorption events, *J. Atmos. Terr. Phys.*, **30**, 591, 1968

Brice, N. and C. Lucas, Influence of magnetospheric and polar wind on the loss of electrons from the outer radiation belt. *J. Geophys. Res.*, **76**, 900, 1973

Brown, R.R. and R.A. Weir, Energy-dependent modulation in auroral X-ray pulsations, *J. Geophys. Res.*, **72**, 5531, 1967

Bryant, D.A., G.M. Courtier, and G. Bennet, Equatorial modulation of electrons in a pulsating aurora, *J. Atmos. Terr. Phys.*, **33**, 859, 1971

Bryant, D.A., Wave acceleration of auroral electrons, Proceedings of the 8th Symposium on European Rocket and Balloon Programmes and Related Research, ed. T. D. Guyenne and J. J. Hunt, ESA Publications, ESA SP-27, 1987

Burton, R.K. and R.E. Holzer, The origin and propagation of chorus in the outer magnetosphere, *J. Geophys. Res.*, **79**, 1014, 1974

Chang, H.C., U.S. Inan, and T.F. Bell, Energetic electron precipitation due to gyroresonant interactions in the magnetosphere involving coherent VLF waves with slowly varying frequency, *J. Geophys. Res.*, **88**, 7037, 1983

Chiu, Y.T., Electrostatic field line mapping, *J. Geophys. Res.*, **79**, 2790, 1974

Chiu, Y.T., A.L. Newman and J.M. Cornwall, On the structure and mapping of auroral electrostatic potentials, *J. Geophys. Res.*, **86**, 10029, 1981

Coroniti, F.V. and C.F. Kennel, Auroral micropulsation instability, *J. Geophys. Res.*, **75**, 1863, 1970

D'Angelo, N., Role of the universal instability in auroral phenomena, *J. Geophys. Res.*, **74**, 909, 1969

Davidson, G.T., Pitch angle diffusion in morningside aurorae 2. The formation of repetitive auroral pulsations, *J. Geophys. Res.*, **91**, 4429, 1986

DeForest, S.E., and C.E. McIlwain, Plasma clouds in the magnetosphere, *J. Geophys. Res.*, **76**, 3587, 1971

Ejiri, M. Trajectory traces of charged particles in the magnetosphere, *J. Geophys. Res.*, **83**, 4798, 1978

Evans, R.D., *The Atomic Nucleus*, McGraw-Hill Book Company, Inc., New York, 1955

Hasegawa, A., Drift-wave instability at the plasma pause, *J. Geophys. Res.*, **76**, 5361, 1971

Hofmann, D.J. and R.A. Greene, Balloon observations of simultaneous auroral X-ray and visible bursts, *J. Geophys. Res.*, **77**, 776, 1972

Hones, E.W., Jr., S. Singer, L.J. Lanzerotti, J.D. Pierson, and T.J. Rosenberg, Magnetospheric substorm of August 25-26, 1967, *J. Geophys. Res.*, **76**, 2977, 1971

Jackson, J.D., *Classical Electrodynamics*, John Wiley and Sons, New York, 1975

Jentsch, Volker, Electron precipitation in the morning sector of the auroral zone, *J. Geophys. Res.*, **81**, 135, 1976

Kan J.R. and L.C. Lee, Formation of auroral arcs and inverted-V precipitations: An overview, *Physics of Auroral Arc Formation, Geophys. Monogr. Ser.*, vol. 25, edited by S.-I. Akasofu and J.R. Kan, p.160, AGU, Washington D.C., 1981

Kangas, J., L. Lukkari, P. Tanskanen, H. Trefall, J. Stadsnes, G. Kremser, and W. Riedler, On the morphology of auroral-zone X-ray events, IV, substorm-related electron precipitation in the local morning sector, *J. Atmos. Terr. Phys.*, **37**, 1289, 1975

Kaye, S.M., and M.G. Kivelson, Time dependent convection electric fields and plasma injection, *J. Geophys. Res.*, **84**, 4183, 1979.

Koch, H.W. and J.W. Motz, Bremsstrahlung cross-section formulas and related data, *Revs. Modern Phys.*, **31**, 920, 1959

Kennel, C.F. and H.E. Petschek, Limit on stably trapped particle fluxes, *J. Geophys. Res.*, **71**, 1, 1966

Kennel, C.F. Consequences of a magnetospheric plasma, *Rev. of Geophys.*, **7**, 379, 1969

Kivelson, M.G., S.M. Kaye, and D.J. Southwood, The physics of plasma injection events, in *Dynamics of the Magnetosphere*, ed. S.-I. Akasofu, pp 385-405, D. Reidel, Hingham, Mass, 1979.

Knoll, G.F., *Radiation Detection and Measurement*, John Wiley and Sons, New York, 1979

Konradi, A.C., L. Semar, and T.A. Fritz, Substorm-injected protons and electrons and the injection boundary model, *J. Geophys. Res.*, **80**, 543, 1975.

Krall, N.A. and A.W. Trivelpiece, *Principles of plasma physics*, McGraw-Hill, New York, 1973

Kremser, G., J. Bjordal, L. Block, K. Bronstad, M. Havag, I.B. Iversen, J. Kangas, A. Korth, M.M. Madsen, J. Niskanen, W. Riedler, J. Stadsnes, P. Tanskanen, K.M. Torkar, and S. Ullaland, Coordinated balloon-satellite observations of enegetic particles at the onset of a magnetosheric substorm, *J. Geophys. Res.*, **87**, 1982

Kremser, G., A. Korth, S. Ullaland, J. Stasdnes, W. Baumjohansen, L. Block, K.M. Torkar, W. Riedler, B. Aparicio, P. Tanskanen, I.B. Iversen, N. Cornilleau-Wehrlin, J. Solomon, and E. Amata, Energetic electron precipitation during a magnetospheric substorm and its relationship to wave particle interaction, *J. Geophys. Res.*, **91**, 5711, 1986

Lanzerotti, L.J. and M. Schulz, *Particle diffusion in the radiation belts*, Springer-Verlag, New York, 1974

Lyons, L.R., Electron diffusion driven by magnetospheric electrostatic waves, *J. Geophys. Res.*, **79**, 575, 1974

Lyons, L.R. and D.S. Evans, An association between discrete auroral and energetic particle boundaries, *J. Geophys. Res.*, **89**, 2395, 1984

Maeda, K., N.K. Bewtra and P.H. Smith, Ring current electron trajectories associated with VLF emissions, *J. Geophys. Res.*, **83**, 4339, 1978

Mauk, B.H. and G.K. Parks, X-ray images of an auroral breakup, *Physics of Auroral Arc Formation, Geophys. Monogr. Ser.*, vol. 25, edited by S.-I. Akasofu and J.R. Kan, p.129, AGU, Washington D.C., 1981

Mauk, B.H., J. Chin and G. Parks, Auroral X-ray Images, *J. Geophys. Res.*, 86, 6827 1981

Mauk, B.H. and C.-I. Meng, Characterization of geostationary particle signatures based on the 'injection boundary' model, *J. Geophys. Res.*, **88**, 3055, 1983.

McIlwain, C.E., Substorm injection boundaries, in *Magnetospheric Physics*, ed. B.M. McCormac, p143, D Reidel, Hingham, Mass. 1974.

McIlwain, C.E., Equatorial magnetospheric particles and auroral precipitation, in *Results of the ARCAD 3 Project and of the Recent Programmes in Magnetospheric and Ionospheric Physics*, p 275, Cepadues-Editions, Toulouse, France, 1985

McPherron, R.L., G.K. Parks, F.V. Coroniti and S.H. Ward, Studies of the magnetospheric substorm 2. Correlated magnetic micropulsations and electron precipitation occuring during auroral substorm, *J. Geophys. Res.*, 73, 1697, 1968

Melrose, D.B., *Instabilities in space and laboratory plasmas*, Cambridge University Press, New York, 1986

Meng, C.-I. and S.-I. Akasofu, Electron precipitation equatorward of the auroral oval and the mantle aurora in the midday sector, *Planet. Space Sci.*,**31**, 889, 1983

Moore, T.E., R.L. Arnoldy, J. Feynman, and D.A. Hardy, Propagating substorm injection fronts, *J. Geophys. Res.*, **86**, 6713, 1981

Mosteller, F. and J.W. Tukey, Data Analysis and Regression, Addison-Wesley Publishing Co., New York, 1977

Newell, P.T. and C.-I. Meng, Low altitude observations of dispersionless substorm plasma injections, *J. Geophys. Res.*, **92**, 10063, 1987

Oguti, T., J. Meek and K. Hayashi, Multiple correlation between auroral and magnetic pulsations, *J. Geophys. Res.*, **89**, 2295, 1984

Omholt, A. and G.J. Kvifte, H. Pettersen, Pulsating aurora, in *Atmospheric Emissions*, NATO Advanced Study Institute, edited by B.M. McCormac and A. Omholt, Van Norstrand Company, New York, 1969

Papoulis, A., *Probability, Random Variables, and Stochastic Processes*, McGraw-Hill Book Company, New York, 1984

Parks, G.K., F.V. Coroniti, R.L. McPherron and K.A. Anderson, Studies of the magnetospheric substorm 1. Characteristics of modulated energetic electron precipitation occuring during auroral substorms, *J. Geophys. Res.*, 73, 1685, 1968

Parks, G.K., and J.R. Winkler, Acceleration of energetic electrons observed at synchronous altitude during magnetospheric substorms, *J. Geophys. Res.*, **73**, 5786, 1968

Parks, G.K., and J.R. Winkler, Simultaneous observations of 5-to 15-second period modulations electron fluxes at the synchronous altitude and the auroral zone, *J. Geophys. Res.*, **74**, 4003, 1969

Pfitzer, K.A., and J.R. Winkler, Intensity correlations and substorm electron drift effects in the outer radiation belt measured with the OGO 3 and ATS 1 satellites, *J. Geophys. Res.*, **74**, 5005, 1969

Pilkington, G. R. and C. D. Anger, A Monte Carlo analysis of the passage of auroral X-rays through the atmosphere, *Planet. Sp. Sci.*, **19**, 1069, 1971

Rosenberg, T.J., J. Bjordal and G.J. Kvifte, On the coherency of X-ray and optical pulsations in aurorae, *J. Geophys. Res.*, **72**, 3504, 1967

Royrik, O. and T.N. Davis, Pulsating aurora: Local and global morphology, *J. Geophys. Res.*, 82, 4720, 1977

Sauvaud, J.A., J.P. Treilhou, A. Saint-Marc, J. Dandouras, H. Reme, A. Korth, G. Kremser, G.K. Parks, A.N. Zaitzev, V. Petrov, L. Lazutine, and R. Pellinen, Large scale response of the magnetosphere to a southward turning of the interplanetary field, *J. Geophys. Res.*, **92**, 2365, 1987

Scourfield, M.W.J. and N.R. Parsons, Auroral pulsations and flaming - some inital results of a cinematographic study using an image intensifier, *Planet. Space Sci.*, **17**, 1141, 1969 References from Appendices

Stadsnes, J., Correlated X-ray images and aurora, Oral Presentation at 8th Symposium on European Rocket and Balloon Programmes and Related Research Sunne, Sweden, 1987

Tanskanen, P., J. Kangas, L. Block, G. Kremser, A. Korth, J. Woch, I.B. Iversen, K.M. Torkar, W. Riedler, S. Ullaland, J. Stasdnes, and K.-H. Glassmeier, Different phases of a magnetospheric substorm on July 23, 1979, *J. Geophys. Res.*, **92**, 1987

Thorne, R. M. and C.F. Kennel, Relativistic electron precipitation during magnetic storm main phase, *J. Geophys. Res.*, **76**, 4446, 1971

US Standard Atmosphere, National Oceanic and Atmospheric Administration, Washington, DC, 1977

Vampola, A.L., Electron pitch angle scattering in the outer zone during magnetically disturbed times, *J. Geophys. Res.*, **76**, 4685, 1971

Walker, R.G. and M.G. Kivelson, Energization of electrons at synchronous orbit by substorm-associated cross-magnetospheric electric field, *J. Geophys. Res.*, **80** 2074, 1975.

West, R.H. and G.K. Parks, ELF emissions and relativistic electron precipitation, *J. Geophys. Res.*, **89**, 159, 1984

Appendix A

X-ray Interactions with Matter

A.1

This appendix will present the theory of x-ray interactions in matter. This has two purposes; to understand principles upon which the detection of x-rays is based, and to formulate a basis for the x-ray transport problem presented in chapter 3. In addition to x-ray interactions, the theory of scintillation detectors will be detailed as a basis for discussion of the associated problems of noise and fluctuations. The latter is an important feature in this type of instrument and should be understood.

An energetic photon can interact with matter in several different ways, but for the energy ranges we are concerned with, 20 to 150 keV, the two most important are photoelectric and Compton interactions. These are not exclusive of one another unless initial reaction is of the photoelectric type. This interaction is the well known effect in which the photon's energy is given up to free a bound electron, with the difference in the photon's energy and the ionization potential going into kinetic energy of the electron. Depending upon the material and the orbital from which the electron originated, the ionization potential can vary from 10's of ev to 10's of keV. The consequences of the higher ionization potential produces a sharp discontinuity for the photoelectric cross section in high Z materials. This is due to the sudden increase in the number of electrons that can interact with the photon once its energy surpasses that of an inner shell. For sodium iodide, this is the K shell and is known as the K-edge effect.

Compton scattering is a process resulting from conservation of momentum and energy during the photon-electron interaction; the scattered photon has less energy and a new trajectory, and the electron has taken up the difference in energy. The energy transfer is a function of the angle through which the photon is deflected; large deflections have larger energy transfers. This relationship is;

$$E_{scatt} = \frac{E_0}{1 + \alpha(1 - \cos\theta)} \qquad \text{(A.1)}$$

where E_{scatt} and E_0 are the scattered and incident photons, respectively, $\alpha = \frac{E_0}{m_e c^2}$, and θ is the angle through which the photon is scattered.

After a Compton collision the photon is still able to undergo photoelectric absorption or perhaps another Compton scattering. If the photon undergoes a large angle deflection near the surface of the medium, it stands a chance of being lost and not depositing its entire energy to the medium and will degrade the resolution of the detector. Figure (A.2) shows a polar plot of the differential cross section for Compton scattering as given by Eqn. (A.2), [*Evans*, 1955], which is derived from the Klein-Nishina formula by averaging over photon polarizations. In this equation, r_0 is the classical electron radius and $d\Omega$ is the element of solid angle into which the photon is scattered.

$$\frac{d\sigma}{d\Omega} = r_0^2 \left(\frac{E_{scatt}}{E_0}\right)^3 \left(\frac{E_0}{E_{scatt}} + \frac{E_{scatt}}{E_0} - \sin^2\theta\right) \qquad \text{(A.2)}$$

Aside from the pathologies mentioned above in connection with the two different interaction processes, the problem of energy deposition by an x-ray has now been reduced to the problem of stopping an energetic electron. Therefore the emphasis will now shift to the physics of a fast electron in a medium.

The only method of interaction for the energy regime 20-120 keV for a fast electron is a Coloumb collision, although the details are quite different depending on whether the electron is primarily interacting with a nucleus or a bound electron. In the case of the former, the energy losses are due to radiation of the accelerating electron in the Coloumb field of the nucleus, while in the latter case the energy losses are due to a transfer of energy to the bound system. The energy losses for electron-nuclei collisions is negligable relative to that lost in electron-electron collisions, approximately $\frac{E\,Z}{700}$ where E is in MeV and Z is the atomic number, [*Knoll*, 1979]. For iodine in sodium iodide, Z = 41, and the ratio is indeed small for 0.10 MeV electrons. The case of electron-electron collisions will be discussed first.

The correct way to investigate the collisional losses is through a quantum mechanical treatment which takes proper account of the wave nature of the particles as well as the discrete levels in which energy transfers can be made. The smallest energy transfers are those that excite the system to the lowest states while the largest ones will result in "ionization". The term ionization is being used loosely to include all energy transfers above a critical value. For atoms or simple molecules this may be an actual ionization process, however for crystal structures the electron will probably not escape the lattice, but will rattle around, loose energy, and eventually settle into the conduction band. The actual details of this process are less important than the fraction of energy deposition that will go into elevating electrons to the conduction band.

There are many more collisions which result in small energy transfers than in ionization, although it is the latter which are readily detectable, while the former result primarily in heating and dissipative effects. Due to the complexity of the above processes it is generally not possible to write down a formal expression to obtain the amount of ionization produced by a given energetic electron. A viable alternative is to obtain an averaged energy loss, which is the concept of "dE/dx", the incremental energy loss of the particle to the medium per incremental distance. For the case of a fast (but not relativistic) electron, this expression is given in Eqn. (A.3) and is due to Bethe. An expression is still required that relates the energy deposition from dE/dx losses to the actual number of ionization interactions, and this usually takes the form of an emperically determined value. Table (A.1) lists a few of these.

$$\frac{dE}{dx} = \frac{2\,\pi\, e^4 N\, Z}{m_0 v^2}\left[\log\frac{m_0 v^2 E}{2I^2} - \log 2 + 1\right] \tag{A.3}$$

The expression of Eqn (A.3) allows the stopping distance for a fast electron to be determined. The parameter I corresponds to an average ionization potential and E is is the energy of the fast electron. For fairly dense media (i.e., over $1\frac{g}{cm^2}$) of low to medium Z, the stopping distance will be on the order of one cm for sub-relativistic electrons. Therefore, for the case of photoelectric absorption of an x-ray in sodium iodide, the total energy can be considered to go into the medium. By using the value from Table (A.1) for ionization rates for various materials, an average number of scintillation photons can be estimated.

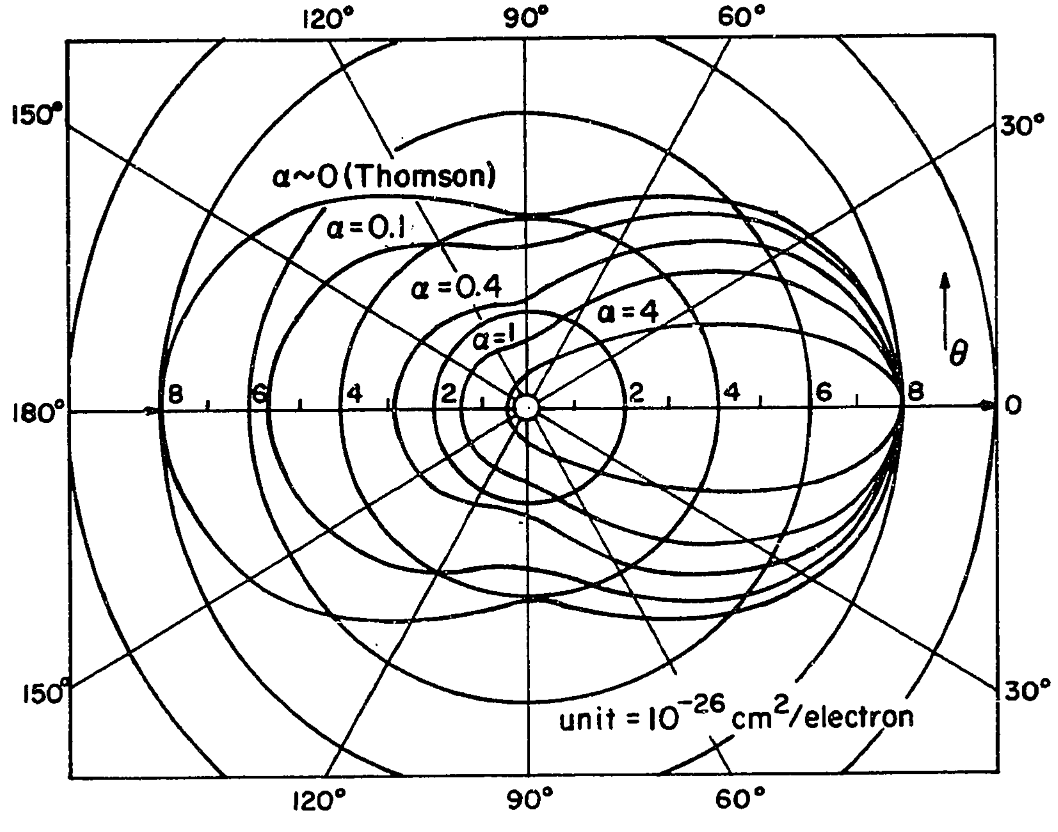

Figure A.1 Polar plot of Klein-Nishina differential cross section. From *Evans* [1955].

Appendix B

Scintillators and Photomultipliers

This appendix will present the characteristics of sodium iodide scintillators and general properties of photomultiplier tubes. The physics of how these devices work is important to the theory of X-ray detection in general, and imaging in particular. The theory of X-ray interaction in matter, which was presented in Appendix One, is also used in this appendix.

B.1 Scintillators

Inorganic scintillators have a lattice structure which lead to the formation of bands in the quantum energy levels. The lower lying levels of the constituent atoms are left relatively unperturbed, but the higher levels have deformed in such a way that the levels have become closely packed in two widely sperated bands, the valence and conduction bands. The inaccessible energy region is the forbidden zone. The ground state occupancy of the electrons is in the valence bands and excitations will elevate the electrons to the conduction band. The width of the forbidden zone is significantly greater than typical thermal energies and hence the conduction band is largely empty.

An excitation of a valence electron to the conduction band can only decay back to the ground state by an emission of a photon of energy equal to that of the forbidden zone width. For sodium iodide these photons lie in the ultraviolet and are readily aborbed by most window materials for PMTs. Furthermore, there would be significant self absorption resulting in poor overall efficiency. Therefore an impurity is introduced to alter the energy band structure at a small number of local sites within the lattice. The impurity is chosen to have allowed transitions in the range which the PMT photocathode is most sensitive. Since the majority of the crystal remains unchanged, excitation still occurrs in the same way, but the decay to ground state will be accomplished at the site of an impurity.

Figure (B.1) shows the emission spectrum of the luminescence for sodium iodide with thallium doping (NaI(Tl)). Important measures of perfomance are the efficiency, which is about 13%, and the decay constant, which is about 10^{-7} seconds, [*Knoll*, 1979]. The first indicates how much of the x-ray energy results in the emission spectrum while the second indicates what sort of x-ray input rates can be measured. Sodium iodide (Tl) has the highest efficiency of all the commonly used inorganic phosphors and therefore is a good choice for x-ray spectroscopy.

Figure (B.2) shows the coefficients for photoelectric absorption and Compton scattering for NaI. These so-called mass attenuation coefficients are obtained by calculating or measuring the total cross sections for the respective processes, and multiplying by a factor which takes into account the number of electrons which the photon can interact with in its path. The units are cm^2/g, and the attenuation of a beam of x-rays is given by;

$$n = n_0 \exp(-\int \sigma_{tot} \, \rho \, dx) \tag{B.1}$$

where ρ is the density, σ_{tot} is the total attenuation coefficient, and dx is along the path of the beam. This result is general for all media. For the case of NaI, the density can be considered constant.

The coefficient for photoelectric absorption in Figure (B.2) shows a discontinuity at 35 keV. Below this energy, the photon can interact only with L shell electrons while above the electron can be photoelectrically absorbed by either K or L shell electrons. This sudden increase in the number of electrons that can lead to absorption gives rise to the discontinuity in the attenuation coefficient, called the K-edge effect.

B.2 Photo Multiplier Tubes

Since the way in which a photomultiplier tube (PMT) works has a dominate influence on the response of the system, it will be examined in some detail here. The utility of this device lies in its high sensitivity and its inherent amplification abilities. This high gain is achieved through a cascade process in which every stage accelerates electrons to the next dynode with sufficient energy to eject several new electrons for each impingent one. The final output at the anode is a burst of charge. The photocathode and the amplification process are a significant source of noise and fluctuations in the system, so these will be the main topic of this section.

There are several competing factors in the design of the photocathode. The quantum efficiency is dependent upon the ability of the material to absorb the incident photon and whether the produced photoelectron can escape. If such an electron is produced too deep within the material, it will loose enough energy through collisions to be unable to overcome the surface potential barrier. However, if the photocathode is made too thin in order to reduce the collisional energy losses, incident photons may not be absorbed. A futher complication arises in compounds with too low of a surface potential barrier; such a material will also allow more thermal electrons to escape and will be noisy. The so-called bi-alkyli photocathodes, such as sodium-potassium, eliviates many of these problems while maintaining an overall quantum efficiency of 16-20%. The PMTs used in the x-ray camera had sodium-potassium photocathodes.

The spectral response of the PMT at the short wavelength end is determined largely by the material on which the photocathode is coated; glass is essentially opaque to UV. At the long wavelength end the determining factor is the thickness of the photocathode. Since the escape depth (the maximum distance a photoelectron can travel and still have enough energy to overcome the surface potential) is a function of the incident photon energy, the less energetic photons will produce photoelectrons which cannot escape. Thus at wave lengths in which the skin depth for the photon becomes comparable to the escape depth, there will be a fall off in response of the PMT. Figure (B.1) shows the spectral response for the class of PMT used in the X-ray camera, together with the emission spectrum of the NaI scintillator.

The photoelectrons are accelerated by an electric field to the first dynode. When they impact, each primary electron will eject several secondary electrons; these are again accelerated to the next dynode. This process is cascaded until the desired amplification is achieved, usually on the order of 10^5 to 10^6. Since the number of secondaries produced is roughly proportional to the primary incident energy, and hence, to the electric field, the PMT gain can be varied by changing the potential applied across the various dynodes.

If each dynode acted in an ideal manner and ejected a constant number of secondary electrons for each impingent primary electron, the gain would be, $G = \delta^N$, where δ are the number of secondaries produced, and N is the number of stages. However, the actual performance of a dynode is not ideal and the value for δ fluctuates, resulting in variations in the gain. Since any such variations that occur early in the cascade process are also amplified, the first and possibly second dynodes are the major source of overall fluctuations in output. The actual effect on the response will be considered further in the next secton.

B.3 Statistics: Sources of Noise and Error

The parameters used to evaluate performance are efficiency, noise, and resolution. The overall efficiency is the amount of incident energy that is converted into energy suitable for the detection scheme. For instance, in a scintillator it would be the ratio of energy which goes into visible photons, to the original X-ray energy. The noise is defined to be the background count-rate (in pulse mode) or dark current (in current mode) which specifies the level of output without input. The resolving ability is defined as the full-width-half-maximum (FWHM) value associated with the occurrence of a monochromatic peak in a pulse-height distribution, normalized to the mean value of the peak.

The production of statistically meaningful images depends upon the ability to identify two components to the measured data, the noise and the "signal". This procedure can be helped by an analysis of noise sources. Those which arise within the instrument are addressed in this section, while those that are associated with the statistics of the X-ray source will be analysed in the next in Chapter Two. The purpose of this analysis is to ascertain whether we can predict the behavior of the instrument and thus know if it is performing as expected.

The primary sources of statistical variations are the components of the system discussed above; the scintillating package (NaI and quartz window), the photocathode, and the PMT dynodes. All of these involve discrete events which suggests the application of binomial statistics, or one of its derivatives, to model these processes. The use of a model to compare with the actual performance is attractive since the results of a particluar statistical process, such as binomial, can be simple and well understood. The question of applying this statistical model, or one of its approximations, is worth looking at.

Binomial statistics are derived from Bernoulli trials which can be stated as a sequence of N independent events, each of which has the same probability, p, of having one of two outcomes. This distribution will give the probability that M of those events will all have the same outcome. When N becomes very large, and p is very small such that the product Np is finite, we can use the approximation known as the Poisson distribution. If N is very large but p is not small, the de Moivre-Laplace Theorem allows us to approximate with a Gauss distribution. In any event, a necessary requirement for any of these three is that all events are independent and p is constant for each event, [*Papoulis*, 1984].

A single X-ray produces many scintillation photons which propagate through the scintillator optics to the photocathode. For the sake of clarity, the former will be identified as N_1, and the number transmitted as N_2. The number of photoelectrons produced will be N_3, and the number of secondary electrons per primary electron at the first dynode as N_4. The behavior of the photocathode and the loss mechanism within the scintillator package certainly meet the requirement of independence since the absorption of a photon is independent of any other absorptions, and likewise with the photoelectric process. Therefore, N_2 *and* N_3 can be modeled as Poisson processes. The other two are more complex.

To examine the behavior of the first and last processes, we identify the probability of the production of a photon, or a secondary electron, from the fast electron as p. The evaluation of p is not so easy, but intuitively we know that it must involve the collision cross section for two charged particles. This has the general form;

$$\frac{d\sigma}{d\Omega} \approx \frac{C}{v^2} \tag{B.2}$$

where v is the velocity of the fast electron through the material. Equation 2.5 shows that each collisional interaction depends upon the details of previous collisions through the velocity, since each collision reduces v by some amount. When v is large, these incremental transfers will result in small relative changes and the cross section is only weakly dependent upon previous events. However, as the electron looses energy to the media the dependence becomes stronger.

A reasonable conclusion is that the events are not independent, p is not constant, and binomial statistics, or the approximations, should not hold. However, for the case of N_1, dependence is weak for much of the production process since v is initially very large. This is not the case for N_4 as the velocity starts out small and the correlations between events will be stronger. Poisson statistics is perhaps a reasonable approximation to model N_1, but not N_4. Since no other information is available on the process N_4, it will be modeled as binomial, but this is certainly the weakest link in the statistical chain.

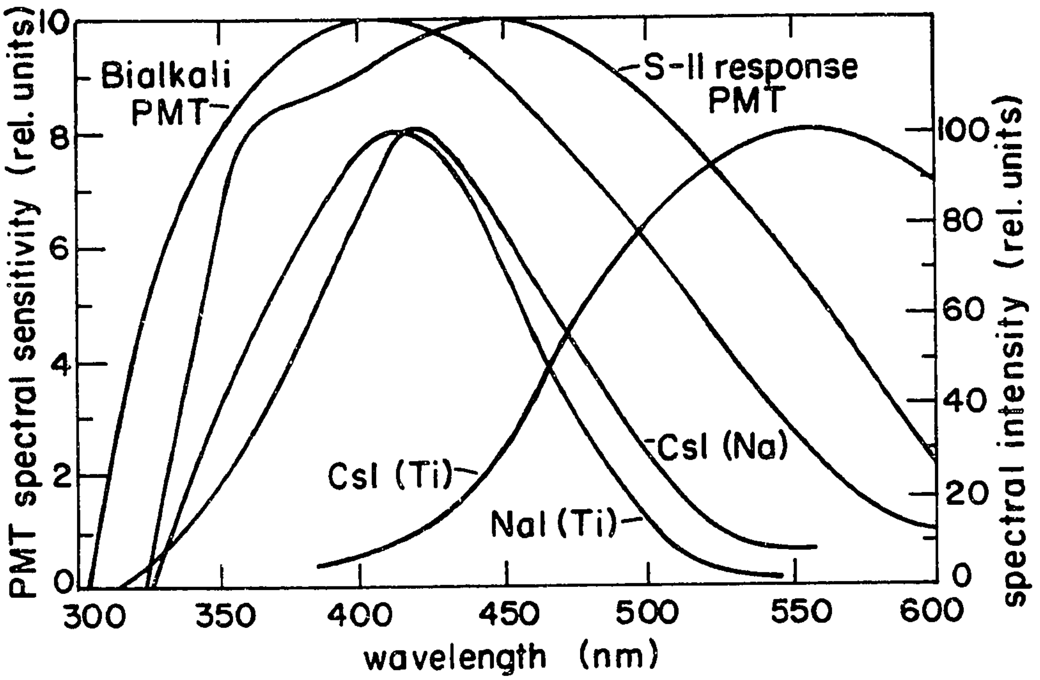

Figure B.1 Emission spectrum of NaI, and PMT spectral response. From *Knoll* [1979].

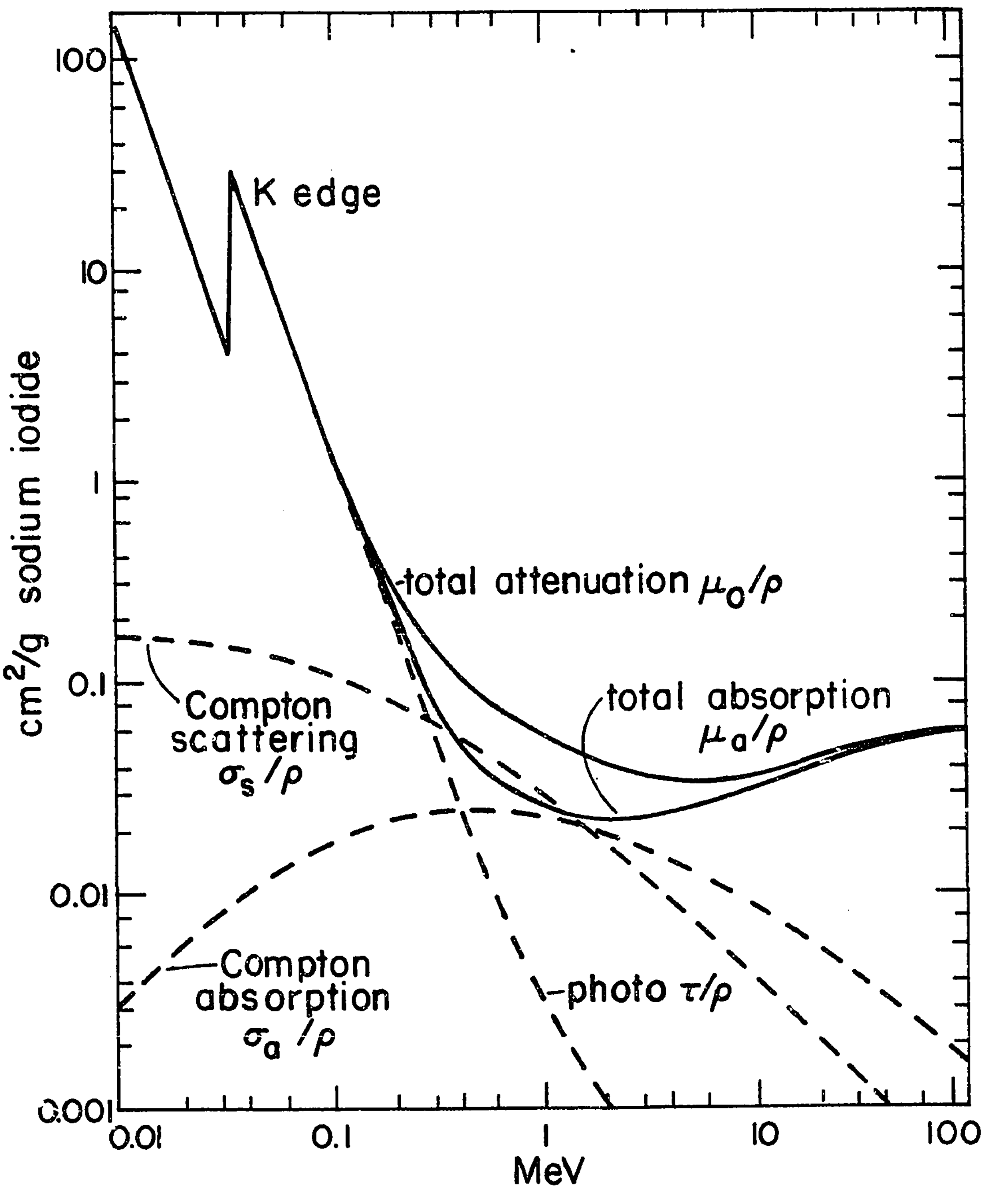

Figure B.2 Mass attenuation coefficients for NaI. From *Evans* [1955].

Vita

Scott H. Werden was born November 27, 1951 in California. He graduated from high school in Torrance, California in 1969 and received his Bachelor of Science degree, majoring in Chemistry, from the University of Washington in 1982.